

**Spiral Wave Initiation in
Reaction-Diffusion-Mechanics Systems:
A Model for the Onset of Reentrant Cardiac
Arrhythmia**

Cover A spiral (oil pastel on paper). Louis Daniel Weise (2012)

Print Proefschriftmaken.nl || Uitgeverij BOXPress

ISBN 978-90-8891-480-5

No part of this thesis may be reproduced in any form, by any print, microfilm, or any other means, without prior written permission of the author.

**Spiral Wave Initiation in
Reaction-Diffusion-Mechanics Systems:
A Model for the Onset of Reentrant Cardiac
Arrhythmia**

**Spiraalgolven in Reactie-Diffusie-Mechanica Systemen:
een Model voor het Ontstaan van Hartritmestoornissen
(met een samenvatting in het Nederlands)**

**Spiralwellen in Reaktions-Diffusions-Mechanik-Systemen:
ein Modell für das Entstehen von Herzrhythmusstörungen
(mit einer Zusammenfassung in Deutsch)**

Proefschrift

ter verkrijging van de graad van doctor aan de Universiteit Utrecht op gezag van de rector magnificus, prof. dr. G.J. van der Zwaan, ingevolge het besluit van het college voor promoties in het openbaar te verdedigen op maandag 29 oktober 2012 des middags te 4.15 uur

door

Louis Daniel Weise

geboren op 22 juli 1979 te Aalen, Duitsland

Promotoren: Prof. dr. R.J. de Boer
Prof. dr. A.V. Panfilov

The studies described in this thesis were performed at the department of Theoretical Biology and Bioinformatics at Utrecht University. The investigations were financially supported by the Netherlands Organization for Scientific Research (<http://www.nwo.nl>) (NWO Grant No. 613.000.604) of the research Council for Physical Sciences (EW).

Meiner Familie

Contents

1	Introduction	1
1.1	Short Introduction	1
1.2	The Human Heart	2
1.3	Excitable Media	3
1.4	Excitability of Cardiac Tissue	4
1.5	Modeling Biological Excitability	5
1.5.1	Electrical Circuit Model of the Cell Membrane	5
1.5.2	Hodgkin-Huxley Model	6
1.5.3	FitzHugh-Nagumo Model	7
1.5.4	Models for Cardiac Cell Excitability	8
1.5.5	Cable Equation	10
1.6	Cardiac Excitation-Contraction Coupling	11
1.7	Cardiac Mechano-Electrical Feedback	12
1.8	Reaction-Diffusion-Mechanics Models	13
1.8.1	Excitation-Contraction Coupling	13
1.8.2	Cardiac Elasticity	14
1.8.3	Mechano-Electrical Feedback	16
1.9	Reentrant Cardiac Arrhythmia and Spiral Waves	17
1.9.1	Reentry	17
1.9.2	Spiral Wave Initiation	18
1.10	Motivation	20
1.11	Outline	20
2	A Discrete Model to Study Reaction-Diffusion-Mechanics Systems	23
2.1	Introduction	25
2.2	Methods	26
2.2.1	Reaction Diffusion Model for Cardiac Excitation	26
2.2.2	Excitation-Contraction Coupling Model	27
2.2.3	Mass-Lattice Model	27
2.2.4	Electromechanical Feedback	30
2.2.5	Numerical Methods	32
2.2.6	Model Validation	33
2.2.7	Computational Performance	36

2.3	Results	38
2.3.1	Pacemaker Drift	38
2.4	Discussion	47
2.5	Acknowledgements	48
3	New Mechanism of Spiral Wave Initiation in a Reaction-Diffusion-Mechanics System	49
3.1	Introduction	51
3.2	Methods	52
3.2.1	Numerical Methods	54
3.2.2	Pinwheel Experiment	55
3.3	Results	56
3.3.1	“Classical Vulnerable Zone” in Deforming dRDM System	56
3.3.2	New Mechanism of Spiral Wave Initiation	57
3.3.3	Dependence of the New Mechanism on Stimulation Parameters	58
3.3.4	Mechanically Initiated Spiral Waves	60
3.4	Discussion	63
3.5	Acknowledgments	65
4	Emergence of Spiral Wave Activity in a Mechanically Heterogeneous Reaction-Diffusion-Mechanics System	67
4.1	Introduction	69
4.2	Model	69
4.3	Results	71
4.4	Discussion	76
4.5	Acknowledgements	76
5	A Discrete Electromechanical Model for Human Cardiac Tissue	77
5.1	Introduction	79
5.2	Model	80
5.2.1	Model for Cardiac Excitation	80
5.2.2	Excitation-Contraction Coupling Model	81
5.2.3	Mass-Lattice Model	82
5.2.4	Mechano-Electrical Feedback	84
5.2.5	Numerical Methods	84
5.2.6	Model Validation	85
5.3	Results	87
5.3.1	Effect of Constant Stretch on Action Potential	87
5.3.2	Action Potential and Conduction Velocity Restitution	89
5.3.3	Spiral Wave Dynamics	91
5.3.4	Spiral Wave Initiation in a Medium with Complex Geometry	93
5.4	Discussion	96
5.5	Acknowledgements	97

6 Discussion	99
6.1 A Short Review	99
6.2 Model Complexity and Limitations	101
6.3 Future Directions	103
6.4 Conclusion	104
Bibliography	107
Samenvatting	117
Zusammenfassung	119
Curriculum Vitæ	121
List of Publications	123
Acknowledgements	125

Chapter 1

General Introduction and Overview

1.1 Short Introduction

Heart failure due to cardiac arrhythmias is a major cause of death in the industrialized world [1]. Cardiac arrhythmia is often caused by spiral waves of electrical activity in the cardiac muscle [2–4]. Therefore, it is a major task in cardiology to understand the mechanisms of spiral wave initiation in the heart.

Valuable insights into mechanisms of the onset of arrhythmia have been achieved by studying spiral wave initiation in reaction-diffusion systems as models for cardiac tissue [5, 6]. However, most of these studies did not take the deformation of the heart into account [7]. Yet mechanical changes have been shown to significantly affect heart functioning [8]. In fact, deformation of the heart has been demonstrated to be able to cause, but also to abolish dangerous cardiac arrhythmias [9, 10].

This thesis focuses on the question: “What is the effect of deformation on mechanisms of the onset of reentrant cardiac arrhythmia?”. To study this problem, mechanically discrete reaction-diffusion-mechanics models of cardiac electromechanical activity are developed, and spiral wave initiation is studied in these systems as a model for the onset of reentrant cardiac arrhythmia.

1.2 The Human Heart

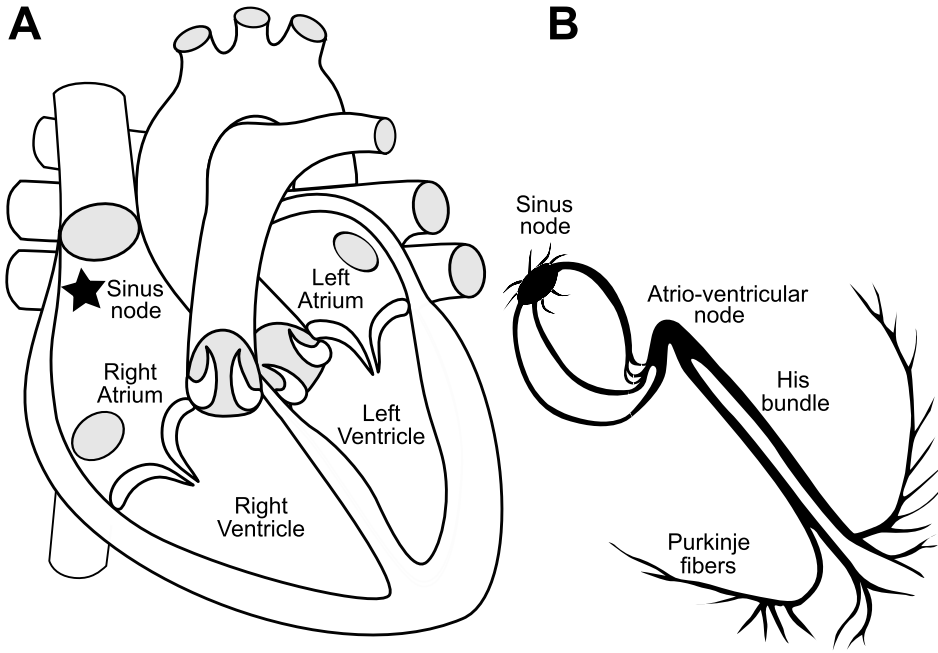


Figure 1.1. The human heart. (A) Schematic ventral view on cross section of a heart. (B) Heart's conduction system.

The heart is an organ which rhythmically pumps blood through the body to sustain the metabolic activity of every cell. It pumps blood in two cycles. In the pulmonary cycle blood is pumped from the right ventricle to the lung where the metabolic end product carbon dioxide is released and fresh oxygen is loaded (see Figure 1.1A). From there the oxygen rich blood is pumped back to the heart. In the large, systemic blood cycle the left ventricle (see Figure 1.1A) pumps oxygen rich blood to all other organs, on this course the blood absorbs nutrients entered via the small intestine, releases waste products in the kidneys and liver, and finally releases nutrients and oxygen to the cells and loads carbon dioxide and other metabolic waste products. The blood cycle is closed as the carbon dioxide-rich blood is pumped back to the right atrium.

The contraction of the heart is initiated by spreading waves of electrical activity. This process is intrinsically controlled by so called pacemaker cells that together form the sino-atrial node in the upper right atrium (see Figure 1.1). Nervous activity has only a modulating role on the excitation frequency of the heart. The pacemaker cells are synchronously auto-oscillating between a low and a high “excited” state of transmembrane potential to rhythmically initiate spreading waves

of electrical activation. The heart tissue is able to conduct a wave of electrical activity because cardiomyocytes are electrically coupled to neighboring cells via gap junctions forming a functional syncytium. Thus, the sino-atrial node initiates waves of excitation that propagate through the atria causing them to contract and pump blood into the ventricles. When the atria contract the ventricles are mechanically passive and not excited. This delay between atrial and ventricular activity is caused by the indirect electrical connection of the ventricles to the atria via the atrio-ventricular node (see Figure 1.1B) in which the conduction velocity of the excitation wave is low. When the wave of electrical excitation leaves the atrio-ventricular node and reaches the bundle of His (see Figure 1.1B) the excitation wave rapidly spreads over the Purkinje system to excite the ventricles and cause its simultaneous contraction (see Figure 1.1B).

The process illustrated above corresponds to normal heart functioning, and often a human's heart works reliably during a life time beating well over a billion times. However, the process of healthy heart functioning can be disturbed by abnormal sources of excitation that underly cardiac arrhythmias. When abnormal sources of excitation cause severe arrhythmias, the heart's pumping function will fail and brain damage and death within minutes follows. In fact, sudden cardiac death is the biggest killer in the industrialized world accounting for about one death in ten [11]. It is therefore of great importance to understand the mechanisms of the onset of these dangerous malfunctions in the heart.

1.3 Excitable Media

In a generic approach an excitable medium can be seen as a system built up by connected elements far from thermodynamical equilibrium that can be either in a ground or an excited state. Examples of such elements are neurons or cardiac cells that can be electrically excited, or an oscillating chemical system, and also individuals in a population in which they can be in a healthy or in an infected state. A stimulation of an excitable element, which has to exceed a certain strength, can initiate an excitation process. In this excitation process an element goes to an excited state and after some time during which a further stimulation will not trigger a new excitation process, it recovers back to the ground state. It is important to note that the necessary energy for the excitation process is provided by the medium itself for example by the metabolism of excitable cells, individuals, or the free energy of reactants in a chemical system. The spatial coupling of excitable elements allows the spreading of excitation e.g. via diffusion of chemicals, and thus an excited element may cause a neighboring element to also become excited and a wave of excitation may spread in an excitable medium. Waves of spreading activity have been studied in various chemical systems such as the Belousov-Zhabotinsky reactions [12], and carbon monoxide oxidation on platinum surfaces [13]. Biological examples are spreading depression in nerve tis-

sue [14], waves of cAMP in the morphogenesis of *Dictyostelium discoideum* [15], and waves of spreading infection in populations [16]. The heart is an excitable medium in which electrical waves of excitation propagate through the tissue and initiate its contraction [17]. The following section explains cardiac excitability.

1.4 Excitability of Cardiac Tissue

The heart is built up from excitable cardiac muscle cells. These cardiomyocytes are excitable similar to neurons [18]. An excitable cell has voltage-gated ion-channels in its cell membrane, and there is a transmembrane potential at resting state ($\approx -85 \text{ mV}$) between the inside and outside of the cell membrane. This allows a cardiac cell to react on an applied stimulation which is normally a pulse of depolarizing current. If the stimulation is small, the resting potential will readjust quickly to its resting state. However, if the stimulation is above a certain threshold ($\approx -60 \text{ mV}$), fast sodium channels open and Na^+ -ions flow from the extracellular medium into the cytosol and cause a rapid depolarization (upstroke) of the transmembrane potential. This rapid depolarization is the initial phase (Phase 0) of a

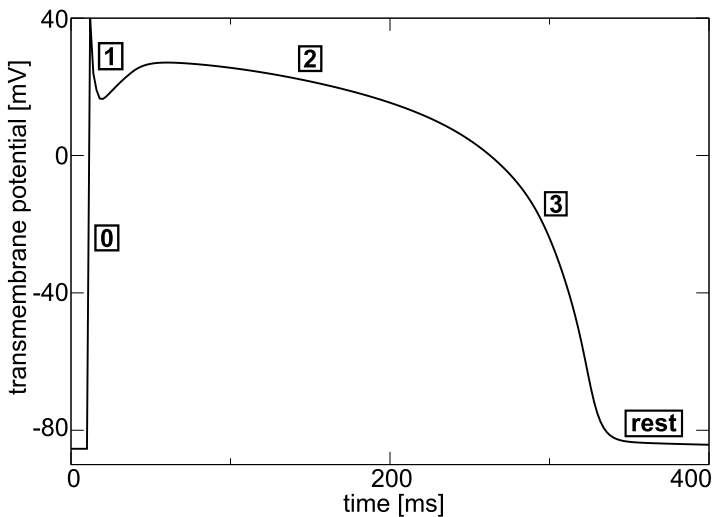


Figure 1.2. The action potential of a human cardiac cell (ventricular, epicardial). The pulse was computed with the Ten Tusscher model (2006) for epicardial cells [19], and initialized by setting the transmembrane voltage to -60 mV for 0.02 ms at time 10 ms .

process called the action potential (see Figure 1.2). Few milliseconds following their activation, the sodium channels are inactivated in a process which is also dependent on the transmembrane voltage. Next (Phase 1), early rapid repolarizing

net currents are caused by the voltage activated opening of the transient outward potassium channels. The following phase (Phase 2) is characterized by a long plateau ($\approx 300 \text{ ms}$) in which the transmembrane potential stays depolarized (see Figure 1.2) and the voltage-gated depolarizing L-type Ca^{2+} -current balances out repolarizing potassium currents. Finally, in the last stage of the action potential (Phase 3) L-type Ca^{2+} -current is inactivated and various repolarizing K^{+} -channels repolarize the cardiac cell to its resting potential (see Figure 1.2). It is important to note that the cardiac cell is inexcitable during the first three phases of the action potential, but regains the ability to generate a new action potential only in the later repolarization phase (late phase 3).

A breakthrough in the research on cell excitability happened in the year 1952, when Hodgkin and Huxley [18] published a work on the excitability of neurons. Ten years later Noble formulated the first mathematical model for cardiac cells [20]. The great importance of the study of cell excitability is reflected nowadays by thousands of scientific publications per year [21].

1.5 Modeling Biological Excitability

Mathematical modeling started to play an important role from the very beginning of the study of cell excitability [18], and is especially important in cardiology where experimental techniques are often limited, e.g. it is difficult to measure the heart's electromechanical activity.

In this section, we first introduce some basics of modeling cellular excitability, and then focus on the modeling techniques for cardiac tissue applied in the following chapters of this thesis.

1.5.1 Electrical Circuit Model of the Cell Membrane

The first step to model electrical excitation of cells is to formulate a model for the cell membrane in terms of an electrical circuit in which the outside, inside and membrane is described [22] (see Figure 1.3). It was shown that the cell membrane can be described in electrical terms as a capacitor, and voltage at this capacitor is changed by ionic currents across the cell membrane (see Figure 1.3) [22]. The total current is thus

$$C_m \frac{dV}{dt} + I_{ion} = 0, \quad (1.1)$$

where I_{ion} is the ionic current through the nonlinear resistor, $V = V_{in} - V_{out}$ (see Figure 1.3) is the transmembrane potential, and C_m is the capacitance of the membrane. To model cell excitability with Eq. (1.1) it is most important to

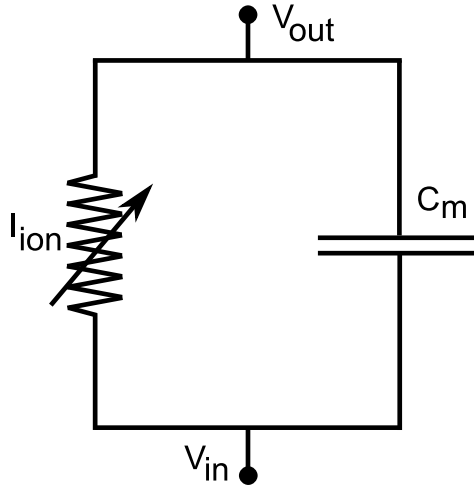


Figure 1.3. Circuit model of the cell membrane.

describe I_{ion} .

1.5.2 Hodgkin-Huxley Model

A milestone in physiology was reached 1952 by Hodgkin and Huxley [18] who were able to measure individual ionic currents, and formulate a model for I_{ion} for the giant axon of a squid. Their work demonstrates that the conductance of the cell membrane is constituted of voltage-dependent ion-channels for specific ion types (in squid axon mainly Na^+ and K^+ channels). One can write I_{ion} for a neuron as

$$I_{ion} = g_{Na}(V - V_{Na}) + g_K(V - V_K) + g_L(V - V_L), \quad (1.2)$$

where g_{Na} , g_K and g_L are the voltage-dependent conductances of the sodium, potassium and an unspecific leakage (mainly chloride) channels, and V_{Na} , V_K , V_L , are the respective Nernst potentials. Hodgkin and Huxley found that expressing conductances in terms of power functions of so called gating variables, which reflect opening probabilities of ion channels, yielded good agreement with experimental data. They wrote for the potassium conductivity

$$g_K = \bar{g}_K n^4, \quad (1.3)$$

where \bar{g}_K is the maximal possible potassium conductance and n is a voltage-dependent gating variable. The dynamics of the gating variables can be described with differential equations of the form

$$\frac{dn}{dt} = \frac{n_\infty(V) - n}{\tau(V)}, \quad (1.4)$$

where $n_\infty(V)$ is the steady state opening probability, and $\tau(V)$ a characteristic time constant. These voltage-dependent parameters for potassium and sodium channels were obtained experimentally. Note that there are activating gate variables and a deactivating gate variable for the sodium channel, and that no gating variables are used for the leakage current.

The Hodgkin Huxley model was the first step towards a deeper understanding of cell excitability. However, it is hard to study the equations of the Hodgkin Huxley model analytically. Therefore, attempts have been made to apply approximations to the Hodgkin Huxley equations, and in fact these studies yielded valuable insights [22]. The most successful approach has been introduced by FitzHugh and Nagumo.

1.5.3 FitzHugh-Nagumo Model

FitzHugh and Nagumo derived a two-variable model that captures qualitative features of the Hodgkin Huxley model [23, 24]. The general form of a FitzHugh-Nagumo-type model reads

$$\dot{u} = -F(u) - g, \quad (1.5)$$

$$\dot{g} = \epsilon(ku - g), \quad (1.6)$$

where u is a fast “excitation” variable, which represents the transmembrane potential, g is a slow “recovery” variable, $F(V)$ is a cubic function in u , and ϵ is a small number which causes the slow dynamics of g . A typical phase plane portrait of a FitzHugh-Nagumo-type model is shown in Figure 1.4, which is similar to a two-dimensional projection of the Hodgkin-Huxley model [22]. The action

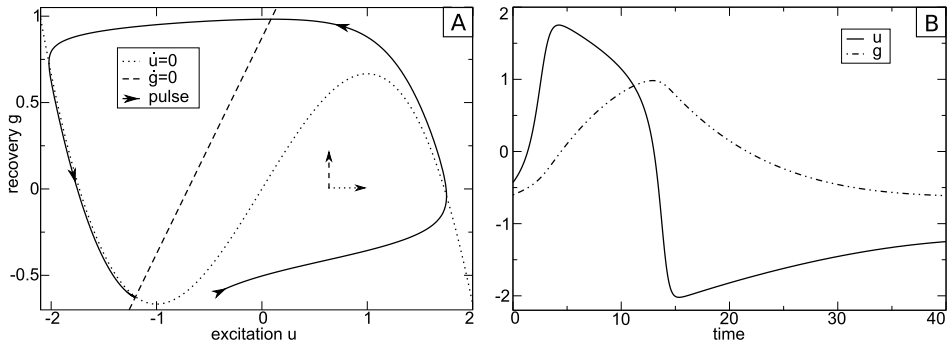


Figure 1.4. Bonhoeffer-van der Pol model. (A) Phase plane with pulse trajectory, and corresponding (B) action potential. Initial condition for the pulse is $u = 0.60$ and $g = 0.43$. The equations are: $\dot{u} = u - u^3/3 - g$, and $\dot{g} = 0.08 \times (u + 0.7 - 0.8g)$.

potential shown as a trajectory in the phase-plane in Figure 1.4A is also shown

in the excitation-time plot in Figure 1.4B. This simplification of the description of cell excitation allows the usage of efficient numerical integration methods, and even the usage of analytical techniques [22].

1.5.4 Models for Cardiac Cell Excitability

Although neuronal and cardiac cells are similar, the description of cardiac excitability requires special models. This is, because more ionic currents are involved during the cardiac action potential, and the dynamics of some ionic currents is different compared to neurons.

Ionic Models

The basic mechanisms for cell excitability in cardiac cells and neurons are similar. Noble showed 1962 that Hodgkin-Huxley-type modeling can be applied to model excitability of cardiac cells of the Purkinje system [20]. Further models for other cardiac cell types followed e.g. the Yanagihara model for cells of the sino-atrial node [25], and the Beeler-Reuter model for ventricular cells [26]. Today, there is a variety of ionic models for cardiac cells of different complexity that have been built in the spirit of the Hodgkin-Huxley modeling approach, but adjusted to reproduce properties of cardiac cells. In this thesis a well established ionic model for human ventricular cells, the TP06 model is applied [19, 27] (in chapter 5). The TP06 model describes all important ionic currents and reproduces properties such as action potential duration and restitution properties [19]. Furthermore, it describes the complex calcium dynamics, including dynamics in cellular compartments and Ca^{2+} triggered inactivation of L-type Ca^{2+} -channels, which is an important feature for models that take deformation into account, where calcium plays a major role [19].

Even though ionic models capture many important features of the cardiac action potential they are computationally difficult to use for some applications that require the simulations of a larger piece of tissue, as the necessary time steps to integrate the model equations are small [28]. Moreover, as for the Hodgkin-Huxley model, analytical techniques are hard to apply, and thus low-dimensional models similar to the FitzHugh-Nagumo model have been developed for cardiac excitability.

Low-dimensional Models

It has been shown that it is possible to formulate low-dimensional models for cardiac excitability to achieve computationally effective methods that can still cap-

ture qualitative features of the cardiac action potential [28]. FitzHugh-Nagumo-type models which have been formulated to model nerve excitability, are not perfect to model the cardiac action potential (although they are applicable to address qualitative research questions), because the shape of the cardiac action potential is not reproduced well. For example the classical example of a FitzHugh-Nagumo model as drawn in Figure 1.4B (“Bonhoeffer-van der Pol model”) shows a super-repolarization of the transmembrane potential ($V < \text{resting potential}$) which does not occur in the cardiac action potential (compare Figure 1.2). Another issue is that a good shape of the cardiac action potential requires that the rate of change of the recovery g is approximately constant during the repolarization phase.

Aliev and Panfilov proposed a FitzHugh-Nagumo-type model for cardiac excitation in which they addressed these issues [28]. They found, that super-repolarization can be prevented when a \dot{u} -nullcline $u = 0$ is present, and that a constant rate of the recovery during the repolarization phase can be assured when the curved nullclines $\dot{u} = 0$ and $\dot{g} = 0$ have a constant distance [28]. The Aliev-Panfilov is written as

$$\dot{u} = -ku(u - a)(u - 1) - ug, \quad (1.7)$$

$$\dot{g} = \epsilon(u, g)(-g - ku(u - a - 1)), \quad (1.8)$$

where $\epsilon(u, g) = \epsilon_0 + \mu_1 g / (u + \mu_2)$ determines the slow dynamics of the recovery variable g . The nullclines of the model are shown in Figure 1.5. The trajectory

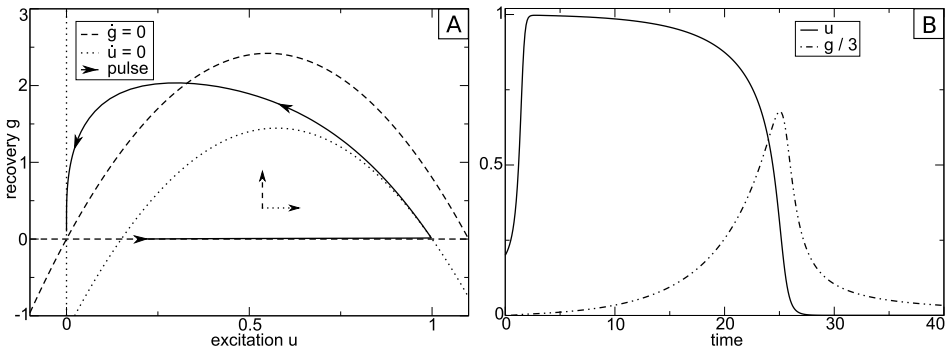


Figure 1.5. Aliev-Panfilov model. (A) Phase plane with pulse trajectory, and corresponding (B) action potential. Parameters are $\epsilon_0 = 0.002$, $\mu_1 = 0.2$, $\mu_2 = 0.3$, $k = 8$ and $a = 0.15$. Initial condition for the pulse is $u = 0.2$ and $g = 0$.

shown in Figure 1.5A describes the action potential shown in Figure 1.5B. Curved nullclines $\dot{u} = 0$ and $\dot{g} = 0$ have a constant distance in Figure 1.5A, and the action potential in Figure 1.5B shows no super-repolarization similar to the action potential shown in Figure 1.2. Interestingly, the nullclines of this model (Figure 1.5A) have been shown to be similar to experimentally achieved nullclines [29]. The Aliev-Panfilov model captures important features, such as the shape of the cardiac

action potential, and the restitution property (action potential duration as function of stimulation frequency) [28]. A modification of the Aliev-Panfilov is also used in this thesis (chapters 2-4).

1.5.5 Cable Equation

To describe heart tissue it is necessary to model the spatial coupling of individual cells to each other. The spatial coupling between cells can be described in terms of a special type of partial differential equations which will be explained in this section.

To derive a basic equation for pulse propagation in cardiac tissue it is useful to consider a one-dimensional excitable medium, a “cable” built up by electrically coupled excitable cells that are described by the circuit model (see Figure 1.3). The circuit of the cable model is shown in Figure 1.6. It turns out that in such a

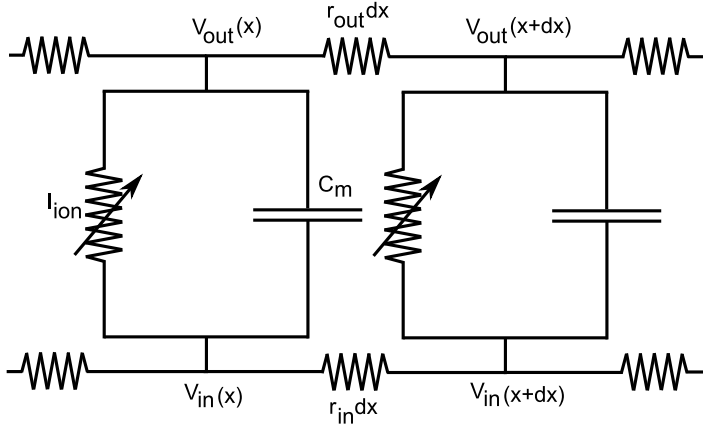


Figure 1.6. Cable model of an one-dimensional cellular excitable medium. Elements of the membrane circuit model are connected intra- and extra-cellularly, where r_{in}, r_{out} are resistances per unit length dx .

cable electrical pulse propagation adds a diffusion term to equation 1.1 to yield a reaction-diffusion (RD) equation [22]

$$C_m \frac{\partial V}{\partial t} = \frac{\partial^2 V}{\partial x^2} + I_{ion}, \quad (1.9)$$

where x is the spatial dimension of the cable. For higher dimensional excitable media the Laplacian in Equation 1.9 is of the dimension of the medium. Thus, to study non-deforming cardiac tissue one first has to formulate an appropriate model for I_{ion} , which depends on the cell type and solve the corresponding Equation 1.9.

Now, the basics on modeling non-deforming cardiac tissue via RD-equations have been introduced. However, in this thesis the influence of deformation on excitation processes is studied, which requires an extension of the RD-modeling approach. Before this extension will be introduced, it is explained how excitation processes are coupled to deformation of heart tissue in cardiac electrophysiology.

1.6 Cardiac Excitation-Contraction Coupling

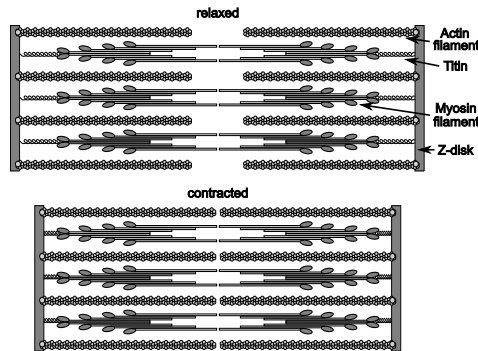


Figure 1.7. Schematic of a sarcomere. Top: sarcomere in relaxed state. Bottom: sarcomere in contracted state.

Excitation-contraction coupling of cardiomyocytes enables the heart's chambers to perform their pumping function. Myocytes gain the ability to create tension from contractile protein filaments “myofilaments” that are actin-filaments (thin filaments in Figure 1.7), and myosin-filaments (thick filaments with branching protein heads in Figure 1.7). Actin filaments form a complex with regulatory proteins tropomyosin and troponin C that in the relaxed state occupy the myosin binding sites preventing force generation. Myosin filaments are bound to the spring-like titin molecules [30] that are also attached to the Z-disks, which delimits each sarcomere (see Figure 1.7, top). Titin plays a major role in the passive elastic properties in muscle tissue [31]. The myofilaments form the structural units of a myofibril, which are cylindrical organelles of myocytes. Sarcomeres produce contractile force in a process in which actin filaments are sliding past myosin filaments [32, 33] (compare Figure 1.7, top and Figure 1.7, bottom) after an activation of myosin by the calcium transient during the action potential. The influx of Ca^{2+} during the action potential triggers a further calcium release from the sarcoplasmic reticulum. Calcium-binding proteins, such as troponin C buffer the cytosolic calcium increase, and the binding of calcium to troponin C causes a conformational change which allows the myosin heads to interact with the actin filaments in a process termed “cross-bridge cycling” which causes a contraction of the myofilaments [34] (see Figure 1.7, bottom). The relaxation of the

myofilaments takes place as the cytosolic calcium concentration decreases and unbinds from troponin C. The decrease of the calcium concentration in the cytosol is mainly driven by sarcoplasmic ATP-driven calcium pumps and the $\text{Na}^+/\text{Ca}^{2+}$ -exchanger ($\approx 95\%$), and only a minor fraction of calcium is removed from the cytosol via ATP-driven pumps of the cell membrane and uniport to the mitochondrion [35].

However, it is important to note, that not only the Ca^{2+} -transient magnitude and the unbinding process of calcium from troponin C are important for the contraction twitch, but also the length and rate of length change of myofilaments [36]. These effects of the myofilament length are caused by the length-dependent Ca^{2+} -sensitivity and unbinding rate of troponin C, and the effect that the maximum tension is also length-dependent.

Next, it is explained how deformation affects excitation processes.

1.7 Cardiac Mechano-Electrical Feedback

In the heart, waves of electrical excitation initiate its contraction. However, not only the excitation is coupled to the deformation of the medium; but also, the heart's deformation affects cellular excitation processes. This phenomenon is called "mechano-electrical-feedback" (MEF), and has been found to be able to induce but also to abolish dangerous heart arrhythmias [9].

The perhaps most important MEF effect emerges from mechano-sensitive ion channels, such as the stretch-activated channels in the cell membrane that induce stretch-activated currents (SACs). It has been shown in experimental and modeling studies that SACs promptly follow a stretch of cardiac tissue, and affect electrophysiological properties such as the resting potential, refractory period, the action potential duration and the restitution curve (dependency of the action potential duration on a stimulation frequency) [37]. It has further been demonstrated that SACs are arrhythmogenic, being able to cause premature ventricular excitations and early and delayed afterdepolarizations [38]. However, SACs can not only induce an action potential, but also cause a cell to become inexcitable via the accommodation phenomenon, and thus cause wave break [37]. Accommodation is the phenomenon that a relatively small depolarizing current increases the activation threshold of an excitable cell via inactivation of sodium currents [18, 39].

Another MEF mechanism is the effect of the myofilament length on the calcium dynamics [40]. A main effect of deformation on the calcium dynamics is the length-dependent buffer ability of troponin C which increases when myofilaments are stretched [36], which has been shown to alter the action potential

duration [41].

1.8 Reaction-Diffusion-Mechanics Models

To study basic effects of deformation on cardiac electrophysiology the reaction-diffusion-mechanics (RDM) framework has been introduced [7], which couples RD to mechanical equations. This approach requires to couple a RD model for cardiac excitability to models for the excitation-contraction coupling, mechano-electrical feedback, and the elasticity of the tissue. This chapter explains the basic ideas behind setting up a RDM model used to study cardiac electromechanics in this thesis.

1.8.1 Excitation-Contraction Coupling

Excitation-contraction coupling is a complex dynamical process, that couples the action potential with the different calcium transport systems to the mechanical changes of the length of myofilaments. However, as for models of cell excitability, one can use simplified models for excitation-contraction coupling, for example to study basic effects of deformation on wave propagation.

It is important to note, that there are two principal techniques used in cardiac modeling, the so called strongly coupled, and weakly coupled models [42]. In weakly coupled models the electrical activation is calculated independently from the mechanical problem, and used as input to solve the mechanical equations. Weakly coupled models are useful to study problems for which the mechano-electrical-feedback can be ignored. Yet, when the effect of deformation on the excitation processes needs to be considered, strongly coupled models must be applied. In the strongly coupled models the electrical activation is solved while taking the mechanical configuration into account [42].

In this thesis, two strongly coupled excitation-contraction models are used, a generic excitation-contraction model coupled to a FitzHugh-Nagumo-type model (chapters 2-4), and a biophysical model coupled to the ionic TP06 model (chapter 5).

A Generic Model

As a generic excitation-contraction model, a modified version of the Aliev-Panfilov model for the cardiac action potential was applied which has been introduced

in [7]. The equation of the contraction model is written as

$$\frac{\partial T_a}{\partial t} = \epsilon(u)(k_T u - T_a), \quad (1.10)$$

where T_a represents the active tension, u is the excitation variable of the Aliev-Panfilov model (see Eq. 1.7), and the parameter k_T controls the amplitude of the contraction twitch. This model ignores all effects but the direct effect of the calcium transient during the action potential, and thus is not suitable to study quantitative effects; however, the model is applicable to study basic effects of deformation in deforming cardiac tissue [43].

Niederer-Hunter-Smith model

As a biophysical excitation-contraction model, a numerically improved version of the Niederer-Hunter-Smith (NHS) model is applied in this thesis [36, 44]. The NHS model describes active tension in a sarcomere as a function of intracellular calcium concentration $[\text{Ca}^{2+}]_i$, sarcomere length, and the rate of sarcomere length change.

1.8.2 Cardiac Elasticity

In this section it is explained how the active tension resulting from the contraction of cardiomyocytes can be coupled to the elastic properties of cardiac tissue.

During the heart's activity its tissue undergoes substantial deformations, which requires the use of finite deformation theory in electromechanical models. Furthermore, cardiac tissue is a complex material to model, as it consists of individual cells that form layers of muscle fibers, which are tightly packed and organized by an extra-cellular matrix into branching sheet structures [45, 46]. Yet, the heart is not only non-homogeneous and anisotropic, but also is closely coupled to the blood flow. These complex effects make the engineering of efficient computational models for the elasticity of the heart a challenging research field [47]. There are two basic approaches to describe cardiac mechanics, continuum mechanics, and discrete mechanical modeling.

Continuum Mechanics

The principal idea of the continuous mechanical formulation of solid matter is to describe mechanics on mathematically infinitesimally small volume elements that possess some mass density and whose deformation can be described in terms of finite strain tensors. Physically these small volume elements should not be thought

as infinitesimally small, but big enough to contain sufficient molecules to be “continuous” [48]. The deformation of the small volume elements is caused by stress on the medium, which is a tensor property of the same rank as the strain tensor. The elastic material behavior is expressed in so called constitutive relations which connect a strain state to a particular stress state. Constitutive relations are normally determined experimentally and often expressed in terms of invariants of the deformation tensor. Continuum mechanics is typically formulated in terms of two coordinate systems, a coordinate system X_M which is deforming with the body, and a reference Cartesian coordinate system x_i [49]. A deformation state can then be described with a deformation tensor $C_{MN} = (\frac{\partial x_k}{\partial X_M})(\frac{\partial x_k}{\partial X_N})$, and finite strain can be described as Green’s strain tensor $E_{MN} = \frac{1}{2}(C_{MN} - \delta_{MN})$, where δ_{MN} is the unitary tensor.

An example for continuum mechanics used in RDM modeling of cardiac electromechanics is the Panfilov-Keldermann-Nash (PKN) model [7, 43]. The mechanical model of the PKN model is written as

$$\frac{\partial}{\partial X_M}(T^{MN} \frac{\partial x_j}{\partial X_N}) = 0, \quad (1.11)$$

$$T^{MN} = \frac{1}{2}(\frac{\partial W}{\partial E_{MN}} + \frac{\partial W}{\partial E_{NM}}) + T_a C_{MN}^{-1}, \quad (1.12)$$

where equation 1.11 describes the mechanical equilibrium of the body for a certain stress T^{MN} (second Piola-Kirchhoff stress), which is given by equation 1.12. T^{MN} consists of the active stress $T_a C_{MN}^{-1}$, where T_a is the active tension given by equation 1.10, and a passive stress. The passive stress is given as derivatives of the strain energy function W to components of Green’s strain tensor. In the PKN model the strain energy function is given by the Mooney-Rivlin constitutive relation $W = c_1(I_1 - 3) + c_2(I_2 - 3)$, where I_1 and I_2 are principal invariants of C , and c_1, c_2 are stiffness parameters [50].

The PKN model is used as an important benchmark for the discrete mechanical model that is used in this thesis.

Discrete Mechanical Modeling

In contrast to the continuous mechanical theory, the discrete mechanical formulation starts with the assumption of infinitesimally small points of matter that have some mass, and deformation is described in terms of force vectors [51]. Furthermore, the force acting on a mass point is assumed to be a function of the other mass points. The problem reads as

$$m_i \ddot{\mathbf{x}}_i = \mathbf{F}_i(\mathbf{x}_1 \dots \mathbf{x}_N, t), \quad (1.13)$$

where $\ddot{\mathbf{x}}_i$ is the acceleration of the mass point i with mass m_i , and \mathbf{F}_i is the force acting on this mass point, which is a function of the positions of other mass points

and time t . Equation 1.13 describes a dynamical many-body system in terms of a high-dimensional system of coupled ordinary differential equations, in contrast to the tensor formalism of the continuous mechanical formulation in equation 1.12.

Discrete models are successfully applied in physical systems in which the continuous formulation is not applicable, such as discontinuous deformations in fracture, plastic deformation, and mass mixing processes [52, 53]. Moreover, discrete models are computationally efficient, and therefore they are applied in computer graphics [54], medical tissue visualization [55], but also for the development of elasto-mechanical models of anisotropic materials [56] such as cardiac tissue [57, 58].

The emphasis of this thesis lies not on engineering a realistic elastic model for cardiac tissue, but on setting up a “minimal model” with elastic properties that we understand, which undergoes finite deformations, and whose numerical solution is efficient to compute. Therefore, an ideal crystal lattice of mass points connected with springs which follow Hooke’s law is used in this thesis. The model setup is described in detail in chapter 2.

The material properties of a mass-lattice model are given by the spring stiffnesses, the point masses, and the geometry of the mesh. The elastic properties of a material are normally described in terms of the constitutive relations of the continuous theory of mechanics. However a discrete description of mechanics can be translated into a continuous formulation using mechanical homogenization theory. Homogenization techniques can be applied to derive constitutive relations for mass-lattice models to apply them for cardiac tissue [59].

Please see chapter 2 on the setup of the discrete mechanical model used in this thesis, and numerical and computational issues for solving it.

1.8.3 Mechano-Electrical Feedback

SACs have been shown to rapidly follow stretch of cardiac tissue, and have been shown to be able to cause heart arrhythmia [9]. Therefore, some previous RDM modeling studies focused on SACs as a MEF effect, and identified important phenomena such as mechanically caused pacemaking activity [43], and the drift and breakup of spiral waves [60]. In this thesis the effect of SACs are also the main MEF effect that is studied; however, it is worth to mention that the NHS model, which is used in this thesis to describe excitation-contraction coupling, also describes the myofilament length-dependence of the Ca^{2+} -affinity of troponin C, which is also a MEF effect.

Stretch-activated currents

Experimental studies have shown that SACs are activated rapidly in cardiomyocytes undergoing stretch, and follow a linear current-voltage relationship [61, 62]. Linear models have been proposed for a stretch activated current I_s to describe SACs [63, 64], and used in previous electromechanical RDM modeling studies [43, 60, 65, 66]. The models developed in this thesis follow these assumptions, for example one model uses the equation

$$I_{sac} = G_s \frac{(\lambda - 1)}{(\lambda_{max} - 1)} (V - E_s), \text{ for } \lambda > 1 \text{ (stretch)} \quad (1.14)$$

where G_s is the maximal conductance, E_s is the reversal potential of the stretch activated channels, λ is the myofilament extension ratio. Parameter λ_{max} is the maximal myofilament extension ratio which is $\lambda_{max} \approx 1.1$ (cells can normally be stretched maximally by 10%) [65].

1.9 Reentrant Cardiac Arrhythmia and Spiral Waves

Cardiac arrhythmias are malfunctions in the regular electrophysiologic functioning of the the heart. Often, cardiac arrhythmias are caused by abnormal sources of excitation that disturb the healthy functioning of the heart. A source of electrical excitation is basically a pacemaker similar to the auto-oscillating sino-atrial node of the heart. Such a pacemaking source is illustrated in Figure 1.8A, where a auto-oscillating source is located in the center and rhythmically initiates radially spreading waves. The atrial and ventricular tissue are normally not auto-oscillating; however, there is another possibility, which is in fact cause of dangerous types of arrhythmia, the emergence of reentrant sources of excitation ¹.

1.9.1 Reentry

Reentry is an important concept in cardiology which has been subject of study since 1913 when Mines formulated the idea that a cell can undergo an oscillating excitation rhythm, if a wave would propagate around a closed circle of tissue (see Figure 1.8B) [68]. Note that the theory of Reentry of Mines is a one-dimensional formulation of reentry. The closed circle can be thought of a closed cable of the form illustrated in Figure 1.6. The theory of reentry was extended by Wiener and Rosenblueth [69] to two dimensions. In Figure 1.8C this two-dimensional theory of reentry is illustrated. One can see, that a reentrant excitation can occur in a two-dimensional medium when an obstacle is present around which a spiral

¹For an extensive review on the theory of reentry see [67]

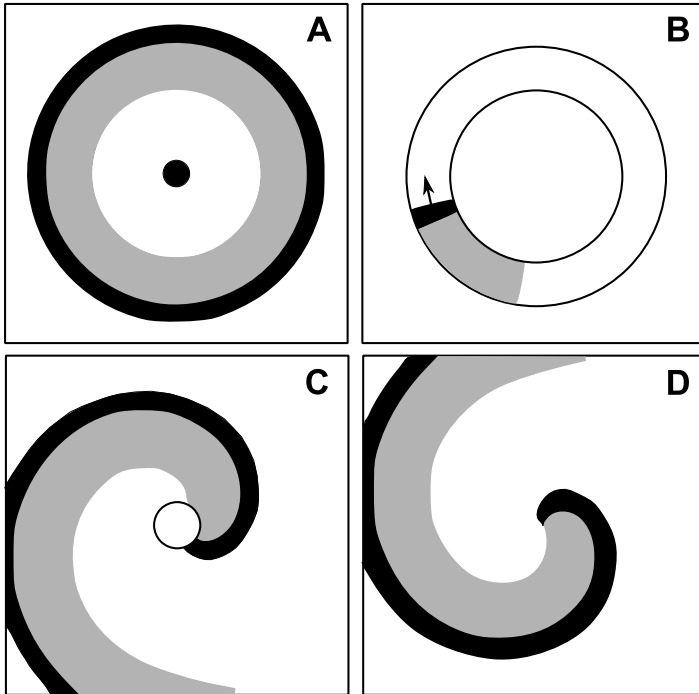


Figure 1.8. Abnormal wave sources. (A) Pacemaking activity. (B) One-dimensional reentry. (C) Two-dimensional reentry around obstacle. (D) Spiral wave reentry. Black represents wave's front, gray the wave's back.

wave can rotate. This type of reentry is termed “anatomic reentry” as it requires an anatomic substrate forming the obstacle. However, it turned out that reentry is also possible in a medium without an obstacle, as a wave can propagate around its own refractory tail. This idea has been introduced by Selfridge [70] and describes a spiral wave, also called “functional reentry”. Spiral wave reentry is illustrated in Figure 1.8D.

1.9.2 Spiral Wave Initiation

To understand the basic mechanisms for spiral wave formation it is important to emphasize the most striking difference between a spiral wave and a “normal” wave. In a normal wave the front and the back are always spatially separated by a refractory region, whereas in a spiral wave there is a special point (in two dimensions) where the wave front directly neighbors the wave back. Such special points are often called “spiral wave tips” or “phase singularities”.

Inhomogeneities

It has been shown that wave breaks, that cause phase singularities and thus spiral waves, can occur due to heterogeneities in excitation properties in the medium. An example of spiral wave initiation which was found by Krinsky [5] due to an inhomogeneity in refractory period in the medium is shown in Figure 1.9(A-C). In this mechanism wave break occurs, because the second wave cannot propag-

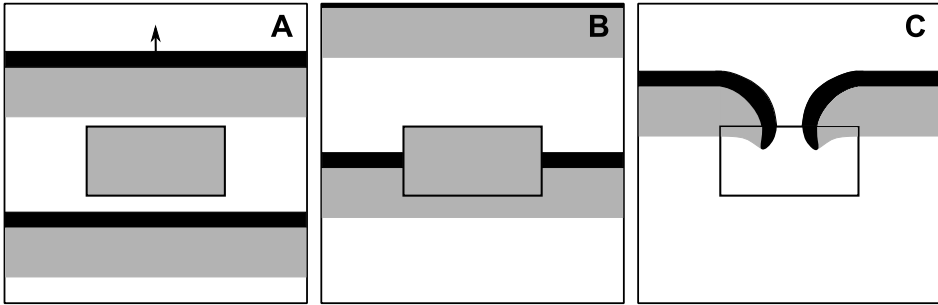


Figure 1.9. Spiral initiation due to a heterogeneity in refractory period. The heterogeneity with elongated refractory period is shown as a rectangle. (A) Two connected waves propagate through the medium, the medium in the inhomogeneity is refractory from the first wave, (B) and causes a wave break of a second wave, (C) which results in two counter-rotating spiral waves.

ate into the inhomogeneous region which has a longer refractory period, if the interval between the first and the second wave is short. After some while, the two wave fronts that resulted from the wave break, can enter the previously inexcitable region and form two counter-rotating spiral waves.

Another mechanism of spiral formation in a setup used also in this thesis is illustrated in Figure 1.10. Here, the wavefront cannot follow the boundary of the medium, it detaches from it and forms a spiral wave.

Vulnerability

An important intrinsic property of excitable media is the so called vulnerability phenomenon: a single stimulation in an excitable medium may cause the formation of spiral waves of excitation [71]. Such a scenario is possible when a local stimulation is applied at the refractory tail of a preceding wave [Figure 1.11A]. A wave initiated by this stimulation cannot propagate forward (due to refractoriness). As a result, the wave breaks and two counter-rotating spiral waves are formed [Figure 1.11B].

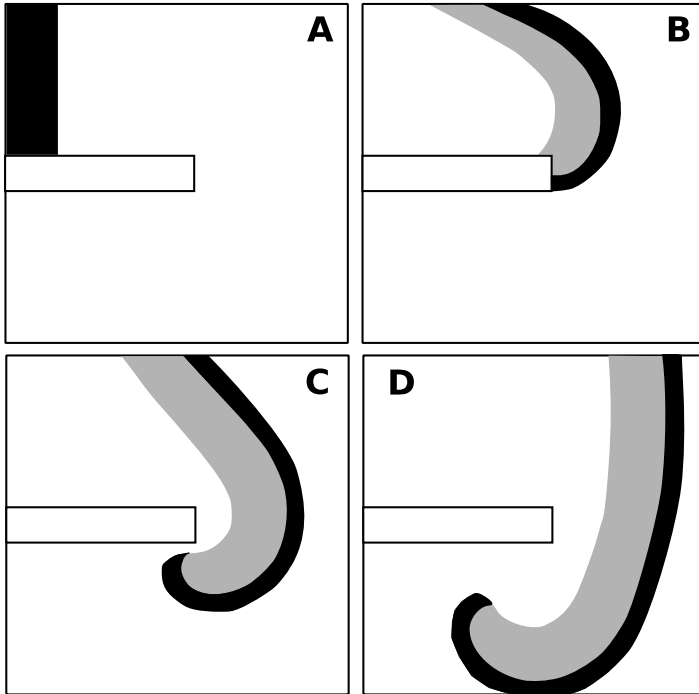


Figure 1.10. Spiral activity caused by an obstacle due to an introduction of a critical curvature

1.10 Motivation

The main question of this thesis is “how does deformation affect the onset of reentrant cardiac arrhythmia?”. It is not yet known what effect deformation has on known mechanisms of spiral wave initiation, or what new mechanisms might emerge taking deformation into account. For example, it has not been studied yet, how deformation affects the vulnerability phenomenon, or how mechanical heterogeneity can be arrhythmogenic. These questions are approached by means of the mechanically discrete RDM models developed in this thesis.

1.11 Outline

In chapter 2 a generic discrete RDM (dRDM) model is formulated to study the basic effects of deformation in excitable media. The dRDM model couples a modified Aliev-Panfilov model to a discrete mechanical model which follows the Seth

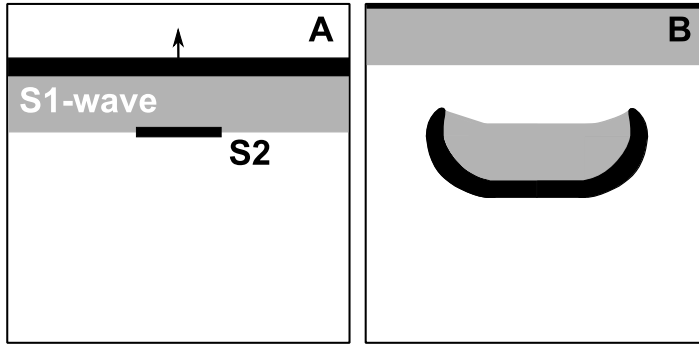


Figure 1.11. Classical vulnerability. (A) A stimulation S_2 is applied in the refractory tail of a propagating wave (“ S_1 -wave”), (B) which results in unidirectional wave block, initiating two counter-rotating spiral waves.

material relation. The value of the dRDM approach is demonstrated in a study on mechanically caused pacemaking activity, where important phenomena are reproduced, that were previously found in a RDM study using a continuous RDM model (PKN model) [43].

In chapter 3 the dRDM model is applied to study the influence of deformation on the vulnerability of cardiac tissue. It turns out here that deformation alters the classical vulnerable zone and causes a new one at longer coupling intervals, which results in a new mechanism for spiral wave initiation. It is demonstrated that the new mechanism of spiral wave formation may cause auto-generation of spiral waves in situations when a curvature is introduced to a wave, for example when it undergoes a diffraction or a deflection.

In chapter 4 the importance of mechanical heterogeneity for the onset of reentrant arrhythmia is studied. This study also employs the dRDM formulation, and in addition introduces mechanical heterogeneity. It is shown that spiral waves emerge due to a local inhomogeneity which is varied in active and passive mechanical properties in a large range of these parameters via five mechanisms. The importance of mechanical heterogeneity for the onset of cardiac arrhythmia is discussed.

In chapter 5 a new model to study electromechanical cardiac functioning is introduced. The model combines state of the art biophysical models for cardiac excitation and contraction, with the generic discrete mechanical formulation which is also used in the generic dRDM model of the previous chapters.

Chapter 6 gives a summary and discussion of this thesis.

Chapter 2

A Discrete Model to Study Reaction-Diffusion-Mechanics Systems

LOUIS D. WEISE¹, MARTYN P. NASH² AND ALEXANDER V. PANFILOV³ (2011)

¹Theoretical Biology & Bioinformatics, Utrecht University, Utrecht, The Netherlands

²Auckland Bioengineering Institute and Department of Engineering Science,
The University of Auckland, Auckland, New Zealand

³Department of Physics and Astronomy, Ghent University, Ghent, Belgium

PLOS One, 6(7): e21934

Abstract

This article introduces a discrete reaction-diffusion-mechanics (dRDM) model to study the effects of deformation on reaction-diffusion (RD) processes. The dRDM framework employs a FitzHugh-Nagumo-type RD model coupled to a mass-lattice model, that undergoes finite deformations. The dRDM model describes a material whose elastic properties are described by a generalized Hooke's law for finite deformations (Seth material). Numerically, the dRDM approach combines a finite difference approach for the RD equations with a Verlet integration scheme for the equations of the mass-lattice system. Using this framework results were reproduced on self-organized pacemaking activity that have been previously found with a continuous RD mechanics model. Mechanisms that determine the period of pacemakers and its dependency on the medium size are identified. Finally it is shown how the drift direction of pacemakers in RDM systems is related to the spatial distribution of deformation and curvature effects.

2.1 Introduction

Reaction-diffusion (RD) partial differential equations describe important spatio-temporal phenomena, including waves and patterns in a variety of chemical, physical, and biological systems. Important examples of these phenomena include waves in the Belousov-Zhabotinsky (BZ) reactions [12, 72], waves of CO oxidation on platinum surfaces [13], waves of spreading depression in nerve tissue [14], and the morphogenesis of *Dictyostelium discoideum* (Dd) [15, 73]. In the heart, electrical waves of excitation propagate through the tissue and initiate its contraction. RD-equations have been successfully applied to model normal and abnormal wave propagation in cardiac tissue, such as rotating spiral waves, whose initiation may result in life-threatening arrhythmias [3, 72]. In many of the systems mentioned above, wave propagation is accompanied by a deformation of the medium. Important examples include the chemotactical motion of cells during Dd-morphogenesis [73], the swelling and deswelling of a polymeric gel in the BZ reaction [74] and the contraction of the cardiac muscle [17]. As the heart contracts, its deformations feed back on the process of wave propagation. This important phenomenon, called mechano-electrical feedback, has been extensively studied in cardiac electrophysiology [9].

To model the effects of deformation on wave propagation in RD systems, it is necessary to describe the underlying mechanical phenomena in terms of the RD process. As such, a coupled reaction-diffusion-mechanics (RDM) framework was introduced in [7] and applied to study cardiac tissue. In particular, the RD equations were combined with the equations of finite deformation continuum mechanics. With this approach several important effects of deformation on wave propagation were identified such as self-organized pacemakers, spiral wave drift, and break-up of spiral waves [43, 60].

Continuum mechanics is among the most valuable and widely used approaches in engineering and modeling studies, however, it does not explicitly describe the particular micro-organization of a medium, which might be important for certain aspects of RDM systems. Cardiac tissue, for example, consists of individual cells that form layers of muscle fibers, which are tightly packed and organized by an extra-cellular matrix into branching sheet structures [45, 46]. To study how this affects the elastic properties of the heart, discrete models with similar micro-structure need to be developed. Discrete models are computationally efficient and widely used in various applications such as computer graphics [54], medical tissue visualization [55], and the development of elasto-mechanical models of anisotropic materials [56] such as heart tissue [57, 58]. Discrete models are also used to describe discontinuous deformations in the case of fracture, plastic deformation, and mass mixing processes [52, 53].

In this paper, discrete elastic modeling is coupled with FitzHugh-Nagumo-type

RD partial differential equations to study RDM systems. First, the process of the setting up of the discrete RDM (dRDM) model is described in detail, and computational and numerical aspects are addressed to discuss the macroscopic elastic properties of the medium. Secondly, as an illustration of the new modeling approach, the dRDM model is applied to study pacemaking activity in the RDM system shown in [43]. This illustration demonstrates that the dRDM model adequately reproduces all of the important phenomena of pacemaker dynamics previously found with a continuous RDM model [43]. The computational efficiency of the dRDM approach allows more detailed investigations into the mechanisms determining important properties of the pacemaking activity. Next, the factors determining the period and drift of the pacemakers found in [43] were identified. Overall, the value of the dRDM modeling approach, as a tool to study RDM systems, is demonstrated.

2.2 Methods

2.2.1 Reaction Diffusion Model for Cardiac Excitation

In this paper, as in [43], the Aliev-Panfilov model [28] for cardiac excitation is used as the RD part of the dRDM model. Of course the same approach can easily be applied to any RD model describing cardiac excitation or any other reaction-diffusion process. The purpose of using a cardiac RD model is to reproduce the time course of the transmembrane potential. The transmembrane potential changes due to ionic currents, which flow through voltage-gated ion channels of the cardiac cell membrane. The reaction part of the model describes these currents either in a general form (in low dimensional models) or on the basis of detailed experimental data (ionic models). The spatial coupling between cells in the RD approach is demonstrated by the Laplacian operator [22]. The Aliev-Panfilov model [28] provides a low-dimensional description of excitation for cardiac cells. The equations of this model are

$$\frac{\partial u}{\partial t} = \nabla^2 u - ku(u - a)(u - 1) - uv - I_s \quad (2.1)$$

$$\frac{\partial v}{\partial t} = \epsilon(u)(ku - v), \quad (2.2)$$

where u and v are normalized representations of the transmembrane potential and the conductance of a slow repolarizing current, respectively. These variables are quantified in this paper in dimensionless units, for u excitation units [e.u.], and for v recovery units [r.u.] are used. The term $-ku(u - a)(u - 1)$ in Eq.2.1

describes the fast excitation process of the AP. The parameter a represents the threshold of activation and parameter k controls the magnitude of the transmembrane current. In this study, $a = 0.05$ and $k = 8$ were used in all computations. $\epsilon(u)$ is a step function setting the time scale of the recovery and the contraction process: we set $\epsilon(u) = 1$ for $u < 0.05$, and $\epsilon(u) = 0.1$ for $u \geq 0.05$ (also used in Eq.2.3). The term $-uv$ describes the repolarizing current of the recovery process. The term I_s is the stretch activated depolarizing current described in Eq.2.9. In a non-deforming medium Eqs.2.1,2.2 with these parameter values describe non-oscillatory cardiac tissue providing stable propagation of excitation waves.

2.2.2 Excitation-Contraction Coupling Model

Following [43] the excitation-contraction coupling is modeled using

$$\frac{\partial T_a}{\partial t} = \epsilon(u)(k_T u - T_a), \quad (2.3)$$

where T_a modulates the active contraction force in Eq.2.5 to associated mass points of the medium. The parameter k_T controls the amplitude of the contraction twitch, where $k_T = 1.5$ was used in all simulations. The identical term Eq.2.3 was used in the continuous RDM modeling approach of Panfilov et al. [43] to account for the active stress. The model formalism of Panfilov et al. from [43] is an important benchmark for the dRDM model in this paper, and is referred to in the following text as the PKN description.

2.2.3 Mass-Lattice Model

To model the mechanical properties in the dRDM approach a 2D lattice that consists of material points connected by springs (Figure 2.1A) is used. The unit cell of this 2D lattice is shown in Figure 2.1B. Each mass point is connected to its four nearest neighbours in horizontal and vertical directions at resting distance r_0 and to its four next-nearest diagonal neighbors at resting length $\sqrt{2}r_0$. All springs follow Hooke's force-displacement relation and horizontal and vertical springs may produce additional active contraction forces. Following the continuous PKN approach [7], elastostatics is assumed in this dRDM model, i.e. the stationary deformations corresponding to each given configuration of active forces and boundary conditions are computed. The procedure is outlined as follows. At steady state, the total force at each node is zero. If the configuration of the active forces is changed, the force balance at the mass points will be violated which results in the motion of the mass points to a new stationary configuration. For efficient computations of this system, viscous forces were added to dampen possible oscillations.

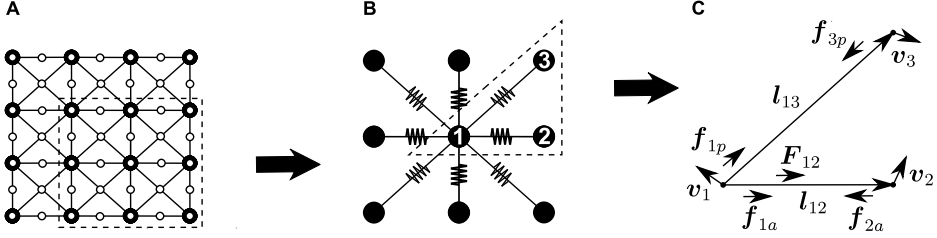


Figure 2.1. (A) **Coupled mechanical and RD mesh.** Coupled mechanical and RD mesh. The mass points are indicated as large black dots. The finite difference points to solve Eqs.(2.1)-(2.3),(2.9) are indicated as small white dots. The lattice springs are indicated as black lines. (B) **Unit cell of the 2D lattice.** Mass point 1 and its four horizontal and vertical nearest neighbors and four diagonal next-nearest neighbors are connected with direct active and diagonal passive springs. Lattice springs are indicated by zigzagging lines (fat lines for active and thin lines for passive springs). Dotted contours indicate insets for the associated subfigures. (C) **Vectors used in Eqs.(2.4)-(2.6)** for calculating lattice interactions.

The formal formulation of the approach is given below: Figure 2.1C demonstrates main forces and the displacements of active and passive lattice springs connecting the mass point 1 to the mass points 2 and 3. The positions of the mass points are given by \mathbf{x}_1 , \mathbf{x}_2 , \mathbf{x}_3 , with the corresponding velocities \mathbf{v}_1 , \mathbf{v}_2 and \mathbf{v}_3 . Mass points 1 and 2 are connected by an active spring. The force generated by this spring on the mass points is given by

$$\mathbf{f}_{1a} = -\mathbf{f}_{2a} = \left[c \left(\frac{\|\mathbf{l}_{12}\| - r_0}{r_0} \right) - d \frac{(\dot{\mathbf{l}}_{12} \cdot \mathbf{l}_{12})}{\|\mathbf{l}_{12}\|} \right] \frac{\mathbf{l}_{12}}{\|\mathbf{l}_{12}\|} + \mathbf{F}_{12}, \quad (2.4)$$

where $\mathbf{l}_{12} = \mathbf{x}_2 - \mathbf{x}_1$ is a vector along an active spring, $\dot{\mathbf{l}}_{12} = \mathbf{v}_2 - \mathbf{v}_1$ is the time derivative of the spring vector \mathbf{l}_{12} , parameters c and d are the stiffness and “damping” constants, respectively ($c = 1$ in all simulations), and \mathbf{F}_{12} is the active force between mass points 1 and 2 given by

$$\mathbf{F}_{12} = \left(\frac{T_a(1) + T_a(2)}{2} \right) \frac{\mathbf{l}_{12}}{\|\mathbf{l}_{12}\|}, \quad (2.5)$$

where $T_a(i)$ is the value of variable T_a from Eq.2.3 at mass point i . Mass points 1 and 3 are connected by a passive spring. The force generated by this spring is given by

$$\mathbf{f}_{1p} = -\mathbf{f}_{3p} = \kappa \left[c \left(\frac{\|\mathbf{l}_{13}\| - \sqrt{2}r_0}{\sqrt{2}r_0} \right) - d \frac{(\dot{\mathbf{l}}_{13} \cdot \mathbf{l}_{13})}{\|\mathbf{l}_{13}\|} \right] \frac{\mathbf{l}_{13}}{\|\mathbf{l}_{13}\|}, \quad (2.6)$$

where $\kappa = 1/2$ is the stiffness ratio between active and passive springs. It is assumed that each node here is subject to Newton's law of motion:

$$\sum_{\alpha=1}^N \mathbf{f}_{i\alpha} = m\ddot{\mathbf{x}}_i, \quad (2.7)$$

where N is the number of springs connected to mass point i , m is the mass of a point, and α indicates connected springs. By solving Eq.2.7 to mechanical equilibrium ($\sum_{\alpha=1}^N \mathbf{f}_{i\alpha} = 0$), the steady state configuration of the lattice for each given distribution of active forces generated by the RD process is found. Note that the "mechanical" time variable τ , as well as the parameters viscosity d and the mass of a node m , have no physical relevance in this model, but each fulfill a pure numerical role. The mass m of each mass point was set to 1 (dimensionless mass units).

Material Properties

The elastic mechanical properties of the dRDM model are determined by the geometry of the lattice unit cell and the stiffness of the springs. In classical continuum mechanics, elastic properties are represented by constitutive relations between the corresponding stress and strain tensors. Constitutive relations are successfully used to describe the elastic properties of many materials including biological tissues. It is possible to formulate the elastic properties of this paper's mass-lattice model in terms of an equivalent continuous material. The mass-lattice model (Figure 2.1B) in this paper was extensively studied for various aspects of elasticity. In most cases the mass-lattice model was studied under conditions of small deformations (linear elasticity). The relation between stress and small strain of this mass-lattice model was shown to be expressible in the form of a 4th rank elasticity tensor C_{ijkl} , and its coefficients can be directly derived from the spring constants of the system [75]. Furthermore, it was demonstrated by Schargott et al., that if the stiffness ratio is $\kappa = 1/2$, the lattice is macroscopically isotropic [76]. This implies that the linear elasticity tensor is rotationally invariant. In this case the constitutive relations simplify to the generalized Hooke's law [76]

$$\sigma_{ij} = C_{ijkl}\epsilon_{kl} = 2\mu\epsilon_{ij} + \lambda(\mathbf{tr}\epsilon)\delta_{ij}, \quad (2.8)$$

where ϵ_{kl} are elements of the small-strain tensor ϵ , δ_{ij} is the Kronecker delta and λ and μ are the Lamé coefficients, which in this case are equal to each other [76]. The elastic coefficients of this material are Young's modulus $E_{2D} = 4/3c$ (where c is the spring stiffness as defined above), and Poisson's ratio $\nu_{2D} = 1/3$ (see [76]). An extension of this material relation for finite deformations can be found in [77]. Krivtsov et al. explained in [77], that even for non-linear deformations, the elastic properties of the mass-lattice model used in this paper can be approximated by a generalization of Hooke's law for finite deformations (Seth material) [78]. The Seth material relation is similar to Eq.2.8 but uses the Almansi strain tensor for finite deformations instead of the small strain tensor ϵ . Therefore, for $\kappa = 1/2$ used in the simulations of this paper, the mass-lattice model is applicable for the description of an isotropic material undergoing non-linear deformations.

Numerical studies were performed to illustrate the material properties for conditions used in this paper's simulations. A deformation field was created by applying a force at the central mass point of an extended 2D lattice, whose boundaries were fixed in space (isometric boundary conditions), leading to finite displacements and local deformations. Next, Eqs.2.4-2.7 were solved to mechanical equilibrium and the displacement of the mass point from its initial position and the angle between the force and the displacement vector were calculated. Similar computations were performed for different orientations and amplitudes of the force vector. This comparison (Figure 2.2A) demonstrates that the 2D mass lattice model used in this paper can be considered as a good approximation to a macroscopically isotropic material, at least for local deformations of up to 24%. The displacement error for 15% local deformations was 0.6%, and for 24% local deformations 1.7% (Figure 2.2C). The angle deviation of the displacement vector and the applied force was $< 0.6\%$ for maximal local deformations up to 15% (data not shown). Furthermore, Figures 2.2A and 2.2B demonstrate, that a linear relationship between force and maximal local deformation, and between force and the displacement of the central mass point holds true for the whole range of studied force amplitudes, i.e. up to maximal studied local deformation of 24%. In summary, the mass-lattice model described here with $\kappa = 1/2$ describes an isotropic medium, which follows a linear force-displacement relation that can be approximated by the Seth material relation.

2.2.4 Electromechanical Feedback

The deformation of cardiac tissue alters the process of wave propagation. It has been shown in studies of excised cardiac tissue and the whole heart that the direct physiological influence of contraction on cardiac tissue is given by a depolarising stretch-activated current I_s through stretch activated channels [9]. Experimental studies have shown, that these channels are activated instantaneously with mechanical stretch and follow a linear current-voltage relationship [61, 62]. Linear

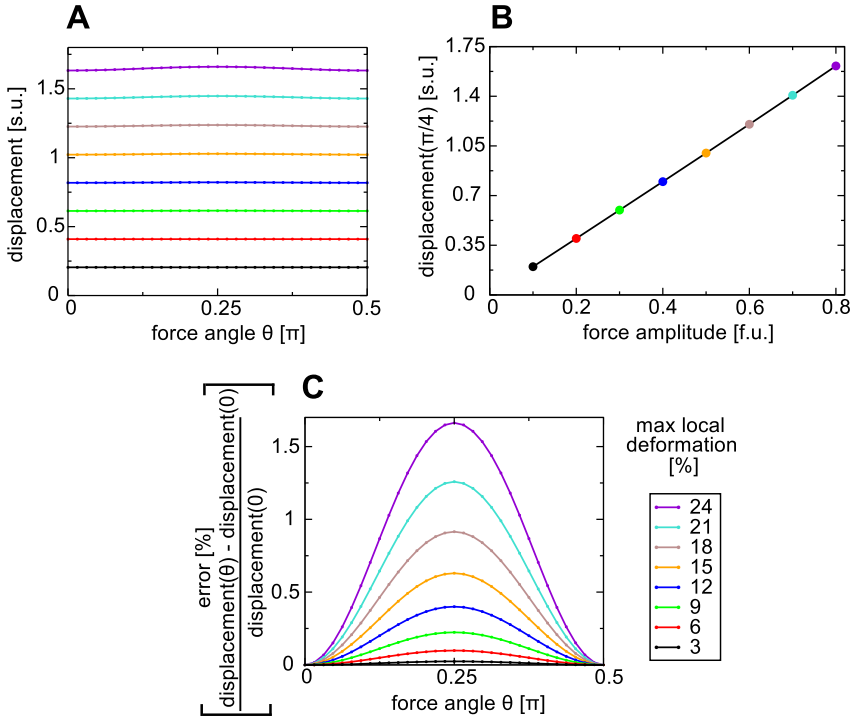


Figure 2.2. Seth material relation. A force was applied at the center point for different amplitudes and 32 orientations θ between 0 and $\pi/2$. An angle of $\theta = 0$ corresponds to a force perpendicular to the border. **(A)** Isotropy: displacement is approximately constant for different force angles θ over a range of force amplitudes. **(B)** Displacement of the center point vs force amplitude (at $\theta = \pi/4$). **(C)** Error of displacement (relative to displacement at $\theta = 0$) vs force angle θ . For these simulations a system size of 79.2 *s.u.* and $thr = 1e - 6$ *f.u.* were applied.

models have been proposed for I_s [63, 64], and have also been applied in other electromechanical models [43, 60]. Following these previous studies the equation

$$I_s = G_s(\sqrt{A} - 1)(u - E_s) \quad (2.9)$$

is used where G_s and E_s are the maximal conductance and reversal potential of the stretch activated channels. Following [43, 60], $E_s = 1$ was chosen. A is the surface area of a quadrilateral formed by 4 neighboring mass points (see Figure 2.1A) normalized using the reference surface area of this quadrilateral in undeformed state (r_0^2 *s.u.*²). The stretch activated current is active only if $A > 1$ (stretch). The value of G_s is a main determinant of the effect of I_s . The value $G_s = 1.5$ was used for all computations in this paper unless stated

otherwise.

2.2.5 Numerical Methods

The dRDM model was solved using a hybrid approach, combining an explicit Euler scheme for the RD Eqs.2.1-2.3,2.9 with a Verlet integration scheme [79] to solve the equations for the motion of the mass points Eqs.2.4-2.7. The position of a mass point i for the integration time $\tau + m\tau$ is computed by

$$\mathbf{x}_i(\tau + m\tau) = 2\mathbf{x}_i(\tau) - \mathbf{x}_i(\tau - m\tau) + \ddot{\mathbf{x}}_i(\tau) \times (m\tau)^2,$$

where $m\tau = 0.01$ is the Verlet integration time step and τ is the integration time. For the very first computation

$$\mathbf{x}_i(0 + m\tau) = \mathbf{x}_i(0) + \frac{1}{2}\ddot{\mathbf{x}}_i(0) \times (m\tau)^2$$

was used. The acceleration of a mass point $\ddot{\mathbf{x}}_i(\tau)$ is given by Eq.2.7. At each time step the velocities of the mass points are calculated by

$$\mathbf{v}_i(\tau) = \frac{\mathbf{x}_i(\tau) - \mathbf{x}_i(\tau - m\tau)}{m\tau}.$$

The solution procedure of the dRDM model is as follows: after *esr* time integration steps for the RD model and electromechanical feedback (Eqs.2.1-2.3,2.9), the equations of the mechanical model (Eqs.2.4-2.7) are solved for all of the springs until the sum of forces for each mass point is under the convergence threshold *thr* (dimensionless force units [f.u.]). Euler computations were performed on a quadratic deforming grid of finite difference points using no-flux boundary conditions. For all simulations, an Euler integration time step of $ht = 0.001$ (dimensionless time units [t.u.]) and a space integration step of $hx = hy = 0.3$ (dimensionless space units [s.u.]) were used. Each surface area element A consists of 2×2 directly neighboring mass points and 3×3 electrical grid points (Figure 2.1A). For grid points at the boundary of two (or more) surface area elements A , the average value of these normalized surface areas was used to compute I_s (Eq.2.9). When solving the mechanical equations 2.4-2.7, the boundaries of the medium were fixed in space. This approach is commonly applied in computational studies on cardiac physiology [43, 60]. It corresponds to the isometric contraction in tissue experiments, and is similar to the isovolumic phases of the cardiac cycle at the whole organ level.

2.2.6 Model Validation

For the integration of the dRDM model Eqs.2.1-2.7, 2.9 several parameters of the numerical scheme were chosen. This section demonstrates how parameters were set to assure accurate and efficient computations.

RD Integration Parameters

The RD Eqs.2.1-2.3 were solved using the finite difference approach with an explicit Euler integration scheme. Previous studies of the Aliev-Panfilov RD model used space steps of $hx = 0.6$ [43] to $hx = 1.0$ [80]. To assure high spatial resolution of the dRDM model, a space step of $hx = 0.3$ was used in this study. A time step of $ht = 0.001$ was applied to assure efficient computation of the coupled mechanical model Eqs.2.4-2.7 (see following section “Electrical and Mechanical Grids”).

Damping-Stiffness-Ratio and Verlet Integration Time Step

The equations describing the motion of the mass points Eqs.2.4-2.7 represent a system of coupled, driven, damped oscillators. As elastostatics was assumed in this work, the damping-stiffness ratio d/k in this case is just a numerical parameter that controls the rate of convergence of the lattice mass points to their equilibrium positions. It seems logical to use the largest possible value of d/k to assure the fastest possible convergence. However, large values of d/k lead to numerical instabilities, because of the counter-play of the elastic and viscous forces. It was found that the use of $d/k = 30$ resulted in fast convergence of Eq.2.7, with no numerical instabilities and convergent results, so this ratio was used for all simulations in this paper. For solving the mechanical Eqs.2.4-2.7 an integration time step of $m\tau = 0.01$ was used, which was found as the maximal time step that allowed fast stable convergence of the lattice mass points to their new configuration.

Electrical and Mechanical Grids

In RDM systems, the deformation is more smoothly distributed in space compared to the state variables of the RD equations [7]. It is therefore possible to use a coarser grid for the solution of the elastostatics equations compared to the integration of the RD equations. Furthermore, the slower mechanical dynamics enabled the update of the mechanical configuration after a number of RD integration steps had been performed [7]. To appropriately choose the parameters

that define the relation between the mechanical and RD grids, one must understand how they affect the accuracy of the simulations. These parameters include: the “mechanical update rate” esr (number of RD integration steps after which the new mechanical configuration is computed), and the “spatial resolution” of the mechanical grid (the relative resolution of the mechanical and RD grids). The spatial resolution is expressed as the ratio of the total number of mechanical nodes to the total number of RD nodes. This means, that if the mechanical grid is twice ($emr = 2$) as coarse as the RD grid, then the ratio of total numbers of nodes will be $1 : 4$ (in general $1 : emr^2$ in 2D). Additionally, the accuracy of the solution of Eq.2.7 also affects the mesh coupling and the accuracy of the dRDM model. The accuracy for the solution of Eq.2.7 is characterized via a threshold parameter thr , which determines the convergence of the system to elastostatics (the sum of forces at each mass point must be smaller than thr *f.u.*). In order to determine how these parameters affect the accuracy of the dRDM model, the following numerical experiment was performed: First, deformation patterns that occurred during the stable rotation of a spiral wave for the duration of 10 *t.u.* (which is $\approx 1/3$ period) were selected as the reference solution. These reference patterns were calculated with the integration parameters listed in the caption of Figure 2.3. Next, an investigation of how less accurate parameter settings affect the accuracy of the solutions was performed. This procedure was applied for various parameter sets and the trajectories of $M = 49$ mass points equally distributed in the medium were traced (Figure 2.3A). The deviation of these trajectories was computed from the reference solution for each simulation time step t . To estimate the mean absolute error of the mass points for a time step t an “instantaneous” error norm ME_t was defined as

$$ME_t := \frac{\sum_{m=1}^M \|\mathbf{x}_{tm}^{ref} - \mathbf{x}_{tm}\|}{\sum_{m=1}^M \|\mathbf{x}_{tm}^{ref} - \mathbf{x}_m^0\|}, \text{ for } \sum_{m=1}^M \|\mathbf{x}_{tm}^{ref} - \mathbf{x}_m^0\| \neq 0, \quad (2.10)$$

where \mathbf{x}_{tm} is the position of mass point m at time step t for a given solution, \mathbf{x}_{tm}^{ref} is the corresponding position of this mass point for the reference solution, and $\|\mathbf{x}_{tm}^{ref} - \mathbf{x}_m^0\|$ is the displacement of the point m from its initial position for the reference solution, and $\|\mathbf{x}_{tm}^{ref} - \mathbf{x}_{tm}\|$ is the difference between the given and the reference solution for point n at time step t . To estimate the total mean error, an error norm TME for the whole experiment over T time steps was defined as

$$TME := \sum_{t=1}^T ME_t, \text{ for } \sum_{m=1}^M \|\mathbf{x}_{tm}^{ref} - \mathbf{x}_m^0\| \neq 0. \quad (2.11)$$

Note that for testing patterns used here, the instantaneous error norm ME_t did not vary significantly during the studied time period (data not shown). Therefore, it is adequate to use TME to approximate the total mean error. In Figure 2.3B the effect of thr on TME is shown. For $thr = 2e - 5$ *f.u.* the estimated total

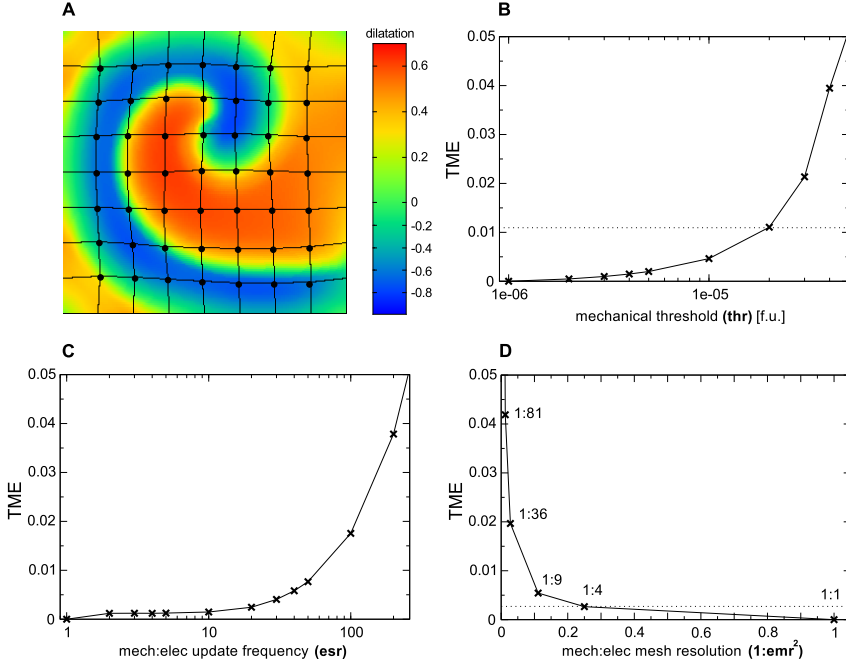


Figure 2.3. Determining mesh parameters. (A) Experimental setup: trajectories of 49 mass points (large big dots) are traced during a spiral wave rotation during 10 $t.u.$ in a medium size of 43.2 $s.u.$ along each side. The color spectrum indicates (local) dilatation (scaled) in the medium ($10 \times (\sqrt{A} - 1)$). Maximal local deformations 15%. (B) TME vs thr with $emr = 2$, $esr = 1$ and using $xthr = 1e - 6$ $f.u.$ to compute reference trajectories. The dotted horizontal line indicates the parameter chosen for further computations ($thr = 2e - 5$ $f.u.$). (C) TME vs. esr with $thr = 1e - 5$ $f.u.$, $emr = 2$, and $esr = 1$ to compute reference trajectories. (D) TME vs. $1 : emr^2$ with $thr = 1e - 5$ $f.u.$, $esr = 1$ and $emr = 1$ to compute reference trajectories.

mean error due to this parameter variation was about 1%. Figure 2.3C shows the influence of the mechanical update rate esr on the accuracy of the model. As a result, the total mean error due to this parameter is expected to be less than 0.2% when $esr < 10$. However, for this study we chose to fix $esr = 1$, because of the observation that the more frequent update of the mechanical grid (together with a small time step to integrate the RD equations) resulted in significantly faster convergence of the iteration procedure and hence decreased the overall simulation time (data not shown). Figure 2.3D shows the effect of the relative spatial resolution of the mechanical and electrical grids on TME . For $emr \leq 2$, the TME is around 0.3%. Based on that the parameters were chosen to: $thr = 2e - 5$ $f.u.$, $esr = 1$ and $emr = 2$. In summary, this parameter choice is expected to cause a total mean error of around 1% mainly due to the choice of the mechanical

threshold thr .

2.2.7 Computational Performance

This section analyses and compares the computational performance of the dRDM and PKN approaches. In particular, the scaling of the computational times for the two modeling schemes versus the number of mechanical nodes N_{MN} was investigated using the following simulations. A radially spreading wave was initiated at the center of an excitable medium using a point stimulus and the subsequent activity was simulated for a duration of 10 $t.u.$ using serial processing on a personal computer with a 3.33GHz Intel Xeon X5680 processor. To compare the computational scaling, we used identical mechanical and electrical grids for both models, with $hx = 0.6 s.u.$ and $emr = 2$. Even though a direct comparison of the nodal resolutions of both modeling approaches (mass points for dRDM and finite elements for PKN) is difficult in terms of mechanical accuracy, it is important to note that the calculation of stretch activated current I_s (Eq.(1.14)) is directly affected by the resolution of the mechanical nodes.

Figure 2.4 illustrates computation time [s] plotted against the system size for the different approaches. For the PKN model, the computation time increased non-linearly with the number of finite element mesh nodes. This was primarily due to the N-squared scaling for the solution of the linearised equations, whilst the element stiffness calculations scaled approximately linearly (data not shown). On the other hand, for the dRDM models the total CPU-time increased approximately linearly with the number of lattice mass points for the system sizes considered here (linear regression analyses showed R^2 values larger than 0.98). Furthermore, the positions of the mechanical nodes for the dRDM simulations ($ht = 0.001 t.u.$, $esr = 1$) were updated 90 times more frequently than the nodes of the PKN model ($ht = 0.03 t.u.$, $esr = 3$). Despite this, the dRDM model with 361 mechanical nodes (system size 21.6 $s.u.$) computed the results 38.2 times faster than the PKN model with the same nodal resolution, whilst the dRDM model with 1089 mechanical nodes (system size 38.4 $s.u.$) solved 177.5 times faster than the PKN approach. Figure 2.4 also illustrates that the resolution the dRDM model can be substantially increased (here shown up to 11.11 $N_{MN}/s.u.^2$ with $hx = 0.3 s.u.$ and $emr = 1$), whilst its computational performance allows such computations for larger RDM systems.

Figure 2.4 compares the computational performance of PKN and dRDM simulations with a mechanical node density of 0.69 $N_{MN}/s.u.^2$ ($hx = 0.6 s.u.$ and $emr = 2$). For the main results simulations presented in this paper, a 4 times higher mechanical node density 2.78 $N_{MN}/s.u.^2$ (dRDM $hx = 0.3 s.u.$ and $emr = 2$) was used with the dRDM model. Compared to these dRDM simulations previous PKN research used simulations with up to 49 times lower node density (0.06 $N_{MN}/s.u.^2$ with $hx = 0.6 s.u.$ and $emr = 7$) [43]. If we com-

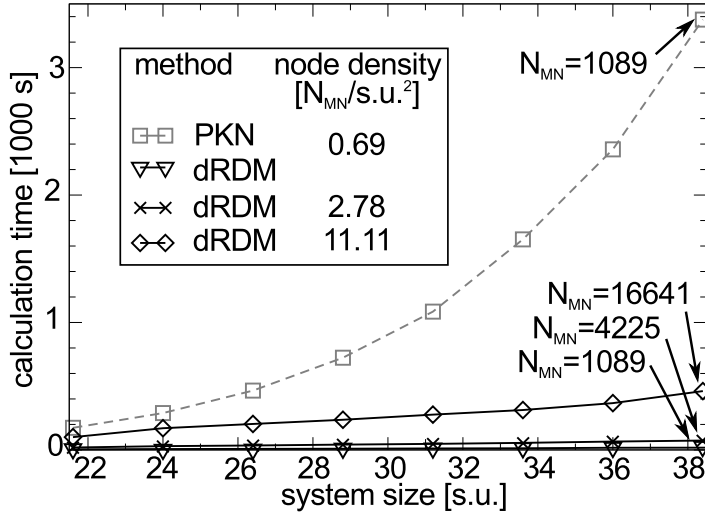


Figure 2.4. Comparison of computational performance of dRDM and PKN. Calculation time is plotted against medium size. A radially spreading wave was initiated at the center of the medium of PKN and dRDM models and simulated for a duration of 10 $t.u.$. Parameters for PKN were as in [43], but $emr = 2$ was used to achieve same mechanical node density as the dRDM with $emr = 2$ and $hx = 0.6 s.u.$ ($0.7 N_{MN}/s.u.^2$). Models with increased mechanical node densities were also analysed using the dRDM approach with $emr = 2$, $hx = 0.3 s.u.$ ($2.8 N_{MN}/s.u.^2$), and $emr = 1$, $hx = 0.3 s.u.$ ($11.1 N_{MN}/s.u.^2$).

pare the computational performance for a typical simulation in this paper (e.g. large system in section “Mechanisms of Pacemaker Drift”, which contains 2601 mechanical nodes with a medium size of 30 $s.u.$), then we estimate that the dRDM approach will be ≈ 3 magnitudes faster than the PKN model (PKN requires 40716.8 s , and dRDM requires 39.3 s for the upper experiment with that number of mechanical nodes). Thus, the application of the PKN model for higher resolutions and larger system sizes is not computationally tractable for studying extended duration model simulations. It is possible to use advanced numerical techniques to improve the numerical performance of finite element methods such as the PKN approach, however that is beyond the scope of this study. The primary aim of this study was to develop a simple and efficient alternative to the PKN approach for the study of basic effects of deformation on wave propagation in excitable media. The dRDM approach provides a computationally tractable method for studying large RDM systems with high temporal and spatial numerical resolutions. The usefulness of the dRDM approach is illustrated in the following results section.

2.3 Results

We have introduced a discrete modeling framework to study the basic properties of RDM systems. We first show that the dRDM approach is able to reproduce some previously reported results on pacemaking activity, which were identified using the PKN model [43]. The RD model in [43] is identical to Eqs.2.1-2.3 in this paper. In addition, no flux boundary conditions for the RD equations and fixed boundaries of the mechanical mesh were used in the present study, as reported in [43]. On the other hand, [43] uses a continuum mechanics formulation that follows the Mooney-Rivlin material relation. The Mooney-Rivlin relation shares similarities with the Seth material relation used in this dRDM model, because both constitutive relations describe isotropic elastic mechanical response. However, the Mooney-Rivlin material relation describes a nonlinear force-displacement relationship for finite deformations. Therefore, we did not seek an exact correspondence of the two approaches, but rather a qualitative agreement as a reflection of the underlying basic mechanisms determining pacemaker dynamics.

2.3.1 Pacemaker Drift

In [43], Panfilov et al. reported on the phenomenon of automatic pacemaking activity in coupled RDM systems. The main objective of this section is to test if the dRDM approach reproduces important mechanisms on self-organized pacemakers that were identified with the continuous PKN modeling framework [43].

To begin, the phenomenon of self-organised pacemaking activity is described. It has been found that a single electrical or mechanical point stimulus can cause the formation of a pacemaker in a RDM medium with non-oscillating RD kinetics. Pacemaking activity occurs because the contraction of the medium that follows a radially propagating wave of excitation subsequently stretches the medium in the neighborhood of the initiation site. This stretch induces a depolarizing stretch activated current I_s (Eq.1.14) that initiates a subsequent excitation wave. The location of this pacemaker may drift over the course of time depending on the position of the initial stimulus [43]. Two main drift directions were identified: to the center of the medium (for larger medium sizes) and to the boundary (for smaller medium sizes) with an intermediate regime involving multiple symmetric attracting points.

Simulations with the dRDM and the PKN models were performed, which showed that all effects found with the PKN model [43] were qualitatively reproduced by the dRDM approach. In particular, the dRDM model reproduced the phenomena of pacemaking activity as well as the dependence of pacemaker drift on the location of the initial stimulus and the size of the medium. Figure 2.5A shows typical drift patterns for a large dRDM model. The pacemaker drifted to the center of the

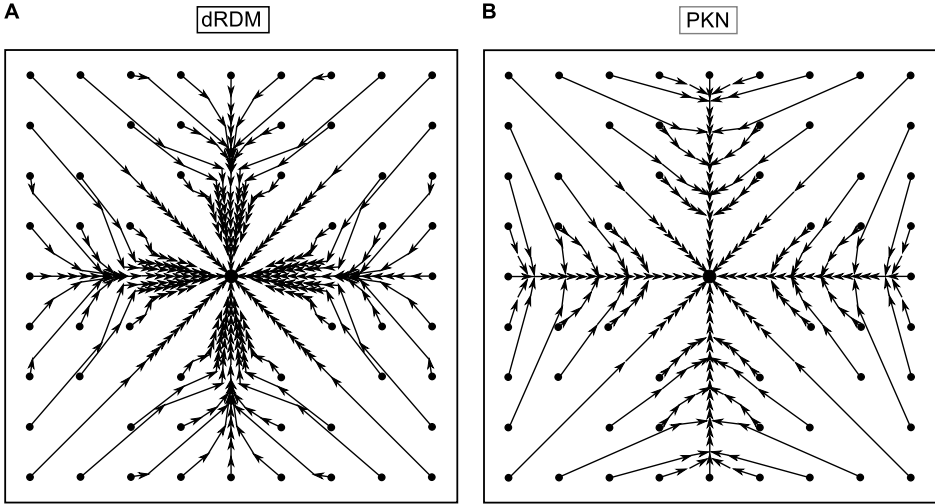


Figure 2.5. Pacemaker drift in large medium (size 38.4 s.u.). Small black dots indicate positions of point stimuli and the arrows indicate drift directions and the estimated positions of sequential action potentials (slow drift is indicated by short arrows). Attractors are indicated as big black dots. **(A)** dRDM model with $G_s = 1.5$ **(B)** PKN model with $emr = 5$, other parameters as in [43].

medium from all initialization locations. Figure 2.5B shows the same experiment performed with the PKN model. Both approaches describe one spatial attractor in the center of the medium.

Figure 2.6A shows the drift patterns for a smaller system size in the dRDM model with peripheral attractors and attractors on the diagonals of the medium. It should be noted that the diagonal attractors were not previously reported in [43]. However, we performed the same experiment using the PKN model (Figure 2.6B) and found that these attractors indeed existed using the continuous PKN approach. Thus all spatial attractors were present in both modeling approaches.

We also studied how the location of the peripheral attractors depended on the medium size. Figure 2.7 demonstrates the distance of the peripheral attractor from the center on a graph similar to that in [43]. Although the elastic properties of PKN and the dRDM model are not identical, the drift patterns showed qualitative agreement. Both modeling approaches demonstrated that there is a shift of peripheral pacemaker attractor locations to the center of the medium as the size of the model is increased. Additionally, this transition occurs at comparable sizes of the medium: 30 – 35 s.u.. Therefore, we conclude that the dRDM model reproduces the same phenomena on pacemaker activity as reported in [43].

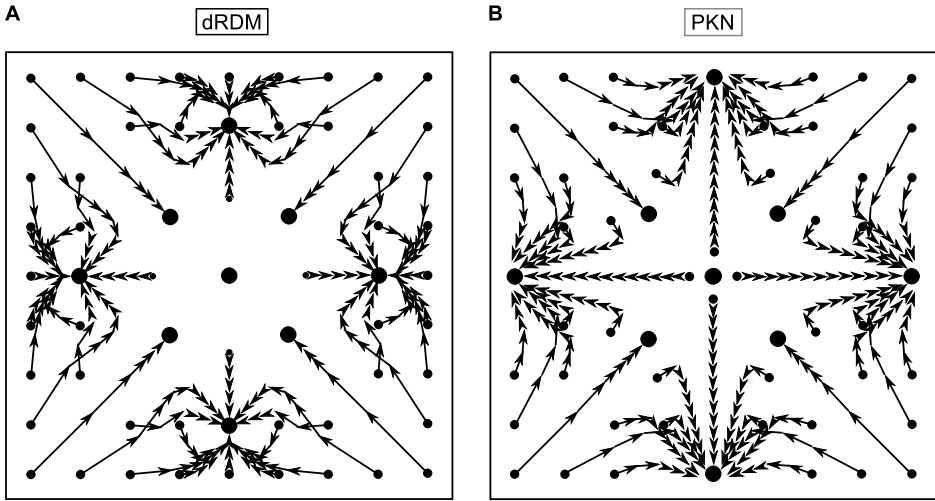


Figure 2.6. Pacemaker drift in smaller medium (size 26.4 s.u.). Notations are as in Figure 2.5. (A) dRDM model with $G_s = 1.5$ (B) PKN model with $emr = 5$, other parameters as in [43].

The increased resolution of the dRDM model (compared to [43]) allows one now to study this system in greater detail. In particular, we shift the focus now onto the following open issues: the effects of change of medium size on the pacemaker period; and the mechanisms underpinning pacemaker drift.

Pacemaker Period

This section is devoted to the cases of pacemaking activity that result in a static pacemaker located at the center of the medium. The aim of this section is to understand the factors that determine the period of the pacemaker and its dependency on the medium size. This investigation commenced with the study of the spatial and temporal transient processes leading to the steady state configuration of a pacemaker with a constant period located at the center of the medium. Figure 2.8 illustrates how the period of a pacemaker of the large system shown in Figure 2.5 evolves during the drift of the pacemaker to the center of the medium. The results of two simulations are shown: for a pacemaker that was initiated at the center of the medium (the red line) and for a pacemaker that was initiated at the boundary of the medium (the black line). In both cases, the pacemakers initially had a long period that rapidly decreased over 3 – 5 cycles. Following this transition phase, the period of the centrally located pacemaker rapidly settled to the value of 11.2 $t.u.$ For the peripherally located pacemaker, its period rapidly decreased during the transition phase to 11.9 $t.u.$ and then the period slowly de-

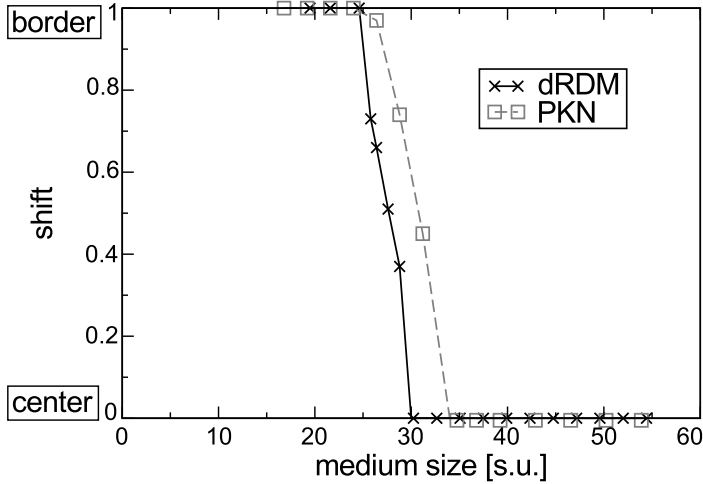


Figure 2.7. Spatial location of the attractor. Relative shift (location of the peripheral attractors as a proportion of the distance from the center to the boundary of the medium) against medium size, where 0 corresponds to the attractor located at the center of the medium, and 1 to the attractor located at the border of the medium. Computations with the dRDM model (black symbols, continuous black lines) were performed using $thr = 2e - 5 f.u.$, $G_s = 1.5$, $E_s = 1$, and $a = 0.05$. The results from the PKN model (red squares, dotted red line) are from [43].

creased further during the drift process. By the time the pacemaker had reached the center of the medium, its period had approached the same value of $11.2 t.u.$. Therefore, the drift of a pacemaker to the center can be described as drift to a region of shorter period.

The results on the study of how the medium size affects the equilibrium period of a stationary pacemaker located in the center of the medium are shown in Figure 2.9A (upper panel). Biphasic behavior was observed. For system sizes larger than $40 s.u.$, the equilibrium period decreased with a decrease in the medium size. On the other hand, for system sizes smaller than $40 s.u.$, the steady-state period increased with a decrease in the medium size. This biphasic behavior is explained in the following. The first regime is the result of an increase in the maximal stretch of the medium. Figure 2.9A (lower panel) shows that the maximal stretch monotonically increased with a decreasing medium size. This observation was qualitatively reported in a previous study using the continuous PKN description [43]. The larger stretch resulted in a larger stretch-activated current I_s , which in turn resulted in a shorter period. The second regime occurred due to a different mechanism. The decrease in medium size also resulted in a decrease of the size of the pacemaker. Figure 2.9A (middle panel) shows the monotonic increase of the curvature of a new forming pulse of a pacemaker with decreasing

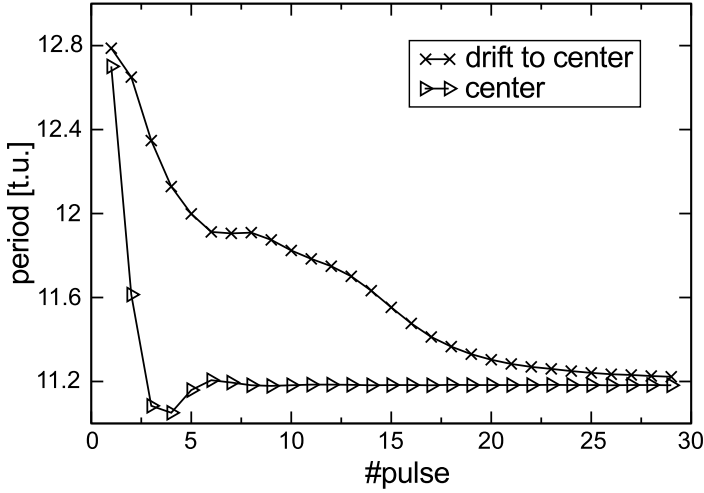


Figure 2.8. Spatio-temporal study of pacemaker period. Pacemaker period for a pacemaker drifting from the boundary of the medium (initiated 18 *s.u.* from the center for the medium size of 38.4 *s.u.*) to the center, in comparison to the period of a pacemaker that was initiated at the center.

medium size. This resulted in an increasing influence of the curvature on wave propagation.

Curvature effects are well known in the theory of excitable media [81] and can be explained using the following formal consideration. If a polar coordinate system (r, ϕ) is used to describe the dynamics of a radially expanding wave front, then the expression for the Laplacian will be given by:

$$\Delta u = \frac{\partial^2 u}{\partial r^2} + \frac{1}{r} \frac{\partial u}{\partial r} = I_{diff}.$$

For an expanding wave front $\frac{\partial u}{\partial r} < 0$, and thus the curvature related term $\frac{1}{r} \frac{\partial u}{\partial r}$ results in a negative diffusive current. This negative diffusive current reduces the velocity of wave propagation and for higher curvature results in the critical curvature phenomenon, i.e. the inability of the wave front to propagate, if its curvature exceeds a critical value. However, for the wave back $\frac{\partial u}{\partial r} > 0$, which results in a positive diffusive current that tends to prolong the action potential. Both of these effects are important to understand the second branch of Figure 2.9A (upper panel). Indeed, comparing the shapes of action potentials for medium sizes 27.6 *s.u.* and 40.8 *s.u.* as shown in Figure 2.9B (black lines), one sees that the upstroke of the action potential was slightly slower in the smaller medium compared to the larger medium (due to negative curvature related current). The recovery process in the smaller medium was also slower (due to the curvature

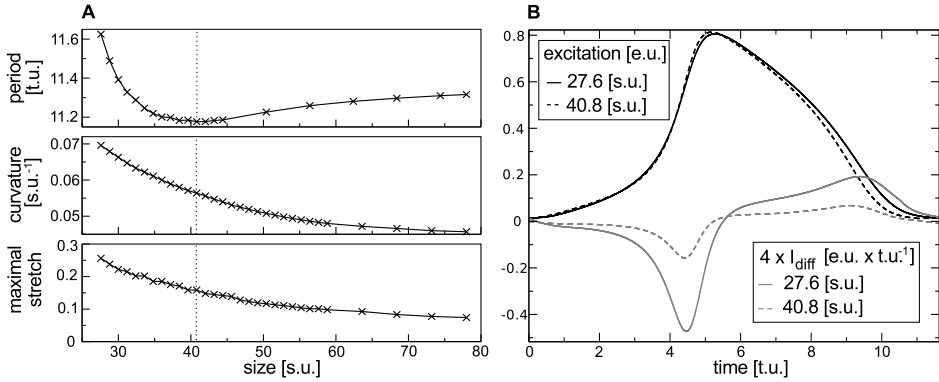


Figure 2.9. Pacemaker period. (A) The “stretch regime” and the “curvature regime” of the pacemaker period (separated by a dotted line in each panel). (Upper panel) Pacemaker period vs medium size. (Middle panel) Curvature of a new forming pulse vs medium size. (Lower panel) Maximal stretch (scaled using $10 \times (\sqrt{A} - 1)$) vs. medium size. (B) Excitation variable u and diffusive current (scaled by $4 \times I_{diff}$) for the center point for one pulse of a pacemaker in a system of size 27.6 $s.u.$ and a system of size 40.8 $s.u.$.

effect on the wave back). This is also illustrated in Figure 2.9B via the diffusive current (red lines), which showed a larger amplitude for the smaller medium that in turn slowed down the upstroke and prolonged the action potential duration. This prolongation increased the period of a pacemaker (see Figure 2.9A). When the medium size was decreased below 27.6 $s.u.$, the firing area became smaller than the critical size and the pacemaker activity disappeared. Indeed, for the medium described with the dRDM model (without deformation) the critical curvature found was $\approx 0.33 (s.u.)^{-1}$, which is close to the curvature $0.26 (s.u.)^{-1}$ below which a block of the pacemaking activity was observed. Therefore, one can conclude that there are two regimes of dependency of the period of a pacemaker on medium size: the “stretch regime”, where the decrease of the period for a decreasing medium size is a result of the increase in maximal stretch; and the “curvature regime”, where for a decreasing medium size the period increases and finally the pacemaking activity is blocked due to curvature effects.

Mechanisms of Pacemaker Drift

This section focusses on pacemaker drift. Figure 2.10 demonstrates a representative example of pacemaker drift to the center of an RDM medium. It illustrates the formation of the 26th pulse after initiation of pacemaking activity near the boundary of the medium. The lower panel reveals the distribution of local dilatation in the medium and the upper panel illustrates the time course of the main

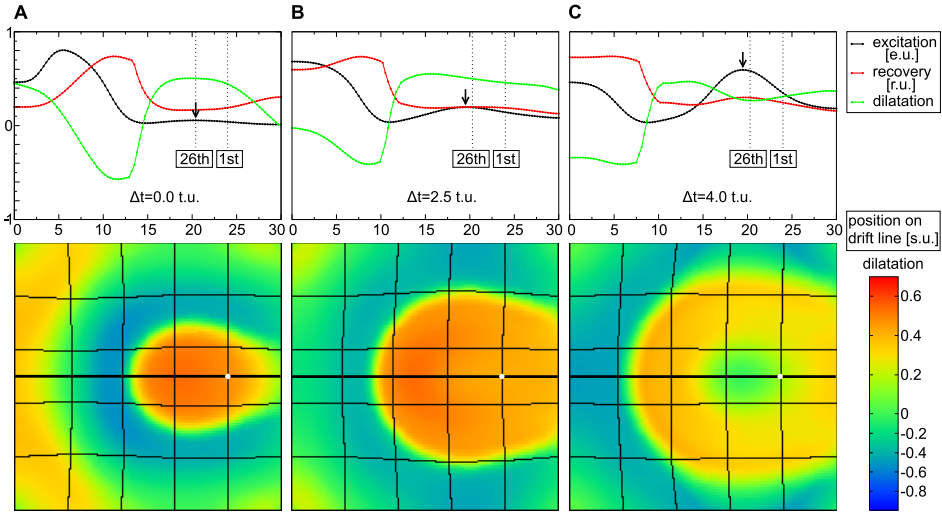


Figure 2.10. Mechanism of pacemaker drift towards center of the medium. (A) emergence of the 26th pulse (at 303.0 $t.u.$). (B) The same pulse after 2.5 $t.u.$ (at 305.5 $t.u.$) and (C) after 4.0 $t.u.$ of its emergence (at 307.0 $t.u.$). The traces in the upper panels illustrate main state variables in the medium along the pacemaker drift lines (thick black horizontal lines in the lower panels): the excitation variable (u) (black), recovery state (scaled using $v/3$) (red), and regional dilatation (scaled using $10 \times (\sqrt{A} - 1)$) (green). The locations of the emergence of the 1st and 26th pulse are marked by vertical dotted lines in the upper panels. The maximum voltage is marked with an arrow. The lower panel indicates the regional dilatation in the medium (scaled using $10 \times (\sqrt{A} - 1)$) by a color spectrum. The point of initial stimulation is indicated by a white dot. Medium size 30.0 $s.u.$.

variables of the dRDM model along the pacemaker drift line, which is indicated as a thick black horizontal line in the lower panel. This line indicates the route of the pacemaker during its drift to the center of the medium. The formation of pulse 26 in the tail of the previous (25th) wave is shown. The following reasoning is based on the stretch distribution in the medium (the green line) generated by this wave. Initially, the stretch is reasonably symmetric around the new forming pulse (see the green line near the arrow in Figure 2.10A). However, a clear gradient is evident with higher stretch directed to the center of the medium at a later stage of pulse formation (see the green line near the arrow in Figure 2.10B). As higher stretch produces a higher stretch activated current I_s , this gradient in stretch leads to a slightly faster depolarization and subsequent excitation closer to the center of the former excitation point (Figure 2.10C). As a result the subsequent pacemaker position is shifted towards the center of the medium and so on until the pacemaker ended up at the center of the medium. From this, one can conclude that the main driving force of the drift in this case is the asymmetry of

the stretch pattern. But why does this asymmetry occur? To study the influence of curvature on the stretch distribution and the pacemaker drift, we compared two cases: a pacemaker initiated by a point stimulus; and a pacemaker initiated by a line electrode. Figure 2.11 shows the stretch distribution and main variables along the drift line immediately prior to the first pacemaker pulse following the stimulus. Again, a gradient in stretch was evident following the point stimulus

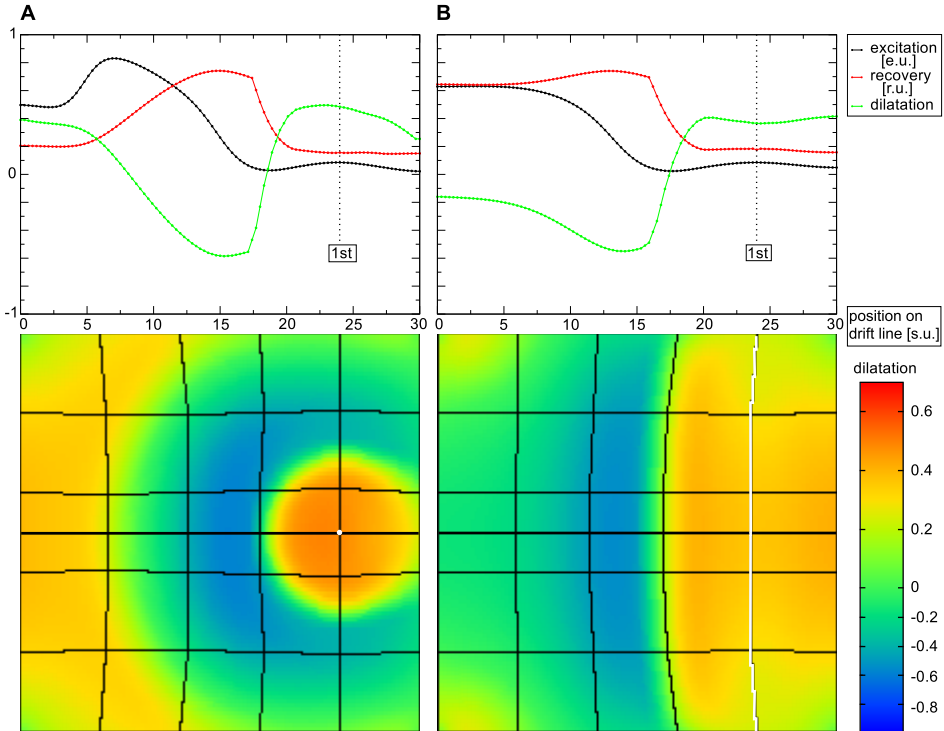


Figure 2.11. Curved wave front causes stretch asymmetry. Pacemaker stimulation with a point stimulus and a line electrode (shown in white in the lower panels). Snapshots taken at (A) 14.3 $t.u.$, and (B) 11.1 $t.u.$. System size and notations are the same as in Figure 2.10.

(Figure 2.11A). However, this asymmetry was not present for the line stimulus (Figure 2.11B). This indicates, that indeed the curvature of the wavefront causes the spatial asymmetry in stretch. Yet, we could not further study a “line-shaped” pacemaker, because after a transient process the initial line-excitation pattern fused to an excitation pattern similar to that following the point stimulus.

To show that the stretch activated current I_s is not important for the formation of the stretch gradient we did similar simulations in the absence of I_s . Figure 2.12A shows the stretch-contraction pattern in this situation. A formation of a gradient

in stretch in the vicinity of the previous pacemaker position (around the vertical dotted line in Figure 2.12A), without stretch activated current is shown. Since

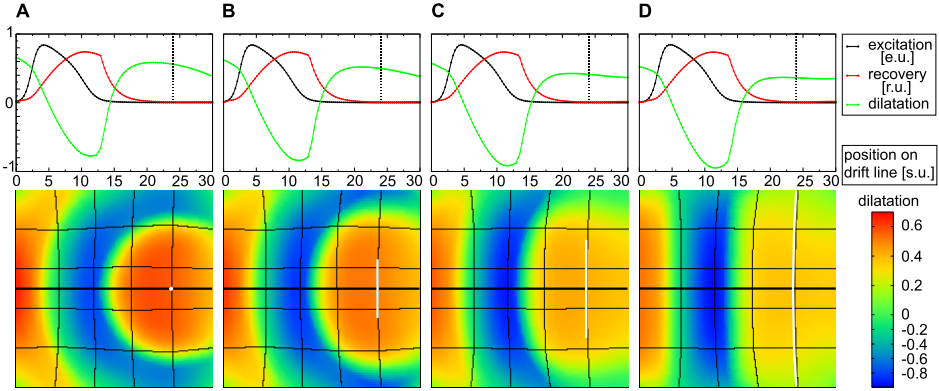


Figure 2.12. Stretch gradient as function of wave shape. Waves of different curvature generated by electrodes of different shape (shown in white in the lower panels). Snapshots are taken at **(A)** 17.4 $t.u.$, **(B)** 13.7 $t.u.$, **(C)** 13.3 $t.u.$, and **(D)** 13.1 $t.u.$ The stretch activated current I_s (Eq.(1.14)) was disabled for these computations. System size and notations are the same as in Figure 2.10.

stretch is the elastic response to a spatial contraction pattern, we studied of how the shape of the wave front affects the formation of this gradient in stretch. For this study, the wave was initiated by linear electrodes with increasing size, which resulted in the generation of waves with progressively decreased curvature (Figure 2.12, lower panel). A decrease in curvature decreased the stretch asymmetry until it disappeared for a plane wave stimulus (Figure 2.12D). Therefore, we conclude that a gradient in stretch in the studied system is formed by the curvature of the wave. Qualitatively this can be understood from the fact that plane wave excitation (contraction) produces stretch mainly in one direction, however, circular contraction “pulls” a point behind a wave front into many directions producing higher maximal stretch than a plane front. This effect is different for points at different distances from the front, which generates a gradient in stretch. A detailed study of the effects of front shape on deformation patterns will be presented as a separate study. The conclusions that can be drawn here is that the drift of a pacemaker to the center in the mechanical setup introduced in [43] is driven by the asymmetry of the stretch pattern, which in turn, is strongly influenced by the shape of the wave front.

As demonstrated in Figure 2.7, pacemaker drift was directed towards the boundaries of smaller models. There is yet to be a comprehensive understanding of the mechanisms of this drift, but we believe it is related to the “curvature regime” of the period variation as described above. In smaller media the influence of the diffusive current is increased, and it starts affecting the duration of the action

potential by inducing a gradient in action potential duration towards the center of the medium. However, to date the authors were unable, to quantify the effects of the diffusive current in relation to drift direction and discriminate them from other observed factors, such as elliptical shape of the firing region, etc. This may serve as a good starting point for follow-up studies.

2.4 Discussion

In this paper, we introduce a discrete modeling framework for the study of reaction-diffusion-mechanics systems. The model is based on the coupling of a mass-lattice model with reaction-diffusion equations. Mass-lattice models are widely used in various areas of computational mechanics research and application [54, 58]. There are several advantages of the dRDM approach presented in this paper. Firstly, its implementation does not require finite element methods, but can be achieved using explicit methods, which allow for a more frequent update rate and higher spatial resolution of the mechanical mesh configuration. Furthermore, the explicit numerical scheme used in this paper to solve the mechanics equations is very effective in studying large systems as the computational speed scales approximately linearly with the number of mass points in the system. The main disadvantage of this approach is that it can not easily be connected to known continuous material properties. However, this does not pose a problem, as we have shown in this paper, that an isotropic Seth material can be used to study basic mechanisms of RDM systems. For more complex materials, it may be necessary to apply homogenization techniques to formulate their constitutive relations. An example of the application of homogenization techniques to derive constitutive relations for a mass-lattice model and its relation to cardiac tissue is given in [59]. It is important to note the possibility to relate discrete mechanics modeling to continuum mechanics by obtaining forces in the mass-lattice model directly from the corresponding constitutive relations [58].

Discrete mechanics modeling and thus our dRDM model is not limited to isotropic material relations. Bourguignon et al. showed that discrete mechanics modeling can be applied to describe elastic properties of anisotropic materials [56]. This approach was further extended to model cardiac elasticity [57, 58]. The extension of the dRDM approach by coupling a RD-model for cardiac excitation to these existing discrete models for anisotropic and hyperelastic cardiac tissue [57, 58] is an interesting approach for the engineering of efficient whole heart models. Furthermore the discrete mechanics description of the dRDM model allows an extension to describe discontinuous deformations [52, 53].

Although cardiac tissue is anisotropic, our isotropic approach can still be applied to several experimental systems. For example the dRDM model is suitable to describe electromechanical processes in cultures of cardiac cells. The tissues pro-

duced in these experiments do not show electrical or mechanical anisotropy.

In this work, a discrete mechanical model was coupled with a low-dimensional RD model for cardiac excitation to study the effect of mechano-electrical feedback on cardiac excitation. The phenomenon of pacemaking activity due to stretch activated current was studied, which was previously done using a continuous RDM approach [43]. The dRDM approach not only reproduced all phenomena found with the continuous system, but also allowed us to study them with higher numerical resolution. As a consequence, new properties of pacemakers were identified, such as dependency of the pacemaker period on its location and on medium size. Furthermore, factors that affect the drift of a pacemaker were also identified.

In the continuous modeling approach, the Laplacian in Eq.2.1 was formulated as a function of the metric tensor to model the influence of deformation on diffusibility [43]. In this paper, however, it is assumed that the main resistance between cardiac cells is not affected during deformation. In the end, this issue was found to be non-essential for the particular problem studied here. Several test simulations using the continuous approach used in [43] were performed and no effects of the different representation of the Laplacian on pacemaker dynamics were found.

2.5 Acknowledgements

The authors are grateful to Dr. Rikkert H. Keldermann for valuable discussions on modeling setup and to Dr. Verônica Grieneisen, Dr. Stan Marée, Dr. Kirsten H. Ten Tusscher, Dr. Daniel S. Lambrecht and Ivan Kazbanov for discussions and useful comments on the manuscript. The authors furthermore thank Lisa Rebert for help with language editing of the manuscript and Jan Kees van Amerongen for excellent technical support.

Chapter 3

New Mechanism of Spiral Wave Initiation in a Reaction-Diffusion-Mechanics System

LOUIS D. WEISE¹ AND ALEXANDER V. PANFILOV² (2011)

¹Theoretical Biology & Bioinformatics, Utrecht University, Utrecht, The Netherlands

²Department of Physics and Astronomy, Ghent University, Ghent, Belgium

PLOS One, **6(11)**: e27264

Abstract

Spiral wave initiation in the heart muscle is a mechanism for the onset of dangerous cardiac arrhythmias. A standard protocol for spiral wave initiation is the application of a stimulus in the refractory tail of a propagating excitation wave, a region that we call the “classical vulnerable zone”. Previous studies of vulnerability to spiral wave initiation did not take the influence of deformation into account, which has been shown to have a substantial effect on the excitation process of cardiomyocytes via the mechano-electrical feedback phenomenon. In this work we study the effect of deformation on the vulnerability of excitable media in a discrete reaction-diffusion-mechanics (dRDM) model. The dRDM framework combines FitzHugh-Nagumo-type equations for cardiac excitation with a discrete mechanical model describing a finite-elastic isotropic material (Seth material) to model cardiac excitation-contraction coupling and stretch activated depolarizing current. We show that deformation alters the “classical”, and forms a new vulnerable zone at longer coupling intervals. This new vulnerable zone results in a new mechanism for spiral wave initiation, where unidirectional conduction block and rotation directions of the consequently initiated spiral waves are opposite compared to the mechanism of spiral wave initiation due to the “classical vulnerable zone”. We show that this new mechanism for spiral wave initiation can naturally occur in situations that involve wave fronts with curvature and discuss its relation to supernormal excitability of cardiac tissue. The concept of mechanically induced vulnerability may lead to a better understanding about the onset of dangerous heart arrhythmias via mechano-electrical feedback.

3.1 Introduction

Reaction-diffusion (RD) equations describe a wide range of phenomena in biological, physical and chemical systems, such as rotating spiral waves. Examples are spiral waves in the Belousov-Zhabotinsky (BZ) reactions [12, 72], and in the catalyzed oxidation of carbon monoxide on platinum surfaces [13]. Spiral waves of cAMP lead the morphogenesis of the *Dictyostelium discoideum* amoebae [15, 73] and occur in retinal and cortical nerve tissue [14], where they underpin neurological diseases, such as epilepsy and migraine. One of the most studied systems is the heart, where spiral wave excitation patterns are a main cause for life-threatening cardiac arrhythmias [3, 72].

In many cases the phenomena described by the RD equations are closely coupled with mechanical processes, such as cell motion in Dd-morphogenesis [73] or the swelling of a gel caused by BZ reactions [74], that cannot be described by the RD equations alone. For the heart, the coupling mechanism between the excitation and the deformation processes works in both directions. The primary physiological function of the heart, its rhythmical pumping, is governed by electrical waves of excitation [17]. The contraction of the heart, however, in turn directly affects the excitation process of the cardiomyocytes. This phenomenon “mechano-electrical-feedback” has been studied in cardiac electrophysiology for over a century, and has been shown to have both positive and negative consequences on the heart rhythm [9]. Recently, a modeling approach has been proposed, that can account for basic effects of the coupled electrical and mechanical cardiac activity, the reaction-diffusion mechanics (RDM) modeling framework [7]. The RDM approach combines the RD equations to describe wave propagation with the equations of continuum mechanics to model the deformation of the medium. Using this RDM framework, important phenomena were identified, such as self-organized pacemakers [43] and the drift and breakup of rotating spiral waves [60].

In this paper we show results of a RDM study on an initial step of the onset of cardiac arrhythmias, the initiation of spiral waves. For this research we applied a recently introduced discrete RDM model [82] (dRDM), which couples FitzHugh-Nagumo-type RD equations for cardiac excitation [28] with a discrete mechanics model describing a finite elastic, isotropic material (Seth material). The dRDM framework describes cardiac excitation-contraction coupling and immediate mechano-electrical-feedback due to a depolarizing stretch activated current.

Vulnerability of an excitable medium is the phenomenon of spiral wave initiation by a local stimulus whose responding wave is unidirectionally blocked by an asymmetric distribution in excitability [71]. We denote the vulnerable zone at the refractory tail of an excitation wave in this paper as the “classical vulnerable

zone”. We studied vulnerability in the dRDM model with the “pinwheel experiment”, a standard stimulation protocol for the initiation of spiral waves. In this protocol a stimulus is applied in the back of a previously initiated excitation wave, with a certain coupling interval between the applied stimuli [2, 83].

Our main finding is that deformation induces a new type of vulnerability in the dRDM system which results in a new mechanism of spiral wave initiation. In this mechanism an unidirectional block occurs in the opposite direction compared to a block caused in the “classical vulnerable zone”. This mechanically caused unidirectional block results in pairs of spiral waves rotating in the opposite direction to those resulting from a wave block in the “classical vulnerable zone”. We study the mechanism of this phenomenon and its dependence on changes in the stimulation protocol. Furthermore we provide examples when this new type of spiral wave initiation naturally occurs due to stretch caused by wave fronts with curvature. Finally we discuss the importance of our findings for the phenomena of supernormal excitability of cardiac tissue and the onset of cardiac arrhythmias.

3.2 Methods

For this study we used the dRDM model [82], which has been shown to enable efficient computations with higher spatial and temporal numerical resolution compared to the continuous RDM description used in [43]. In [82] a detailed description of the dRDM model setup and numerical methods is given. Table 3.1 provides an overview of all parameters of the dRDM model and their numerical values used in this publication and shows alterations to parameters used in [82]. The dRDM model consists of a two-variable FitzHugh-Nagumo-type RD model for cardiac excitation [28], coupled with mechanics equations describing a finite-elastic, isotropic material [82]

$$\frac{\partial u}{\partial t} = \nabla^2 u - ku(u - a)(u - 1) - uv - I_s, \quad (3.1)$$

$$\frac{\partial v}{\partial t} = \epsilon(u)(ku - v), \quad (3.2)$$

$$\frac{\partial T_a}{\partial t} = \epsilon(u)(k_T u - T_a), \quad (3.3)$$

$$\mathbf{F}_{12} = \left(\frac{T_a(1) + T_a(2)}{2} \right) \frac{\mathbf{1}_{12}}{\|\mathbf{1}_{12}\|}, \quad (3.4)$$

$$\mathbf{f}_{1a} = \left[c \left(\frac{\|\mathbf{1}_{12}\| - r_0}{r_0} \right) - d \frac{(\dot{\mathbf{1}}_{12} \cdot \mathbf{1}_{12})}{\|\mathbf{1}_{12}\|} \right] \frac{\mathbf{1}_{12}}{\|\mathbf{1}_{12}\|} + \mathbf{F}_{12}, \quad (3.5)$$

$$\mathbf{f}_{1p} = \frac{1}{2} \left[c \left(\frac{\|\mathbf{1}_{13}\| - \sqrt{2}r_0}{\sqrt{2}r_0} \right) - d \frac{(\dot{\mathbf{1}}_{13} \cdot \mathbf{1}_{13})}{\|\mathbf{1}_{13}\|} \right] \frac{\mathbf{1}_{13}}{\|\mathbf{1}_{13}\|}, \quad (3.6)$$

$$\sum_{\alpha=1}^N \mathbf{f}_{i\alpha} = m\ddot{\mathbf{x}}_i = 0, \quad (3.7)$$

$$I_s = G_s(\sqrt{A} - 1)(u - E_s), \quad (3.8)$$

Table 3.1. Overview of dRDM parameters.

Category	Parameter	Numeric value
Electrophysiology	a	0.08; (0.05)
	k	8
Mechanics	k_T	1.5
	c	1, varied in inhomogeneities; (1)
	d	$30 \times c$
	m	1
Electromechanical feedback	G_s	2.0 and 2.6; (1.5)
	E_s	1.0
Mesh coupling	emr	2
	esr	1
	thr	2×10^{-5}
Integration	$m\tau$	0.01
	Δt	0.001
	$\Delta x = \Delta y$	0.3

Parameters for the dRDM model used in this paper, and after a semicolon “;” (in parentheses) numerical values are shown that were used in the previous publication [82] if the numerical value changed in the present paper. Parameter emr is the ratio of mass points to finite difference points, esr is the update ratio of the RD system to the update of the mesh configuration.

where $\epsilon(u)$ is a step function setting the time scale of the recovery and contraction process: $\epsilon(u) = 1$ for $u < 0.05$, and $\epsilon(u) = 0.1$ for $u \geq 0.05$. For undeformed tissue, Eqs. (3.1), (3.2) with transmembrane potential u (in dimensionless excitation units [e.u.]) and conductance of slow repolarizing current v (in dimensionless recovery units [r.u.]), describe non-oscillatory cardiac tissue, which is able to provide stable wave propagation for the parameters $a = 0.08$ (activation threshold) and $k = 8$ (magnitude of transmembrane current) used in this paper. The medium of the dRDM model is described by a square lattice, where mass points are connected to $N = 8$ (if not at the boundary) direct neighboring mass points with springs. Each such mass point is connected to its 4 diagonal neighbors with “passive springs” (describing passive elastic properties only), and to its 2 vertical and 2 horizontal neighbors with “active springs” (springs that additionally mediate active forces). Eqs. (3.3), (3.4) describe the excitation-contraction coupling for two neighboring mass points 1 and 2 that are connected by an active spring, where T_a modulates the active contraction force via Eq.(3.4), and the parameter k_T ($k_T = 1.5$ in this paper) controls the amplitude of the contraction twitch. The Eqs. (3.5), (3.6) describe the forces $\mathbf{f}_{1a} = -\mathbf{f}_{2a}$ mediated through an active spring to mass points 1 and 2, and the forces $\mathbf{f}_{1p} = -\mathbf{f}_{3p}$ mediated through a passive spring to mass points 1 and 3, respectively. In Eqs.(3.5), (3.6) the spring vectors are given by the mass point’s positions as $\mathbf{l}_{12} = \mathbf{x}_2 - \mathbf{x}_1$ and $\mathbf{l}_{13} = \mathbf{x}_3 - \mathbf{x}_1$,

r_0 is the resting length of an active spring and $\sqrt{2}r_0$ the resting length of a passive spring, $\dot{\mathbf{l}}_{12} = \mathbf{v}_2 - \mathbf{v}_1$ and $\dot{\mathbf{l}}_{13} = \mathbf{v}_3 - \mathbf{v}_1$ are the time derivatives of the respective spring vectors \mathbf{l}_{12} and \mathbf{l}_{13} , and c and d are the stiffness and damping constants ($c = 1$ unless stated otherwise, and $d = 30 \times c$). The forces \mathbf{f}_{1a} , \mathbf{f}_{1p} are functions of the mass point's positions $\mathbf{x}_1, \mathbf{x}_2, \mathbf{x}_3$, velocities $\mathbf{v}_1, \mathbf{v}_2, \mathbf{v}_3$ and $T_a(1), T_a(2)$ that form the active force distribution through Eqs.(3.3), (3.4). Following previous RDM studies to study cardiac electromechanics [7, 43, 60, 82] elastostatics was assumed in this paper. By solving Eq.(3.7), with the mass m of a mass point set to 1, the elastostatic configuration of the lattice for every force distribution defined by the RD state is found. The deformation of the tissue feeds back on the excitation process. Following previous studies [43, 60, 82], we describe the direct influence of deformation on the excitation state of the medium as depolarizing stretch-activated currents [9], that are activated instantaneously with mechanical dilatation, and describe a linear current-voltage relationship [61, 62]. Therefore we use Eq.(3.8) in this paper to model mechano-electrical feedback through stretch activated channels. In Eq.(3.8) the parameters G_s and E_s are the maximal conductance and reversal potential of the stretch activated channels ($E_s = 1$ in this paper), the variable A is the normalized surface area (relative to the undeformed reference surface area) of a square, formed by 4 direct neighboring mass points, connected with active springs. Stretch activated current I_s is active only if $A > 1$ (stretch). The value of G_s is a main parameter of the effect of I_s . In our simulations we varied G_s in a range of 2.0 – 2.6, where we also can get pacemaking activity [43, 82] in the medium.

3.2.1 Numerical Methods

The coupled dRDM model was solved with a hybrid approach, the explicit Euler method to solve the RD system, and the Verlet integration scheme [79] to solve the mechanical model. After each Euler computation of the RD system describing a new force distribution in the medium, the mechanical equations were solved with a Verlet integration time step $m\tau = 0.01$ until the sum of forces for each mass point was smaller than the threshold $thr = 2 \times 10^{-5}$ (dimensionless force units [f.u.]). Euler computations were performed on a quadratic deforming grid of up to 202×202 finite difference points using no-flux boundary conditions. For all simulations, an Euler integration time step of $\Delta t = 0.001$ (dimensionless time units [t.u.]) and a space integration step of $\Delta x = \Delta y = 0.3$ (dimensionless space units [s.u.]) were used. According to the explicit Euler method the diffusion term in Eq.(3.1) for a electrical mesh point at position (x, y) is computed as

$$\nabla^2 u(x, y) = \frac{[u(x + \Delta x, y) + u(x - \Delta x, y)] + (u(x, y + \Delta x) + u(x, y - \Delta x) - 4u(x, y))}{\Delta x^2},$$

and the excitation state of an electrical mesh point for a next time step $t + \Delta t$ is computed as

$$u(t + \Delta t) = u(t) + \frac{\partial u(t)}{\partial t} \times \Delta t.$$

The position of a mass point i during the iterative solution of Eq.(3.7) is computed by a Verlet step with

$$\mathbf{x}_i(\tau + m\tau) = 2\mathbf{x}_i(\tau) - \mathbf{x}_i(\tau - m\tau) + \ddot{\mathbf{x}}_i(\tau) \times (m\tau)^2.$$

The boundaries of the deformable medium were fixed in space modeling isometric contraction to mimic isovolumic phases in the cardiac cycle, an assumption that has been made also in previous electromechanical studies [43, 60, 82]. The parameter k_T together with the stiffness constant c control local deformations of the contraction process. These parameters were chosen to give rise to relative local deformations in the medium of up to 15% (similar to contracting cardiac cells). The elastic properties of this model can be described by the Seth material constitutive relation [82].

3.2.2 Pinwheel Experiment

Figure 3.1 illustrates the setup of the pinwheel experiment and demonstrates the vulnerability of an excitable medium in the dRDM model without deformation (Eqs.(3.1),(3.2)). In a pinwheel experiment a 'secondary stimulus' (S2) is applied in the back of a previously initiated "S1 wave" (see Figure 3.1A). The wave initiated by the S2 stimulation can be blocked by the refractory tail (lower panel of Figure 3.1) towards the propagation direction of the S1 wave and can only propagate in other directions (see schematic successive front positions in upper panel of Figure 3.1A). As a result a pair of counter rotating spiral waves occurs. The upper panel of Figure 3.1B illustrates the vulnerable zone of the non-deforming excitable medium. Blue dots symbolize S2 stimuli for which spiral waves were initiated. The black crosses mark the lowest stimulation strengths which result in no conduction blocks and thus to connected wave fronts. Stimulations with positions and strengths under the lower bound of these regimes resulted in no wave initiation (the threshold of excitation). This unidirectional block is caused by a gradient in excitability due to the recovery tail of the S1 wave [69]. The lower panel of Figure 3.1B shows an inset of the voltage and the recovery variable in the tail of the S1 wave. We see a monotonic decrease of the recovery variable v which causes the monotonic decrease of excitability (compare upper panel of Figure 3.1B) in the tail of the wave, which explains the block of the S2 wave in the forward direction. We refer to the vulnerable zone, which is formed by the recovery tail of a wave, as the "classical vulnerable zone" in this work. The "classical vulnerable zone" has been shown previously to be an inherent property of excitable media [71].

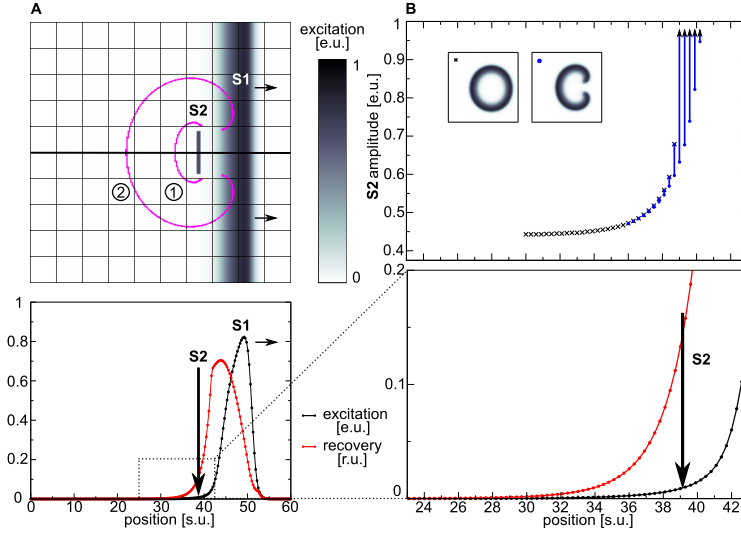


Figure 3.1. Pinwheel experiment. (A) Spiral wave initiation by S2 stimulus in “classical vulnerable zone”. Upper panel shows 2D medium. The resulting wave front is indicated with magenta contours for (1) 4 $t.u.$ and (2) 12 $t.u.$ immediately prior the S2 stimulus (indicated by vertical arrow). Lower panel shows state variables excitability u (black) and recovery v (scaled using $v/3$) (red) on the cross section indicated by a thick black line in the upper panel. (B) “Classical vulnerable zone”. Lower panel shows state variables in the refractory tail of the S1 wave (inset from figure A indicated by dotted lines). Upper panel shows regimes of responses to the S2 stimulation as a function of position and amplitude. Lowest S2 amplitudes that result in a connected wave front are indicated as black crosses, stimulations that result in spiral wave dynamics are indicated blue. Stimulations with lower amplitudes (under curve) result in no wave propagation. A $9.6 \times 0.6 s.u.^2$ stimulus was applied for 0.001 $t.u.$ with different amplitudes. System size was 60 $s.u.$. S1 stimulus was applied at 0.0 $t.u.$, and S2 stimulus was applied at 35.7 $t.u.$

3.3 Results

3.3.1 “Classical Vulnerable Zone” in Deforming dRDM System

Repeating the pinwheel experiments for the deforming dRDM system (Eqs.(3.1)-(3.8)) we find the “classical vulnerable zone” slightly altered. The top panel of Figure 3.3B illustrates the vulnerable zone for the deforming dRDM system. Following the notation from Figure 3.1B the stimulations at positions and amplitudes that result in classical spiral wave initiation are indicated in blue, and the lowest stimulation strengths that cause connected wave fronts are indicated as black

crosses. A comparison of the top panels of Figure 3.3B and Figure 3.1B shows that the “classical vulnerable zone” (regime *I*) is also present in the deforming system. The “classical vulnerable zone” in the deformed case shows a steeper excitability gradient compared to the undeformed system. As a result the threshold of excitation for the undeformed system is higher in the “classical vulnerable zone” compared to the deforming system. For instance at position 39.9 *s.u.* a minimal S2 amplitude of 0.70 *e.u.* is required in the deformed case, whereas for the undeformed case a minimal S2 amplitude of 0.82 *e.u.* is required. This can be explained by the depolarizing stretch activated current I_s , that is present for positions smaller than ≈ 39.7 *s.u.*, where local stretch develops (lower panel of Figure 3.3B) and leads to an increase in u and thus to a decreased threshold of excitation.

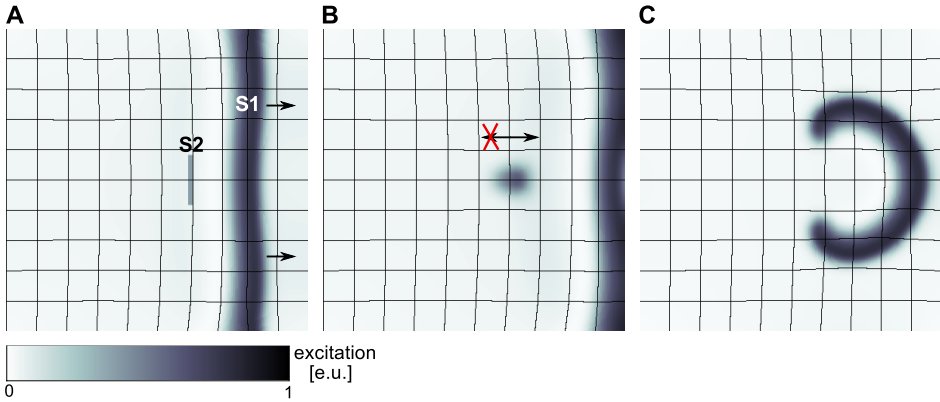


Figure 3.2. New regime of spiral wave initiation. (A) S2 stimulus is applied in the mechanically induced vulnerable zone of S1 wave (arrows indicate propagation direction). (B) Unidirectional block of S2 wave retrogradely to propagation direction of S1 wave (indicated by arrows), $\Delta t = 6.2$ *t.u.* after S2 stimulus. (C) Figure eight reentry pattern evolved from wave block of S2 wave response (see B), $\Delta t = 20.2$ *t.u.* after S2 stimulus. For the S2 stimulus a 9.6 *s.u.* long and 0.6 *s.u.* thick electrode of 0.385 *e.u.* was applied at position 35.4 *s.u.* for 0.001 *t.u.*. System size was 60 *s.u.*. S1 stimulus to initiate the S1 wave was applied at 0.0 *t.u.*, S2 stimulus was applied at 33.5 *t.u.*. System and simulation protocol as in Figure 3.3.

3.3.2 New Mechanism of Spiral Wave Initiation

In addition to the “classical vulnerable zone” we find a new regime of spiral wave initiation for the deformed case. For stimulations at positions ≈ 28.0 to 37.0 *s.u.*, depicted as orange dots in the upper panel of Figure 3.3B, we see that the propagation of the S2 wave is blocked oppositely to the propagation direction

of the S1 wave. As a result a pair of counter rotating spiral waves is initiated (upper panel Figure 3.3A) (regime *II*) with rotation directions opposite to spirals initiated by the classical mechanism (upper panel Figure 3.1A) (regime *I*). This process of mechanically caused conduction block and spiral wave initiation is illustrated in Figure 3.2. We see, an S2 stimulation (Figure 3.2A) that results in a wave that can propagate away from the S1 wave but fails to propagate towards it (Figure 3.2B), forming a pair of counter rotating spirals (Figure 3.2C).

The mechanism of this new regime of spiral wave initiation can be understood from Figure 3.3B. We see a non-monotonous dependence of the threshold for wave initiation by an S2 stimulus (lower boundary of curve in top panel of Figure 3.3B) on the distance from the S1 wave. The medium is most excitable (lowest threshold) at position 35 *s.u.*, from where the threshold gradually increases with larger distance from the S1 wave to a steady state value. As a result a stimulation around the maximal excitability in the medium may initiate a wave that is able to propagate towards the S1 wave, but is blocked in the opposite direction.

How does deformation cause this new vulnerability? In the lower panel of Figure 3.3B we can see the state variables of the dRDM model in the vulnerable zone. The transmembrane potential u is indicated as a black line, the recovery state as a red line and stretch as a green line. We see that in the back of the S1 wave, where the medium recovers (from 37 – 39 *s.u.*), local stretch develops in the medium. The stretch in the medium causes depolarizing stretch activated current I_s , which leads to an increase of u . In general an increase of u brings the system closer to the threshold value and thus decreases the threshold of the S2 stimulation amplitude, which explains the decrease of the S2 threshold in the “classical vulnerable zone”. However, further behind the back of the S1 wave another process takes place. The increased u causes the recovery state v to increase, which in turn decreases the excitability of the medium. Thus we can state that the threshold minimum and gradient emerges due to the depolarization of the tissue by stretch activated current I_s (Eq.(3.8)). Note, that in general, the decrease of excitability caused by slow depolarisation is a well known phenomenon, called accommodation which has been studied in electrophysiology since 1936 [18, 84]. A previous study [60] also showed that this phenomenon can result in block of waves during spiral wave rotation. Here we show another mechanically induced manifestation of accommodation in RDM systems.

3.3.3 Dependence of the New Mechanism on Stimulation Parameters

We tested how the protocol of stimulation affects the new mechanism of spiral wave initiation. For this, we studied the effect of electrode shape (thickness) and duration of a S2 stimulus, applied in the position of maximal excitability

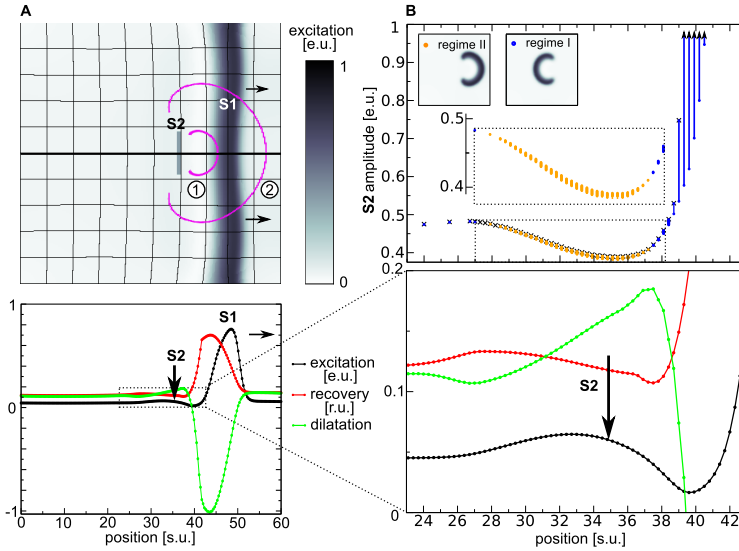


Figure 3.3. Mechanically induced vulnerability. (A) Spiral wave initiation by S2 stimulus in mechanically caused vulnerable zone. Upper panel shows 2D medium. The resulting wave front is indicated with magenta contours for (1) 10 $t.u.$ and (2) 20 $t.u.$ after S2 stimulus was applied. Lower panel shows main variables transmembrane potential u (black), recovery (scaled using $v/3$) (red) and the dilatation (scaled using $10 \times (\sqrt{A} - 1)$) (green) on the cross section indicated by a thick black line in the upper panel, immediately prior the S2 stimulus (indicated by vertical arrow). (B) Mechanically induced vulnerability. Lower panel shows state variables in the refractory tail of the S1 wave (inset from figure A indicated by dotted lines). Upper panel shows regimes of responses to the S2 stimulation as a function of position and amplitude. Smallest S2 amplitudes that result in a connected wave front are indicated as black crosses, stimulations that result in classical spiral wave dynamics (block towards S1) are indicated blue (regime I). Stimulations that result in the new regime of spiral wave dynamics (block retrogradely to the S1 wave) are indicated as orange points (regime II). Stimulations with lower amplitudes (under curve) result in no wave propagation. Inset magnifies stimulations that result in spiral waves in new vulnerable zone. A $9.6 \times 0.6 s.u.^2$ stimulus was applied for 0.001 $t.u.$ with different amplitudes. System size was 60 $s.u.$ and $G_s = 2.6$. S1 stimulus was applied at 0.0 $t.u.$ and the S2 stimulus was applied at 33.5 $t.u.$.

(35 $s.u.$), on the window of stimulus strengths that initiate spiral waves. We found that the thickness of the stimulated region does not affect the parameter window significantly (Figure 3.4A). However, it turned out that a longer stimulation pulse approximately doubles the parameter window to a maximal window size of 4.2% (Figure 3.4B).

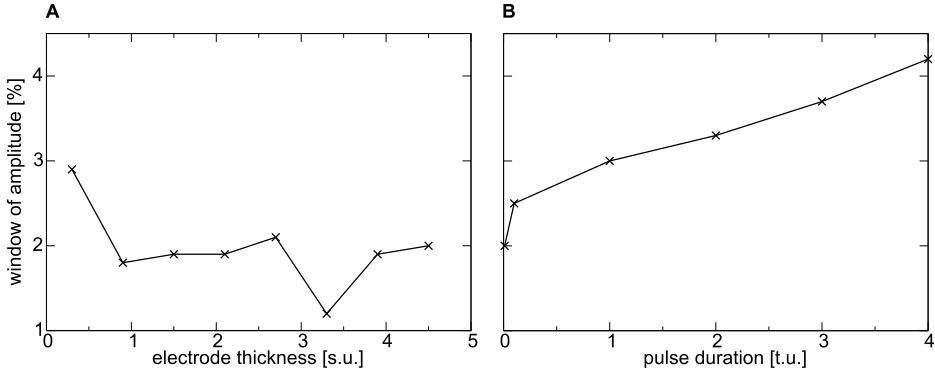


Figure 3.4. Dependence of the new mechanism on stimulation parameters. (A) Window of amplitude against electrode thickness. (B) Window of amplitude against pulse duration. System and stimulation protocol as in Figure 3.3.

3.3.4 Mechanically Initiated Spiral Waves

Although the parameter window of S2 stimulation strengths, where the mechanically induced vulnerable zone leads to spiral wave dynamics, is narrow it may still be an important mechanism, as it is located at the area of maximal excitability in the medium. This is illustrated by the following examples. It has been shown previously [43, 82] that a point stimulus in an electromechanical system can produce pacemaking activity. This is because a radially spreading excitation-contraction wave tends to stretch and thus depolarizes the medium by stretch activated current in the vicinity of the initial point stimulus. This stretch activated current can initiate a new wave. The strength of this stretch activated current depends on the degree of stretch of the medium which itself is affected by many other factors, such as boundary conditions and elastic properties of the material. Furthermore the magnitude in stretch depends on the location of the initial stimulus in the medium: if it is closer to the center the stretch amplitude is maximal, and decreases when the pacemaker position shifts to the boundary of the medium [82]. It turns out that this effect can also initiate spiral waves via the new mechanism reported in this paper. If a point stimulus is applied in the system within the inner region of the medium enclosed by the green region in Figure 3.5F, then sustained pacemaking activity emerges [82]. However, if the initial stimulus is applied in the region outside the green region in Figure 3.5F, then the resulting stretch in the vicinity of the initial stimulation site is not sufficient to stimulate a additional pulse. However, if the initial stimulus is applied in the green area, it leads to a “close to threshold” excitation of the medium and spiral wave generation via the new mechanism. Figures 3.5A-E illustrate this phe-

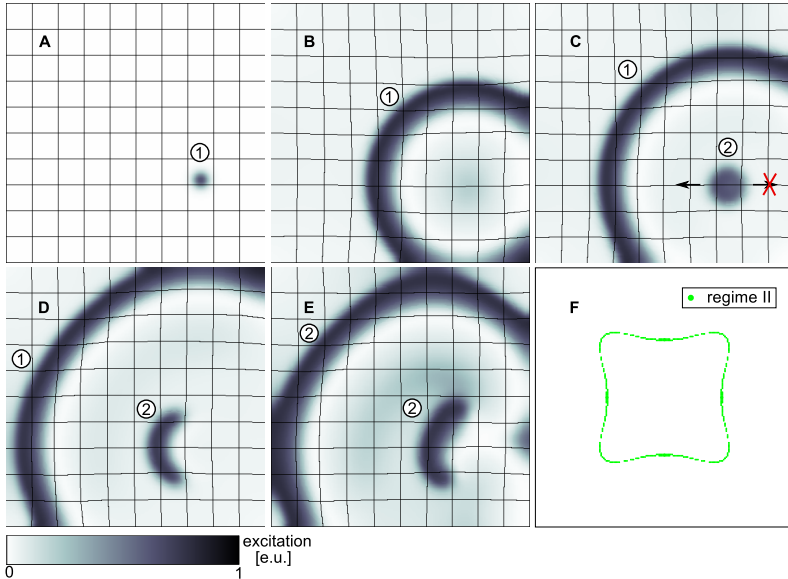


Figure 3.5. Spiral wave formation following a point stimulus. (A) A wave (1) forms as response to a point stimulus ($t = 2.0 t.u.$). (B) Wave (1) propagates radially and causes stretch and initiation of a wave (2) due to depolarizing stretch activated current I_s ($t = 19.5 t.u.$). (C) The wave (2) is unidirectionally blocked (indicated by arrows) in the mechanically induced vulnerable zone ($24.5 t.u.$). (D) Wave (2) forms a pair of counter rotating spiral waves ($32.0 t.u.$). (E) Spiral wave pair (2) after one rotation ($56.0 t.u.$). (F) Enclosed by green region: pacemaking regime, excluded by green region: quiescence regime, green region: critical region where a point stimulus initiates spiral wave dynamics. System size as in Figure 3.3 and $G_s = 2.0$.

nomenon.¹ We see that wave 2 is blocked unidirectionally towards the boundary of the medium (Figure 3.5D) initiating a pair of counter rotating spiral waves via the new mechanism (compare Figure 3.2). The surface area of this “critical region” is $\approx 0.8\%$ of the total surface area.

Such a scenario of mechanically induced spiral wave formation can also occur without a point stimulus. In [82] it has been shown that the curvature of a wave in a dRDM system similar to that used in this paper causes an asymmetric strain distribution in the medium. Curvature effects have been shown to be important for spiral wave initiation [85, 86]. One physiological example how a curvature of a wave front can be created is the diffraction of a travelling wave at an isthmus, which was studied extensively in cardiac electrophysiology [87]. In Figure 3.6 we show that such a diffraction event can also result in spiral wave initiation via the

¹See <http://bioinformatics.bio.uu.nl/danielw/thesis/supplemental/3rd-chapter/> for movie on spiral formation after a point stimulus.

new mechanism. We see that the initial wave 1 forms a curved wave front after

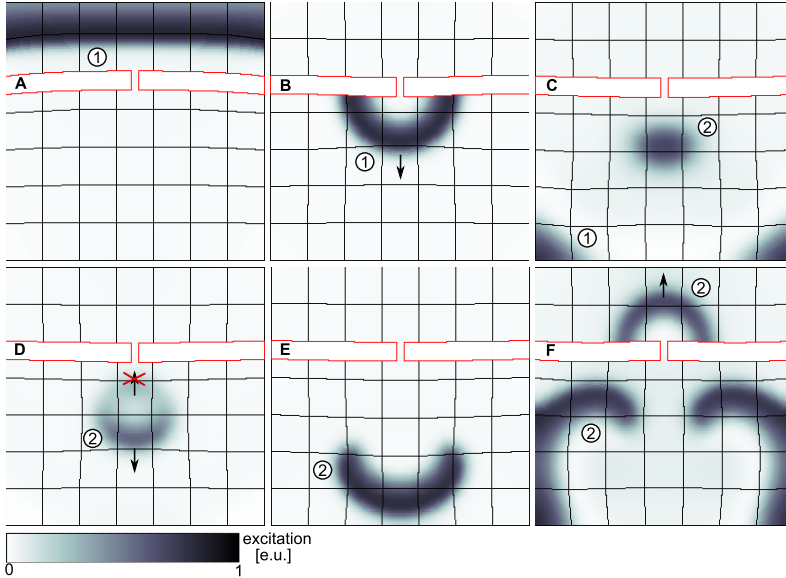


Figure 3.6. Spiral wave formation following a wave diffraction at an isthmus. (A) A plain wave (1) propagating towards an isthmus ($t = 5.5 t.u.$). (B) Wave (1) diffracted at the isthmus ($t = 20.5 t.u.$). (C) Wave (1) produces stretch activated current that initiates wave (2) ($t = 37.5 t.u.$). (D) Initiated wave (2) is unidirectionally blocked in the mechanically induced vulnerable zone of wave (1) ($t = 41.5 t.u.$). (E) Wave (2) forms a counter rotating spiral wave pair ($50.5 t.u.$). (F) Spiral wave pair after 1.5 rotations ($75.5 t.u.$). System size $42.0 s.u.$ and $G_s = 2.0$. Stiffness of the isthmus (contoured red) is twofold the stiffness in medium ($2 \times c$).

diffraction at an isthmus. The curvature of wave 1 leads to a region of maximal stretch in the focus of the curved wave 1 which initiates an additional wave 2. Wave 2 is blocked retrogradely to the propagation direction of wave 1 forming two spirals via the new mechanism.²

Another more complex scenario for mechanical spiral wave initiation is presented in Figure 3.7.³ We see a wave front propagating around an obstacle, where it gets curved and leads to a new wave initiation (Figure 3.7A,B). This new wave 2 itself is curved and initiates another wave 3 (Figures 3.7C,D). However, this new wave 3 is unidirectionally blocked retrogradely towards the propagation direction of wave 2, and thus a rotating spiral wave is initiated.

²See <http://bioinformatics.bio.uu.nl/danielw/thesis/supplemental/3rd-chapter/> for movie on spiral formation after a wave diffraction.

³See <http://bioinformatics.bio.uu.nl/danielw/thesis/supplemental/3rd-chapter/> for movie on spiral formation following a wave deflection.

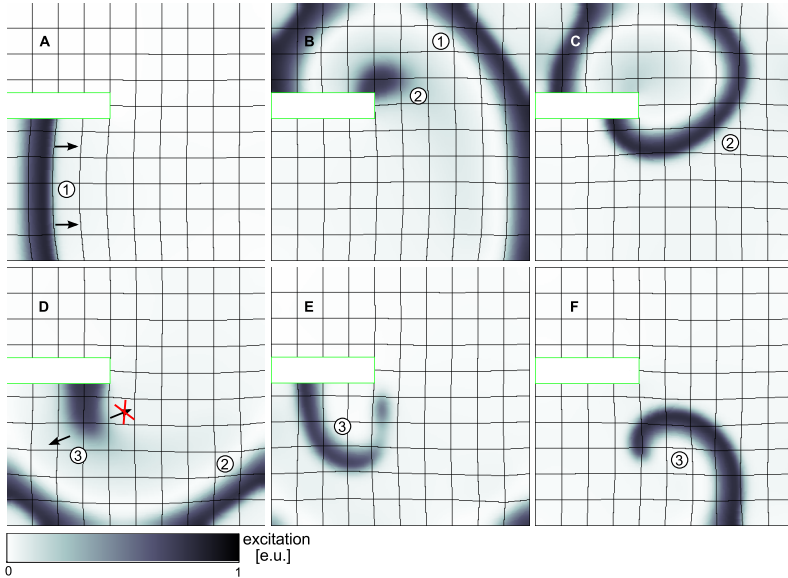


Figure 3.7. Spiral wave formation following a wave deflection. (A) A plain wave (1) propagating around a non-conducting static block ($t = 8.0 t.u.$). (B) Stretch caused by wave (1) initiates new wave (2) ($t = 41.8 t.u.$). (C) Wave (2) is propagating around non-conducting static block ($t = 53.8 t.u.$). (D) Stretch caused by wave (2) initiates wave (3) in mechanically induced vulnerable zone of wave (2) causing unidirectional block of wave (3) ($t = 71.8 t.u.$). (E) Wave (3) forms spiral wave ($t = 78.0 t.u.$). (F) Spiral wave (3) after one rotation ($t = 100.0 t.u.$). System size $60 s.u.$ and $G_s = 2.0$. The static block is contoured green.

In all examples shown above the formation of new spiral waves is caused by mechanically induced “close-to-threshold” stimuli which appeared in the areas of minimal threshold, thus in the areas prone to the new mechanism spiral wave initiation, reported in this article.

3.4 Discussion

In this paper we show that deformation can substantially affect the vulnerability of an excitable medium and induces a new vulnerable zone at longer coupling intervals than the “classical vulnerable zone”. In the mechanically caused vulnerable zone we found a new mechanism of spiral wave initiation which produces counter rotating spiral wave pairs with rotation directions opposite to spirals resulting from the “classical vulnerable zone”. This new vulnerable zone is located at

a region of maximal excitability in the back of an excitation wave. As a result this mechanism is relevant for waves initiated by weak stimuli, a scenario that occurs for example due to the stretch activated currents. We show on examples, that scenarios in which curvature is introduced to a wave of excitation, such as after a diffraction at an isthmus or deflection on a nonconducting inhomogeneous medium, can lead to asymmetric stretch distributions that may result in spiral wave initiation by the mechanism shown in this article.

All studies were performed with the dRDM model, which describes the mechanics of the medium in a discrete formulation. Another approach of modeling electromechanics uses continuous modeling frameworks. However, the dRDM approach has been shown to reproduce RDM phenomena previously found with a continuous modeling framework [82]. Thus we expect our results to hold true for continuous descriptions of cardiac mechanics.

The new vulnerable zone is located at longer coupling intervals compared to the “classical vulnerable zone”. It would be interesting to see if this new vulnerability can be seen in an experiment for electrical stimulation of cardiac tissue or mechanical stimulation mimicking the onset of the deadly heart arrhythmia “commotio cordis”, a state of chaotic excitation patterns following an impact on the heart tissue.

Note, that in our simulations the parameter range for the initiation of spiral waves, and for the generation of new pulses via stretch are close to each other. In [88] it has been suggested, that stretch can induce new pulses in cardiac tissue. We believe therefore, that under these circumstances it will also be possible to induce spiral waves by the mechanism shown in Figures 3.5-3.7 in this paper.

In this paper isometric boundary conditions (fixed boundaries) were applied. The change of the boundary conditions affects the stretch magnitude and distribution in the medium, and accordingly may shift parametric ranges of the observed phenomena. However, changes in boundary conditions do not change the basic effects of stretch activated currents, and thus conditions for the emergence of the mechanically caused vulnerability. Therefore, we expect that with other mechanical boundary conditions we will get similar results, provided that sufficiently large stretch is developed in the medium. Quantifying the effects of boundary conditions and geometry may be the subject of a following study.

We performed this study in a phenomenological low dimensional model of cardiac excitation. However, we think that the results will be reproduced in more detailed models, because the mechanism is based on the accommodation effect, which can be perfectly reproduced by ionic models.

The phenomenon “superexcitability” has been reported in various experimental studies [89, 90], and may be caused by factors not related to mechano-electrical feedback. As the basic requirement for our mechanism of spiral wave initiation,

besides a threshold stimulus, is only superexcitability, we can expect that it may also work in situations when it is not mechanically induced.

3.5 Acknowledgments

The authors are grateful to Dr. Martyn P. Nash, Dr. Rikkert H. Keldermann for valuable discussions. The authors furthermore thank Dr. Sarah LaPointe and Paul Baron for help with language editing of the manuscript and Jan Kees van Amerongen for excellent technical support.

Chapter 4

Emergence of Spiral Wave Activity in a Mechanically Heterogeneous Reaction-Diffusion-Mechanics System

LOUIS D. WEISE¹ AND ALEXANDER V. PANFILOV² (2011)

¹Theoretical Biology & Bioinformatics, Utrecht University, Utrecht, The Netherlands

²Department of Physics and Astronomy, Ghent University, Ghent, Belgium

Phys. Rev. Lett., **108**, 228104

Abstract

We perform a numerical study of emergent spiral wave activity in a two-dimensional reaction-diffusion-mechanics medium with a regional inhomogeneity in active and passive mechanical properties. We find that self-sustaining spiral wave activity emerges for a wide range of mechanical parameters of the inhomogeneity via five mechanisms. We classify these mechanisms, relate them to parameters of the inhomogeneity, and discuss how these results can be applied to understand the onset of cardiac arrhythmias due to regional mechanical heterogeneity.

4.1 Introduction

Spiral waves occur in various important excitable media. The most studied examples include spiral waves in the Belousov-Zhabotinski (BZ) reactions [12], and in the cardiac muscle where they underpin dangerous cardiac arrhythmias [3, 72].

Excitation waves can be described by reaction-diffusion (RD) partial differential equations; however, the excitation process is often coupled to deformation of the underlying medium, such as motion of amoebae of *Dictyostelium discoideum* [73] or swelling of a gel caused by BZ reactions [74]. The heart's pumping is governed by electrical waves of excitation; yet, its deformation also feeds back on the excitation processes of the cardiomyocytes. This phenomenon, which is known as "mechano-electrical feedback" (MEF), has been shown to be able to cause, but also to abolish, dangerous cardiac arrhythmias [9]. To study basic effects of MEF the reaction-diffusion mechanics (RDM) framework has been introduced [7], which couples RD to mechanical equations. Using the RDM framework, important phenomena were identified, such as self-organized pacemakers [43], initiation [91], drift and breakup [60] of spiral waves.

The most important problem in the theory of spiral waves is to understand mechanisms of their initiation, as it is a key to understanding the onset of cardiac arrhythmias. So far the main known mechanisms of spiral wave initiation are related to electrophysiological heterogeneity of cardiac tissue [5, 92–94], for example in duration of the refractory period of cardiac cells. Many forms of cardiac disease also cause mechanical heterogeneity in the heart. Although mechanical heterogeneity has been linked to the onset of arrhythmias, the mechanisms of spiral initiation due to mechanical heterogeneity have not been studied yet. Here, we perform a generic study with the aim to understand how regional heterogeneity in passive and in active mechanical properties may cause spiral wave activity using a discrete RDM (dRDM) model.

4.2 Model

The dRDM model is described in detail in [82]. Here we provide a short description of its main features. The dRDM model couples a two-variable FitzHugh-Nagumo-type RD model for cardiac excitation [28] with mechanics equations describing a finite-elastic, isotropic material.

$$\frac{\partial u}{\partial t} = \nabla^2 u - ku(u - a)(u - 1) - uv - I_s, \quad (4.1)$$

$$\frac{\partial v}{\partial t} = \epsilon(u)(ku - v), \quad (4.2)$$

$$\frac{\partial T_a}{\partial t} = \epsilon(u)(k_T u - T_a), \quad (4.3)$$

$$\mathbf{F}_{12} = p \left(\frac{T_a(1) + T_a(2)}{2} \right) \frac{\mathbf{l}_{12}}{\|\mathbf{l}_{12}\|}, \quad (4.4)$$

$$\mathbf{f}_{1a} = \left[c \left(\frac{\|\mathbf{l}_{12}\| - r_0}{r_0} \right) - d \frac{(\dot{\mathbf{l}}_{12} \cdot \mathbf{l}_{12})}{\|\mathbf{l}_{12}\|} \right] \frac{\mathbf{l}_{12}}{\|\mathbf{l}_{12}\|} + \mathbf{F}_{12}, \quad (4.5)$$

$$\mathbf{f}_{1p} = \frac{1}{2} \left[c \left(\frac{\|\mathbf{l}_{13}\| - \sqrt{2}r_0}{\sqrt{2}r_0} \right) - d \frac{(\dot{\mathbf{l}}_{13} \cdot \mathbf{l}_{13})}{\|\mathbf{l}_{13}\|} \right] \frac{\mathbf{l}_{13}}{\|\mathbf{l}_{13}\|}, \quad (4.6)$$

$$\sum_{\alpha=1}^N \mathbf{f}_{i\alpha} = m\ddot{\mathbf{x}}_i = 0, \quad (4.7)$$

$$I_s = G_s(\sqrt{A} - 1)(u - E_s), \quad (4.8)$$

where step function $\epsilon(u)$ sets time scales of recovery and contraction processes: $\epsilon(u) = 1$ for $u < 0.05$, and $\epsilon(u) = 0.1$ for $u \geq 0.05$. For undeformed tissue, Eqs.(4.1),(4.2) with transmembrane potential u and conductance of repolarizing current v , describe non-oscillatory cardiac tissue ($a = 0.08$, $k = 8$). We set up the mechanical model on a square lattice of mass points connected to up to $N = 8$ direct neighboring mass points with springs (see Figure 1 in [82]). Eq.(4.3) describes the development of active tension T_a as a function of tissue depolarization (term $\epsilon(u)k_T u$, with $k_T = 1.5$). Active contraction force is generated at each node and mediated via vertical and horizontal (“active”) springs. Eq. (4.4) describes the contraction force \mathbf{F}_{12} generated by an active spring \mathbf{l}_{12} connecting mass points 1 and 2. In Eq.(4.5), \mathbf{F}_{12} is added to the elastic force mediated by the active spring \mathbf{l}_{12} . Diagonal “passive” springs account only for passive forces. Eq.(4.6) describes the force \mathbf{f}_{1p} mediated at mass point 1 through a passive spring connecting mass points 1 and 3. Time derivatives of spring vectors are $\dot{\mathbf{l}}_{12}$ and $\dot{\mathbf{l}}_{13}$; c and d are the stiffness and damping constants (in bulk medium: $c = 1$, $m = 1$ and $d = 30 \times c$, in inhomogeneity: $d = 10 \times c$). Following previous studies on cardiac electromechanics [7, 43, 60, 82, 91], we assumed elastostatics [see Eq (4.7)]. As in [43, 60, 82, 91], we describe MEF as depolarizing stretch-activated currents I_s [9] given by Eq. (4.8) with ($E_s = 1$ and $G_s = 2.5$), where variable A is the normalized surface area (relative to undeformed reference surface area) of a square formed by 4 direct neighboring mass points connected with active springs. Stretch activated current I_s is active if $A > 1$ (stretch).

The model was solved with the explicit Euler method for the RD system and the Verlet integration scheme for the mechanical model with time step $m\tau = 0.01$, convergence threshold $thr = 2 \times 10^{-5}$, Euler time step $\Delta t = 0.001$ (time units [t.u.]) and space step of $\Delta x = \Delta y = 0.3$ (space units [s.u.]) [82]. We used a

quadratic deforming grid of 101×101 mass points and 202×202 finite difference points using no-flux boundary conditions. The boundaries of the medium were fixed in space to mimic isovolumic phases in the cardiac cycle, an assumption that has been made also in previous electromechanical studies [43, 60, 82, 91].

We used a 60×60 *s.u.*² model with a regional mechanical inhomogeneity of size 18×30 *s.u.*² located close to the center of the medium (see Figure 4.1). We altered the passive (parameter *c*) and active mechanical properties (parameter *p*) in this region for different simulations, where we initiated a traveling wave from one side of the medium (see Figure 4.1) and computed for 200 *t.u.*.

4.3 Results

We found that self-sustaining spiral waves emerge in the model via several mechanisms in a large range of parameters *c* and *p* of the inhomogeneity. We will first illustrate the phenomenon of emergent spiral wave patterning and sketch underlying mechanisms. Figure 4.1 and movies submitted as Supplemental Material¹ illustrate the mechanisms of spiral wave initiation. Figure 4.1 I illustrates the first mechanism of spiral wave formation. An extra pulse ② forms in the heterogeneous region in the back of the initially stimulated wave ① at time 36 *t.u.*. Then the propagation of this new wave ② is blocked counter to the propagation direction of wave ① [Figure 4.1 I, 36 *t.u.*], and as a result a pair of counter rotating spiral waves is formed [Figure 4.1 I, 48 *t.u.*, 60 *t.u.*]. Figure 4.1 II illustrates the second mechanism of spiral wave formation. Following initial wave ① waves ② and ③ are formed, but they do not cause spirals. At time 63 *t.u.* a pulse ④ forms in the inhomogeneity which is blocked toward a previous wave ③ inducing a pair of counter-rotating spiral waves (72 *t.u.*). Note, that in contrast to mechanism I, wave block occurs in accordance with a classical pinwheel protocol for spiral wave formation, when conduction block occurs at the recovery tail of the preceding wave [2]. Figure 4.1 III illustrates the third mechanism of spiral wave formation. At time 24 *t.u.* a wave breaks at the inhomogeneous region and forms two rotating spiral waves (36 *t.u.*, 48 *t.u.*, 60 *t.u.*).

Furthermore, we found mechanisms which are related to an incomplete excitation in the inhomogeneous region. Figure 4.1 IV' illustrates the fourth mechanism of spiral wave formation. At time 26 *t.u.* we see that a pulse ④ forms in the inhomogeneity that does not result in a traveling wave but disappears (29.2 *t.u.*). However, it produces a temporarily inexcitable region (29.2 *t.u.*), and another wave ③ breaks at this region at time 33.0 *t.u.* producing a pair of spiral waves (48.0 *t.u.*). If this wave ④ is stronger and can exit the inhomogeneity partially, it can result in formation of spiral waves by another fifth mechanism (Figure 4.1 IV''): At

¹See <http://bioinformatics.bio.uu.nl/danielw/thesis/supplemental/4th-chapter/> for movies on mechanisms (I-V'').

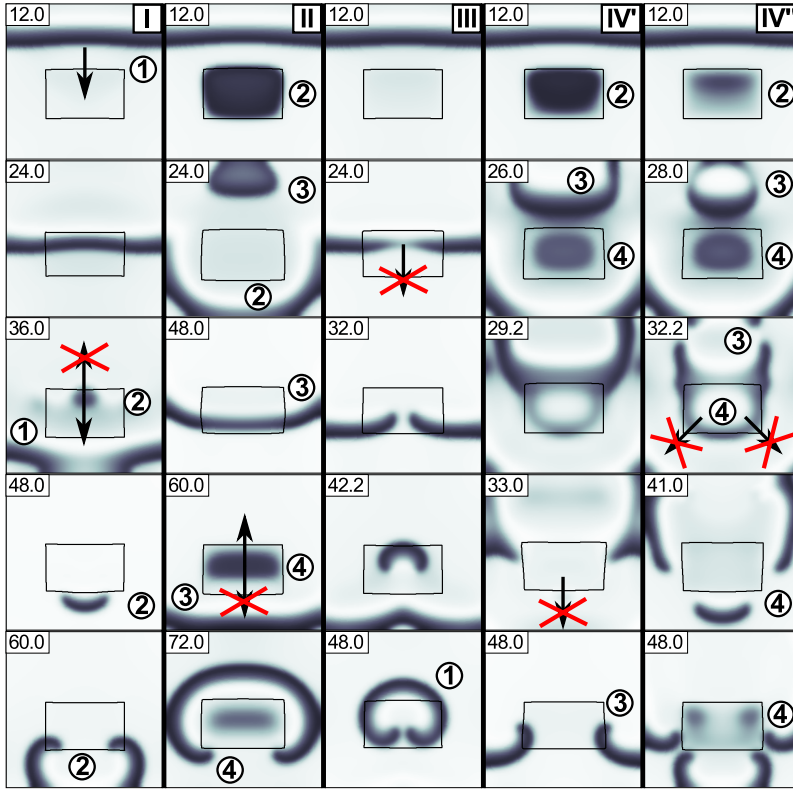


Figure 4.1. Mechanisms (I-IV') of spiral wave formation caused by a mechanical inhomogeneity. The mechanical parameters (p, c) in the inhomogeneity are I: $(1.00, 0.51)$, II: $(0.00, 0.75)$, III: $(0.50, 1.20)$, IV: $(0.25, 0.68)$, and IV': $(0.25, 0.92)$. Wave blocks are indicated by red, crossed arrows. Waves are labeled by order of appearance. Simulation time [t.u.] of a snapshot is shown in its upper left corner.

time $28 t.u.$, we see that a pulse ④ forms in the inhomogeneity similar to the previous case, and here this wave forms a traveling wave. However, it gets blocked in diagonal directions to form pairs of spiral waves ($41 t.u.$, $48 t.u.$). Note, that we initiated only one propagating “initial wave”, and all other waves emerged in the medium due to MEF. Waves can emerge prior the initial wave, which we will call a “premature beat” (wave ② in Figures 4.1 II, IV', IV'' the upper row), or behind the initial wave (wave ② in Figures 4.1 I at $36.0 t.u.$, and wave ④ in Figure 4.1 II at $60.0 t.u.$). Furthermore, we found that pacemakers can form in the medium.

We find that most mechanisms for spiral wave initiation are caused by MEF and accommodation. Accommodation is the phenomenon of a decrease of excitability caused by a relatively weak depolarizing current, which has been studied in electrophysiology since 1936 [18, 84]. In our model, accommodation is caused

by stretch of the tissue which causes a depolarization via I_s .

We will now outline the mechanisms of spiral wave formation. In mechanism I, stretch behind the traveling wave initiates a secondary wave at the region of maximal local excitability [91]. As this wave propagates towards regions of lower excitability, it is blocked as is illustrated in Figure 4.1 I. This mechanism for spiral formation was reported for a homogeneous tissue in [91]. In mechanism II a pulse is also caused via stretch behind the traveling wave; however here, wave block occurs in the opposite direction due to proximity of this pulse to the refractory tail of the preceding traveling wave. In mechanism III the initial wave stretches the inhomogeneous region in front of itself decreasing its excitability due to accommodation. As a result, the traveling wave breaks at the inhomogeneous region. This mechanism was first reported in [60] in two-dimensional (2D) and in whole heart models in [65, 66]. In new mechanisms IV' and IV'' a stretch of the inhomogeneous region causes a wave response. However, accommodation causes decreased excitability, and thus it may result in an overall block of propagation, and thus, a temporary inexcitable region in the inhomogeneity (mechanism IV') which can break other waves, or result in a partial exit of the wave from the inhomogeneity causing local breaks (mechanism IV''). Note, that mechanisms III and IV' are similar to an important mechanism of spiral wave formation in which wave block happens due to an inhomogeneity with a prolonged refractory period [92]; however, in our case these breaks occur only due to mechanical inhomogeneity.

We will now report the regimes as a function of (p, c) . Figure 4.2 illustrates emergent wave patterning as a function of mechanical properties of the inhomogeneity. The white region in Figure 4.2 illustrates the parametric space (p, c) where the initial wave does not produce any secondary waves. Black dots in Figure 4.2a indicate simulations when a premature beat was induced, red dots when no premature beat but other wave patterning occurred. The boundary of the “patterning region” is given by two straight lines², which reflects the linearity of the elastic model. The positive and negative slopes reflect different mechanisms of patterning. During the formation of a premature beat, active tension p counteracts the passive tension c during formation of a pulse in the heterogeneity, while for a wave originating behind the initial wave, a stronger contraction of the heterogeneity itself (p) increases the stretch behind that wave and thus favors formation of this additional pulse. Figure 4.2b shows spiral wave formation in the experiment for a large parametric range. We studied the (p, c) -space with resolution $(\Delta p = 0.05, \Delta c = 0.05)$, and found 425 simulations that lead to emergent wave patterning. In 239 of these 424 patterning cases, spiral waves emerge (56%), in 99 simulations (23%) pacemaking activity [43] occurs, and in 87 simulations (20%) a single premature beat happens. In the 239 cases that cause spiral wave activity mechanism III occurs 81 times (34%), mechanism I happens 80

²Regression analysis ($c = b \times p + a$) yields $a = 2.22 \pm 0.01$, $b = -2.10 \pm 0.02$, $R^2 = 0.998$ for the left line, and $a = -0.14 \pm 0.03$, $b = 0.64 \pm 0.02$, $R^2 = 0.986$ for the right line.

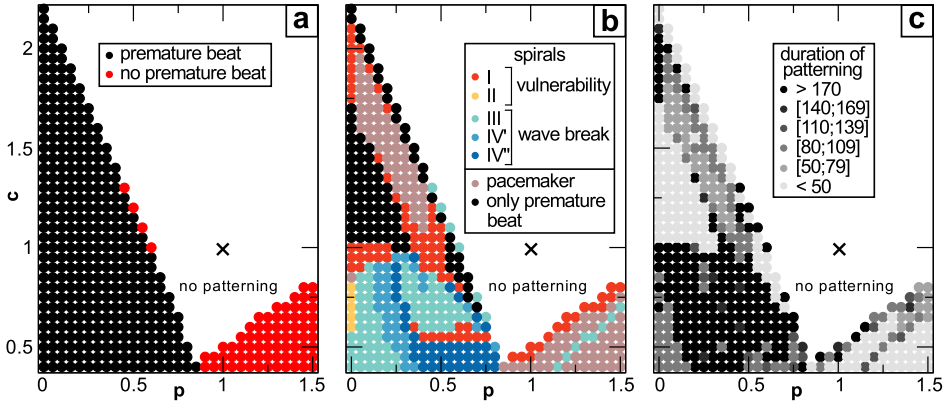


Figure 4.2. Wave patterning as function of mechanical parameters p and c of the inhomogeneity. Black crosses indicate condition ($p = c = 1$). Colored dots indicate the wave patterning regime. “No patterning” labels the white region where the initially stimulated traveling wave propagates through the medium without producing new waves. (a) Patterning with (black) and without (red) premature pulse. (b) Single premature beat (black), pacemaker (brown), spiral formation: (red, orange) due to vulnerability, (blue tones) due to wave break. (c) Duration of wave patterning [t.u.].

times (33%), mechanism IV” 41 times (17%), mechanism IV’ 32 times (13%) and mechanism II occurs 5 times (2%). Figure 4.2c shows the observed duration of wave patterning as a function of (p, c) in the inhomogeneity. We see that spiral wave patterning can often sustain in the model for a long simulation time: in 160 of the 239 cases (67%) patterning sustained longer than 200 $t.u.$ (≈ 10 spiral periods). For mechanism I it was 85% (51 of 60 cases), for mechanism II (2 of 5), 64% for mechanism III (52 of 81), 97% for mechanism IV’ (31 of 32), and 56% for mechanism IV” (23 of 41).

We have also studied the longer term dynamics of wave patterning on representative examples for each of the mechanisms (see Figure 4.3 and movies submitted as Supplemental Material ³). We see that for the examples for mechanisms I, II, III and IV’ [Figure 4.3a- 4.3d], the activity sustained beyond the simulation time, whereas for example IV” activity eventually terminated. For mechanisms II, III and IV’ [Figure 4.3b- 4.3d], wave patterning included spirals and pacemakers. We see in all examples dynamic appearance and disappearance of spiral waves via various mechanisms; however, most frequently it occurs by mechanism III (accommodation).

Now, we will use our results to make predictions. Mechanical heterogeneity can occur due to different processes in the heart. The most common is myocardial

³See <http://bioinformatics.bio.uu.nl/danielw/thesis/supplemental/4th-chapter/> for movies on dynamics of emergent spiral wave activity.

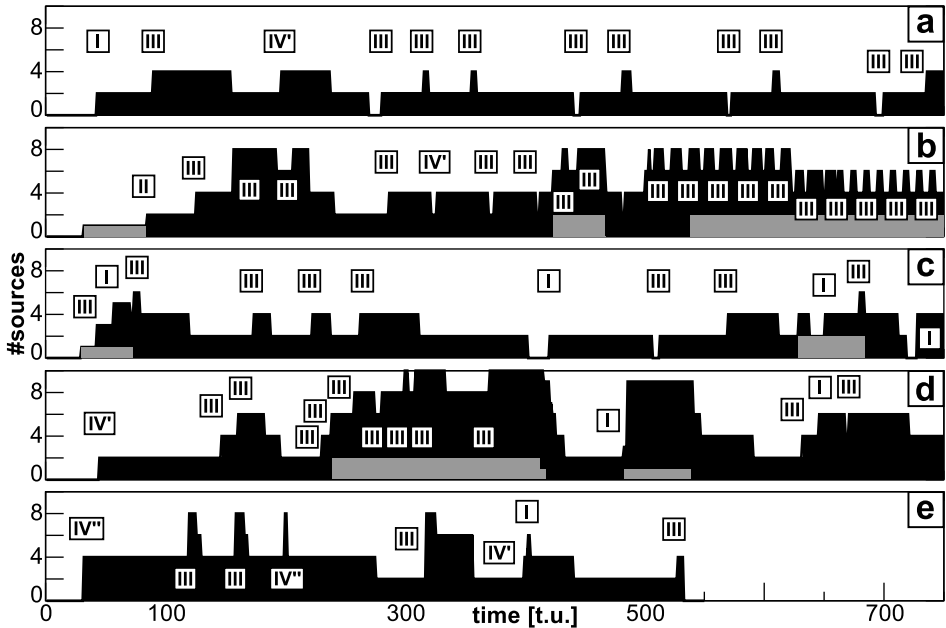


Figure 4.3. Self-sustaining spiral wave activity. Number of wave sources ('#sources' shown as black line, number of pacemakers shown as grey bars) and mechanisms of spiral formation (I-IV'') are plotted against simulation time. Mechanical parameters (p, c) in the inhomogeneity are (a): (0.90, 0.45), (b): (0.00, 0.80), (c): (0.50, 0.70), (d) (0.40, 0.80), (e) (0.70, 0.45).

ischaemia, where a region of the heart receives insufficient blood flow which can result in infarction, when a part of cardiac muscle tissue is damaged or dead. In acute ischaemic cardiac tissue, the contraction twitch and the stiffness are reduced [95, 96], which can be modeled in a RDM model by a decrease in active contractile force scaling p and decrease in stiffness c , or increase in c for late infarction. Based on results shown in Figure 4.2, we can expect that during acute ischaemia (lower c and p) the leading mechanism of arrhythmia onset are III and IV with the occurrence of premature beats. And indeed, a previous whole-heart modeling study on acute ischaemic cardiac tissue predicted formation of premature beats and formation of spirals due to mechanism III [66], where mechanical inhomogeneity was modeled by equally downscaling stiffness and active tension in acute ischaemic tissue up to 25%. For the late infarction state, where stiffness is increased (low p , high c), our model predicts occurrence of premature beats and spiral formation mainly via mechanism I. Another possibility may be related to a neurogenic cardiac regulation. A local release of catecholamines (e.g. resulting from local sympathetic nervous activity) could increase active tension (increase in p) in a region. In that case our model predicts that the most likely mechanism for spiral formation is mechanism I without the occurrence of pre-

ture beats. Note that the parametric region in which spiral waves emerge is small here.

4.4 Discussion

In this letter we identified 5 mechanisms of spiral wave initiation in a heterogeneous RDM system. The leading mechanisms of spiral wave formation in (p, c) turned out to be I “non-classical vulnerability”, and III “accommodation” (67% in total), whereas “classical vulnerability” II accounted for only 2%. In this study, we stimulated a single initial wave and further waves were caused by MEF. We expect that further mechanisms might be found with the RDM approach, if, for example, a high frequency stimulation protocol would be applied.

Relating mechanisms I-IV” to parameters p, c is a complex problem as it requires a study of the interplay of the deformation field with other emergent properties as curvature of wave fronts and vulnerability phenomena. The main aim of this letter was to describe the observed patterns and classify them for a particular mechanical setup. More work is necessary to obtain a better understanding of complex relations between observed regimes and model parameters. It could be interesting to generalize the analytical approach of Alvarez-Lacalle and Echebarria [97] for a nonhomogenous 2D case or use other methods, for instance singular perturbation theory, to analytically study the effect of MEF on spiral wave formation.

The results of our study might be tested in 2D electromechanical experimental systems, such as myocardial tissue slices [98] and cell cultures [99]. Heterogeneity can be induced by various means. For example, ischaemia can be mimicked by covering a cell culture with a glass coverslip [100].

4.5 Acknowledgements

We thank Dr. Martyn P. Nash and Dr. Rikkert H. Keldermann for valuable discussions and Jan Kees van Amerongen for excellent technical support. This research is funded by the Netherlands Organization for Scientific Research (NWO Grant No. 613.000.604).

Chapter 5

A Discrete Electromechanical Model for Human Cardiac Tissue

LOUIS D. WEISE¹ AND ALEXANDER V. PANFILOV² (2011)

¹Theoretical Biology & Bioinformatics, Utrecht University, Utrecht, The Netherlands

²Department of Physics and Astronomy, Ghent University, Ghent, Belgium

in preparation

Abstract

We introduce an electromechanical model for human cardiac tissue which couples a biophysical model of cardiac excitation (Tusscher, Noble, Noble, Panfilov, 2006) and tension development (Niederer, Hunter, Smith, 2006 model) with a discrete elastic mass-lattice model. The passive mechanical properties of the mass-lattice model are described by a generalized Hooke's law for finite deformations (Seth material). In our approach equations for electrical excitation are solved using a finite difference approach, and equations of the mass lattice model are solved using a Verlet integration scheme. The active mechanical contraction is initiated by changes of the intracellular calcium concentration which is a variable of the electrical model. Mechanical deformation in turn affects the electrical system via stretch activated ionic channels whose conductivity is controlled by the local stretch of the medium. In an initial set of simulations we study how stretch activated currents affect the shape of the action potential, the action potential duration and conduction velocity restitution, and dynamics of spiral waves. We show an example of emergence of spiral wave activity in a medium with complex geometry.

5.1 Introduction

The heart's pumping function is controlled by electrical waves of excitation which propagate through the cardiac muscle and initiate its contraction. Abnormal electrical excitation of the heart may result in cardiac arrhythmias which disturbs the heart's pumping and cause its failure. Heart failure due to cardiac arrhythmias is a major cause of death in the industrialized world [1]. Mechanisms of arrhythmias initiation are largely unknown and some of them are caused by spiral waves of electrical excitation in the cardiac muscle [2–4].

Electrical waves of excitation not only initiate cardiac contraction, but are also affected by tissue deformation via the electromechanical feedback phenomenon. It was shown that rapid stretch of cardiac tissue (mechanical stimulation) can initiate electrical waves of excitation [9, 10]. Two important clinical examples are “commotio cordis” [101, 102], the phenomenon when an abrupt impact of an object on the chest causes arrhythmia; another example is the precordial thump: the phenomenon that a strong impact on the chest of a patient may stop arrhythmia [103]. In both of these examples the phenomena are believed to be a result of an abrupt deformation of the heart, and the main effect of deformation on the electrical activity is considered to be transmitted via so-called stretch activated channels. These channels produce a depolarizing inward current as a response to stretch of the tissue [9]. In view of these and other known effects the study of effects of mechano-electrical feedback is an important direction of research in current cardiac electrophysiology [104]. An important method used to study electromechanical effects is mathematical modeling, which allows to control both mechanical and electrical activity, which is a difficult problem in experimental research.

Examples of such modeling studies include a series of papers on the onset of pacemakers and dynamics of spiral waves due to mechano-electrical feedback, where low dimensional models for cardiac tissue and a continuous finite element approach for cardiac mechanics was used [43, 60, 105]. In our papers [91, 106] we studied possible mechanisms of initiation of cardiac arrhythmias also using a low dimensional model for cardiac tissue and a discrete representation of cardiac mechanics.

Low dimensional models for cardiac tissue used in the mentioned papers can provide important insights into electromechanical processes; however, they are limited to a qualitative level. The next natural step in modeling cardiac electromechanical activity is the development of detailed biophysical models for contracting cardiac tissue which consider the heart's geometry and fiber anisotropy. First steps in that direction have been made using a continuous mechanical approach coupled to biophysical models of cardiac excitation and contraction [65, 66]. Here, we develop a detailed biophysical model for cardiac

excitation and contraction coupled to a discrete mechanical model. An advantage of this method is its high computational efficiency which allows to obtain high spatial and temporal resolution. In this approach we use an ionic model of cardiac excitation for human cardiac cells (Tusscher, Noble, Noble, Panfilov 2006 model) [19, 27] and a biophysical model for excitation-contraction coupling (Niederer, Hunter, Smith, 2006 model) [36, 44]. In this paper we describe the setting up of the model, and address numerical and computational techniques to solve the coupled excitation-contraction equations. Using this model we study effects of stretch-activated currents on the action potential shape, and action potential duration (APD) and conduction velocity (CV) restitution, and the dynamics of spiral waves. Furthermore, we study emergence of spiral waves in a medium with complex geometry.

5.2 Model

5.2.1 Model for Cardiac Excitation

We use the 2006 version of the Tusscher Noble Noble Panfilov model for human epicardial myocytes (TP06) [19, 27]. The model is given as the following reaction-diffusion equation for the transmembrane potential V

$$\frac{\partial V}{\partial t} = \nabla D \nabla V - \frac{I_{ion}}{C_m}, \quad (5.1)$$

with the membrane capacitance density $C_m = 2.0 \mu F/cm^2$, and the diffusivity $D_{ij} = \delta_{ij} \times 0.00154 cm^2/ms$, and the transmembrane ion current

$$\begin{aligned} I_{ion} = & I_{Na} + I_{K1} + I_{to} + I_{Kr} + I_{Ks} + I_{CaL} + I_{NaCa} + \\ & I_{NaK} + I_{pCa} + I_{pK} + I_{bCa} + I_{bNa} + I_{sac}, \end{aligned} \quad (5.2)$$

where I_{Na} is fast Na^+ current, I_{CaL} is L-type Ca^{2+} current, and the K^+ currents are I_{to} (transient outward), I_{Kr} (rapid delayed rectifier), I_{Ks} (slow delayed rectifier), and I_{K1} (inward rectifier). Furthermore, I_{NaK} is the Na^+/K^+ pump current, I_{NaCa} is the Na^+/Ca^{2+} exchanger current, I_{pCa} , I_{pK} are plateau Ca^{2+} and K^+ currents, and I_{bCa} , I_{bNa} are background Ca^{2+} and Na^+ currents. The voltage dependency of ion channels is modeled by gating variables with dynamics of the form [18]

$$\frac{dn}{dt} = \frac{n_\infty - n}{\tau}, \quad (5.3)$$

where n_∞ describes the voltage-dependent steady state activation/inactivating, and τ the voltage-dependent characteristic time for a respective gating variable. The TP06 model also describes Ca^{2+} dynamics of intracellular compartments of

sarcoplasmic reticulum. A full list of parameters and equations for these currents is given in [27].

In our model we add a stretch activated depolarizing current I_{sac} which will be introduced later in Eq.(5.11). By I_{sac} the deformation of the medium feeds back on its excitation state.

We will now describe the coupling of the electrical excitation process of the cardiomyocytes to their tension development.

5.2.2 Excitation-Contraction Coupling Model

We model myocyte excitation-contraction coupling in our model with a numerically improved version of the Niederer, Hunter, Smith (NHS) model [36, 44]. The NHS model describes active tension in a sarcomere as a function of intracellular calcium concentration $[Ca^{2+}]_i$, sarcomere length and the rate of sarcomere length change, determinants which have been shown to substantially affect the active tension development (see [36] and references within).

Measure of Strain

The NHS model takes the dynamics of sarcomere length into account, however our generic elastic model (see section “mass lattice model”) has no sarcomere length defined as it describes an isotropic 2D medium. Therefore we follow previous studies [43, 82, 91, 106] and define as a pseudo normalized sarcomere length λ as

$$\lambda = \sqrt{\frac{A}{A_0}}, \quad (5.4)$$

where the A is the surface area of a smallest area element in the model (see mechanics section) and A_0 is the surface area of such a smallest area element in undeformed state.

Model Adjustments for Human Ventricular Cells

We followed changes on the original version of the NHS model [36], which was originally set up using experimental data of rat and guinea pig hearts, that have been made in the work [65] to model human ventricular myocytes. These changes were explained by experimentally observed relaxation rates due to higher body temperatures [107], namely a speeding up of myocyte relaxation rates $\alpha_{r1} = 10 \text{ s}^{-1}$, $\alpha_{r2} = 25 \text{ s}^{-1}$, and adjusting the contractile tension by setting

parameters $T_{ref} = 125 \text{ kPa}$ (maximum tension at resting length of sarcomere) and $p[\text{Ca}]_{50} = 6.5$ ($p[\text{Ca}^{2+}]_i$ at half maximal contraction tension).

Active Tension in Myocytes

The NHS model describes the tension T_a that is developed in cross bridges as

$$T_a = \widehat{T}K(Q_i)\alpha, \quad (5.5)$$

$$\widehat{T} = T_{ref}\left(\frac{z}{z_{max}}\right), \quad (5.6)$$

where \widehat{T} is the length and velocity independent tension, (z/z_{max}) is the fraction of the available actin sites in a sarcomere z to the maximal available actin sites z_{max} at a particular sarcomere length, and the scaling functions α and $K(Q_i)$ describe the sarcomere length and velocity dependencies of the total tension. In particular, the function α models the influence of the dynamics of the cross bridge cycle and thin filaments in a sarcomere, and function $K(Q_i)$ accounts for the velocity dependency of tension development via a fading memory model. We use the “update method” on the NHS model described in [36], where the functions $K(Q_i)$ and α are calculated within the mechanical iteration algorithm to calculate the total tension T_a via Eq.5.5. For a detailed model description and parameters, see [36, 44].

We will now describe the coupling of the tension development of the medium to its elastic properties.

5.2.3 Mass-Lattice Model

We use the mass-lattice framework introduced in [82] to describe an isotropic material following a linear force-displacement relation described by the Seth material relation [77, 78, 82]. The model describes a square lattice in which each mass point is connected to $N = 8$ (if not at a boundary) direct neighboring mass points with springs (see Figure 2.1). The equations of the model are

$$\mathbf{F}_{12} = \frac{1}{\sigma_N} \left(\frac{T_a(1)+T_a(2)}{2} \right) \frac{\mathbf{l}_{12}}{\|\mathbf{l}_{12}\|}, \quad (5.7)$$

$$\mathbf{f}_{1a} = \left[c \left(\frac{\|\mathbf{l}_{12}\| - r_0}{r_0} \right) - d \frac{(\dot{\mathbf{l}}_{12} \cdot \mathbf{l}_{12})}{\|\mathbf{l}_{12}\|} \right] \frac{\mathbf{l}_{12}}{\|\mathbf{l}_{12}\|} + \mathbf{F}_{12}, \quad (5.8)$$

$$\mathbf{f}_{1p} = \kappa \left[c \left(\frac{\|\mathbf{l}_{13}\| - \sqrt{2}r_0}{\sqrt{2}r_0} \right) - d \frac{(\dot{\mathbf{l}}_{13} \cdot \mathbf{l}_{13})}{\|\mathbf{l}_{13}\|} \right] \frac{\mathbf{l}_{13}}{\|\mathbf{l}_{13}\|}, \quad (5.9)$$

$$\sum_{\alpha=1}^N \mathbf{f}_{i\alpha} = m\ddot{\mathbf{x}}_i = 0. \quad (5.10)$$

Each mass point is connected to its 4 diagonal neighbors with “passive springs” (passive elastic properties), and to its 2 vertical and 2 horizontal neighbors with “active springs” (passive and active forces). In Eq. (5.7) we use T_a from Eq. (5.5) to describe excitation-contraction coupling of two neighboring mass points 1 and 2 connected with an active spring, where σ_N is the mass point surface density (a function of mesh coupling parameters, see numerics section). Eqs. (5.8),(5.9), respectively, describe forces $\mathbf{f}_{1a} = -\mathbf{f}_{2a}$ mediated through an active spring to mass points 1 and 2, and forces $\mathbf{f}_{1p} = -\mathbf{f}_{3p}$ mediated through a passive spring to mass points 1 and 3. In Eqs. (5.8),(5.9) the spring vectors are given by mass point’s positions as $\mathbf{l}_{12} = \mathbf{x}_2 - \mathbf{x}_1$ and $\mathbf{l}_{13} = \mathbf{x}_3 - \mathbf{x}_1$, r_0 is the resting length of an active spring and $\sqrt{2}r_0$ the resting length of a passive spring, $\dot{\mathbf{l}}_{12} = \mathbf{v}_2 - \mathbf{v}_1$ and $\dot{\mathbf{l}}_{13} = \mathbf{v}_3 - \mathbf{v}_1$ are the time derivatives of the respective spring vectors $\mathbf{l}_{12}, \mathbf{l}_{13}$. Parameter c is the stiffness constant, and d is the damping parameter. In this paper we used a spring stiffness c of 1.25 N/cm (unless stated otherwise), and following [91] a damping value for bulk medium of $30 \times c$ (dimensionless). Parameter $\kappa = 1/2$ is the stiffness ratio between active and passive springs which causes that the lattice the lattice is macroscopically isotropic [76] for small deformations, and in good approximation for finite deformations that occur in this paper [82]. Using this relation yielded in maximal deformations of springs of 15% similar to contracting cardiac cells. Forces $\mathbf{f}_{1a}, \mathbf{f}_{1p}$ are functions of mass point’s positions $\mathbf{x}_1, \mathbf{x}_2, \mathbf{x}_3$, velocities $\mathbf{v}_1, \mathbf{v}_2, \mathbf{v}_3$, and $T_a(1), T_a(2)$ forming the active force distribution through Eq. (5.7). Each mass point follows Newton’s law of motion, and we compute Eq. (5.10) to mechanical equilibrium to determine the steady state configuration of the lattice for each given distribution of active forces. Note, that the pseudo normalized sarcomere length λ is a function of the relative change of the surface area of a quadrilateral formed by 4 neighboring mass points (see Figure 1 in [82]). We used λ and its rate of change in Eq. (5.5) to calculate the total contractile tension T_a which is updated during these computations according to the “update algorithm” suggested in [44]. The mass density of myocardial tissue is around 1.055 g/ml [108], and with a mass point volume density of $\frac{1}{8\Delta x^3} = 1000 \text{ ml}^{-1}$ a corresponding mass for a single mass point in our model is $\approx 11 \text{ mg}$. However, numerically we may choose m as we like as we assume elastostatics, also the Verlet time τ and the viscosity d can be chosen to assure efficient and accurate numerical computations. Following [82] we set m to the identical numerical value of c ($m = 0.1 \text{ mg}$) to achieve stable and efficient computations.

We will now describe how deformation feeds back on the excitation state of the medium.

5.2.4 Mechano-Electrical Feedback

The deformation of a cardiomyocyte affects its excitation processes. It has been shown in studies of excised cardiac tissue and the whole heart that a direct physiological influence of contraction on cardiac tissue is depolarizing stretch-activated current I_{sac} (compare Eq. (5.2)) through stretch activated channels [9]. Experimental studies have shown that these channels are activated instantaneously with mechanical stretch and follow a linear current-voltage relationship [61, 62]. Linear, time-independent models have been proposed for I_{sac} [63, 64], and have been used in other electromechanical models [43, 60, 65]. Following these previous studies we use the equation

$$I_{sac} = G_s \frac{(\lambda - 1)}{(\lambda_{max} - 1)} (V - E_s), \text{ for } \lambda > 1 \text{ (stretch)} \quad (5.11)$$

where G_s is the maximal conductance, E_s is the reversal potential of the stretch activated channels. For E_s values around $[-20; 0]$ mV have been reported [109, 110], and we set $E_s = 0$ mV . It has been shown that G_s varies between $[0; 100]$ S/F [9, 111]. In this study we vary G_s in a range of $[0; 100]$ S/F to study the influence of I_s on several properties. Parameter λ_{max} is the maximal pseudo normalized sarcomere length which we set to $\lambda_{max} = 1.1$ (cells can be stretched maximally 10%) as in [65].

5.2.5 Numerical Methods

We solved the model with an explicit Euler method for the TP06 model of cardiac excitation and the NHS model, and the Verlet integration scheme [79] to solve the mechanical model. After each Euler computation of the electrical system a new $[Ca^{2+}]_i$ is obtained, a length and velocity independent tension \hat{T} is computed via Eq. (5.6). The independent tension \hat{T} is then passed to the mechanics model, where the mechanical equations are solved with a Verlet integration time step $m\tau = 0.01$ until the sum of forces on each mass point is smaller than a threshold $thr = 0.05$ mN (unless stated otherwise). During the mechanical iteration algorithm the length and velocity dependent tension scaling functions $K(Q_i)$ and α of the total tension T_a which is computed via Eq. (5.5) are updated together with the mesh configuration using the “update-method” [44]. Note, that in this paper the “update method” is applied within the Verlet routine on discrete nodes, whereas in the original work [44] the method is used within a Newton step to solve equations of continuum mechanics; moreover, here not an actual sarcomere length, but as for the MEF calculation a pseudo normalized sarcomere length λ from Eq. (5.4) is applied. For simulations we used an Euler integration space step from $\Delta x = \Delta y = 0.05$ cm to 0.025 cm and Euler integration time step of $\Delta t = 0.02$ ms . We computed a quadratic deforming grid of up to 603×603 finite difference (and 301×301 mass) points using no-flux boundary conditions

modeling a thin quadratic layer of up to $30 \times 30 \text{ cm}^2$ cardiac tissue. The boundaries of the deformable medium were fixed in space modeling isometric contraction to mimic isovolumic phases in the cardiac cycle, an assumption that has been made also in previous electromechanical studies [43, 60, 82, 91].

5.2.6 Model Validation

The numerical coupling and integration of the Euler and the Verlet scheme require the choice of several parameters. We will first discuss the integration parameters and then parameters for the coupling of the numerical grids to assure efficient and stable computations.

Integration Parameters

It has been shown that the TP06 model together with the improved NHS model coupled to a whole heart continuum mechanics model can be stably integrated with the Euler method using integration parameters $\Delta t = 0.02 \text{ ms}$ and $\Delta x = \Delta y = 0.05 \text{ cm}$ where the mechanical configuration has been updated after every 100's Euler step [65]. We use Euler integration steps of $\Delta t = 0.02 \text{ ms}$ and $\Delta x = \Delta y = 0.05 \text{ cm}$ as in [65] for most computations, and use stricter settings $\Delta x = \Delta y = 0.025 \text{ cm}$ for computations on spiral wave dynamics. We update the mechanical configuration after each Euler step, and achieve stable and accurate integration of the coupled electromechanical model. For solving the mechanical Eqs. (5.8)-(5.10) we use a Verlet integration time step of $m\tau = 0.01$, which we also used in [82]. We find, that also in the present study this setting allows to swiftly and stably compute a new configuration of the mechanical grid under conditions as in the simulations shown in this paper.

Damping-Stiffness-Ratio

The system of coupled, damped, driven oscillators described by Eqs. (5.8)-(5.10) has been shown in [82] to allow fast stable convergence of the lattice mass points to their new configuration in a similar application as in this paper. Also in this work we found that setting the damping-stiffness ratio $d/c = 30$ (dimensionless) as in [82] yields stable and efficient computations of mechanical mesh configurations.

Electrical and Mechanical Grids

In [82] we applied a method to validate the mesh coupling of the finite difference mesh and the mechanical mesh via an error norm defined by residues of mass point trajectories what allowed us to find accurate coupling parameters. We found in these validation experiments that the usage of a coarser finite difference mesh compared to the mechanical mesh as shown in Figure 1 in [82] allows accurate computations. Moreover, we found in [82] that our mechanics model converges better with a frequent update rate, and therefore we also choose here to update the mechanical mesh after each solve of the RD system (every $\Delta t = 0.02 \text{ ms}$). We performed a convergence study to determine a suitable value for the threshold of convergence $thr = 0.05 \text{ mN}$ for the mechanical solve for numerical step sizes. For this we halved and quartered the value for thr , and found a convergence of results (occurrence of stretch induced waves, mechanisms for spiral formation, spiral wave dynamics).

Mesh Initial Conditions

The main determinant of cardiac contraction is the $[\text{Ca}^{2+}]_i$ transient, and it is necessary to set initial conditions of the TP06 model so that it describes a steady state Ca^{2+} dynamics of a working cardiac cell. As we aim to study various regimes of wave propagation, which differ substantially from each other, it is necessary to set up proper steady state Ca^{2+} dynamics for each of them. We found that one should carefully approach this problem as establishing of such steady state can take a substantial period of time. To demonstrate this, we performed a numerical experiment on a single, non-deforming cell in which we stimulated it with a frequency 2 Hz by setting $V = 0 \text{ mV}$ for one time step 0.02 ms . We see in Figure 5.1A that it requires a very long time (up to 30 s) to reach steady state values for $[\text{Ca}^{2+}]_i$. Figure 5.1B illustrates the steady state $[\text{Ca}^{2+}]_i$ transient. According to this experiment we use the following initial conditions: $[\text{Ca}^{2+}]_i = 0.11 \text{ }\mu\text{M}$; $[\text{CaSR}] = 3.77 \text{ mM}$; $\text{CaSS} = 0.2 \text{ }\mu\text{M}$. Figure 5.2 shows an electromechanical pulse of a single fiber during isometric contraction. One can see that as in experimental records [112] contraction is slightly delayed from the $[\text{Ca}^{2+}]_i$ transient, and the fiber produces a maximal contractile tension of $\approx 85 \text{ kPa}$ approximately after 100 ms after the upstroke of the action potential.

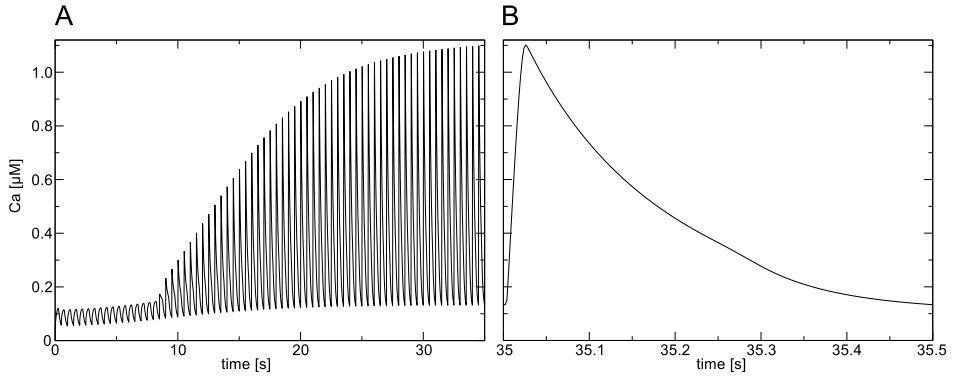


Figure 5.1. Mesh initialization (A) $[Ca^{2+}]_i$ transient during pacing experiment. $[Ca^{2+}]_i$ is shown for a single non-deforming cell undergoing 2 Hz pacing. **(B) Steady state $[Ca^{2+}]_i$ transient.** $[Ca^{2+}]_i$ is shown for a single non-deforming cell after 35 s of 2 Hz pacing.

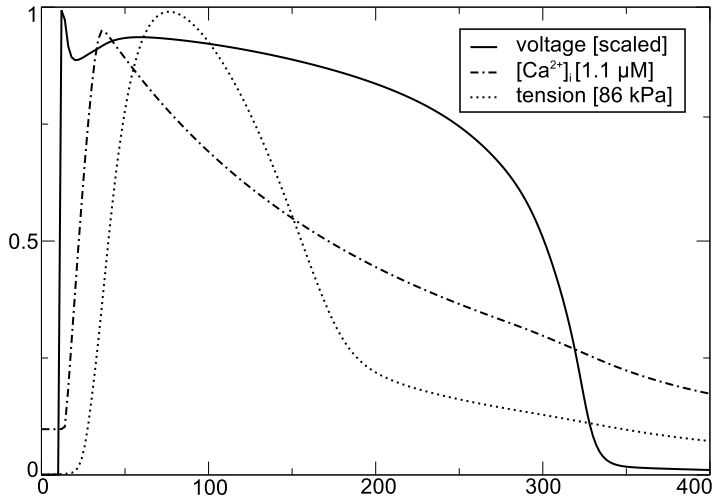


Figure 5.2. Electromechanical activity of an isolated fiber. A pulse is initialized at time 10 ms by setting voltage to 0 mV for 0.02 ms. Fiber is kept at its resting length.

5.3 Results

5.3.1 Effect of Constant Stretch on Action Potential

In the first set of simulations we study the effect of a constant stretch on the action potential of cardiomyocytes. For this we kept a fiber at its maximal fiber

length λ_{max} , and paced it with 1 Hz for 20 s to obtain a steady state dynamics. We applied a constant conductivity G_s for stretch activated current I_{sac} with values from 0 to 25 S/F, and studied how it affects characteristics of the action potential. In Figure 5.3A we show the steady state shape of action potentials for G_s . We see, that the APD increases with increasing G_s . Moreover, we see

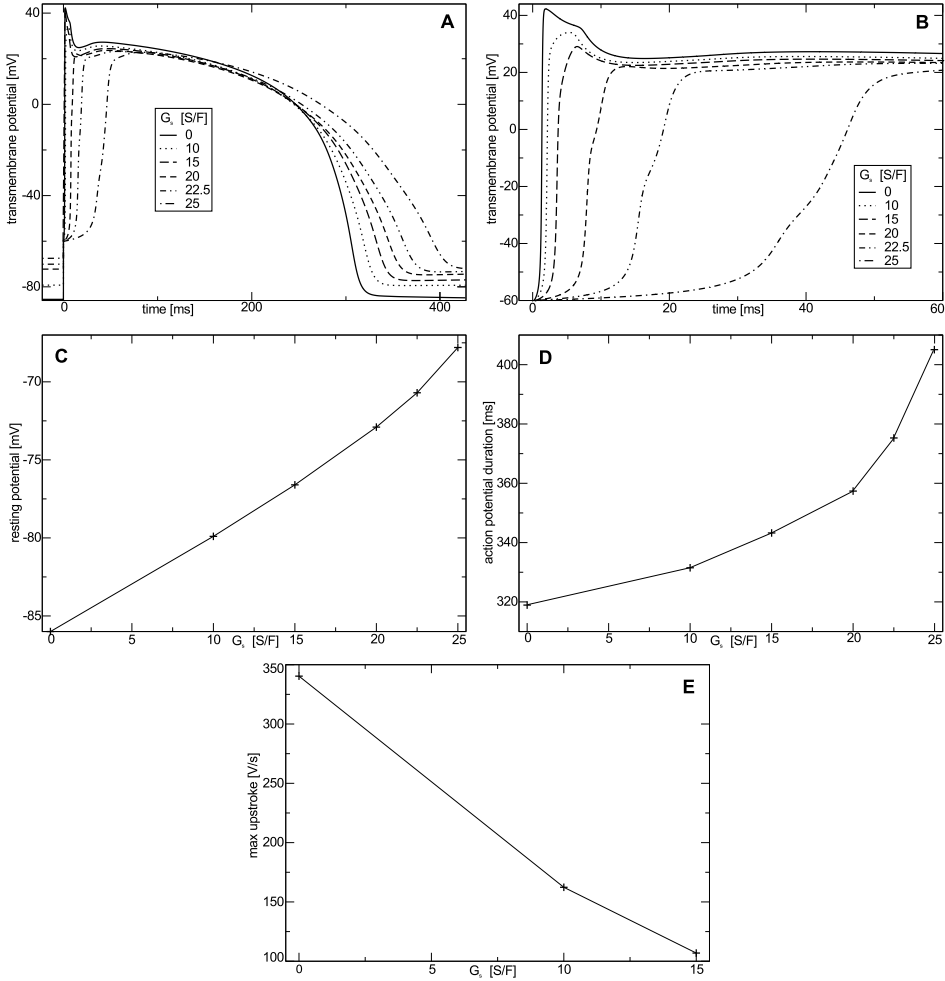


Figure 5.3. Effect of constant maximal stretch on an isolated fiber. (A) Action potential vs G_s . **(B)** Upstroke of action potential vs G_s . **(C)** Resting membrane potential vs G_s . **(D)** APD vs G_s . **(E)** Maximal upstroke slope vs G_s . Fiber was kept at maximal relative length (λ_{max}), and paced at 1 Hz to steady state dynamics.

that the upstroke peak and magnitude decreases with increasing G_s , and that for G_s larger than 15 S/F no typical fast-sodium driven upstroke takes place (see

Figure 5.3B). In Figure 5.3E the upstroke slope is shown as a function of G_s for values smaller than $20 S/F$.

We can explain these effects as a result of two phenomena. First, an increase in APD occurs due to an increase of inward depolarizing current I_{sac} , which causes a longer repolarization process. Second, the effect of the decrease in upstroke slope is caused by a depletion of fast sodium channels via the accommodation phenomenon, a decrease of opening probability of fast sodium channels with a small depolarizing current [18]. In Figure 5.3C we illustrate the effect of I_{sac} on the resting potential of the cell. We can see that the depolarizing I_{sac} increases the resting potential of a cell, which in turn causes accommodation of the fast sodium channels. Moreover, Figure 5.3D illustrates the dependency of APD against G_s , where we also see a linear dependency, and for $G_s = 22.5 S/F$ a steeper slope.

5.3.2 Action Potential and Conduction Velocity Restitution

Next, we show results of a study on the effect of stretch activated currents on restitution properties. To measure restitution properties by external stimulation we periodically initiate traveling waves in a $20\text{ cm} \times 20\text{ cm}$ medium and measure steady state conduction velocity and APD against the frequency of the stimulation. This experiment is performed for conductivities of G_s in a range of $[0; 50] S/F$. The results of this study are illustrated in Figure 5.4. We can see from Figure 5.4A that an increase in G_s lowers the APD; however, does not affect the slope of the restitution curve much. Note, that shortening of APD at low frequency with increase of G_s contradicts results of our simulations for APD in a single cell shown in Figure 5.3A,D, where we showed that APD increases with increase of G_s . However, these differences can be explained by different conditions of the numerical experiments. This is illustrated in Fig 5.5, where we show the shape of action potential, stretch activated current, and deformation of the medium for a single cell which is subject to a constant stretch (as in Figure 5.3), and for a cell in a contracting medium, in which we measured the APD restitution shown in Figure 5.4. We see that I_{sac} in a constantly stretched cell is active during the entire action potential, and has a substantial negative value at the waveback, which results in APD prolongation. Yet, in contrast, for a cell in the contracting medium this negative current at the waveback is absent, as during that phase the cell is not stretched, but is contracting, and thus no stretch activated current is produced. As a result of that difference, the APD for cell in tissue is shorter than that in a cell under constant stretch. Some shortening of APD at increased G_s in that case occurs mainly because negative current prior/during the upstroke of the action potential, which decreases sodium current via the accommodation phenomenon.

Figure 5.4B shows the CV restitution. One can see, that for a stimulation period longer than 2 s stretch activated currents do not affect CV much, because there is no influence of the preceding wave (length of medium 20 cm , and $CV \approx 60\text{ cm/s}$,

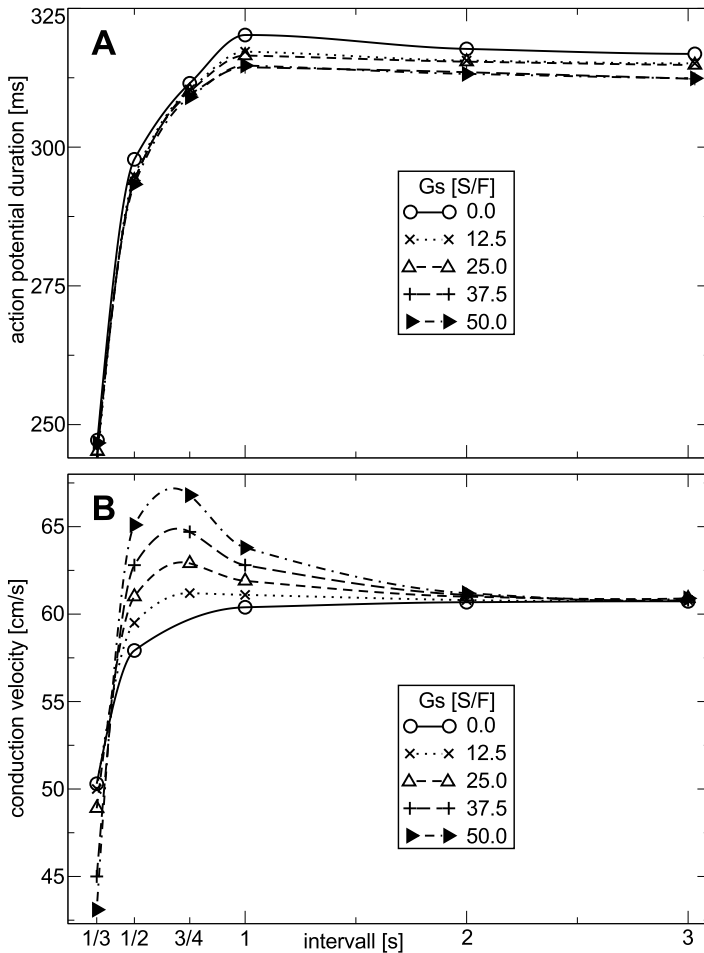


Figure 5.4. Dependence of restitution on stretch-activated currents. (A) APD restitution vs G_s . (AB) CV restitution vs G_s .

thus propagation time is about $1/3$ s). Yet, for stimulation intervals between 1 s and 2 s at higher values of G_s we see slightly negative CV restitution slopes: a higher periodic stimulation causes higher wave velocities. We see that this effect is most pronounced for $G_s = 50$ S/F. This can be understood from the depolarizing effect of I_{sac} , which can increase the potential of a cell and thus bring it closer to its threshold value and increases the wave velocity. For stimulation periods shorter than 0.5 s however, a steep positive CV restitution is present for all measured values of G_s , and the slope of the CV curve increases when G_s is larger.

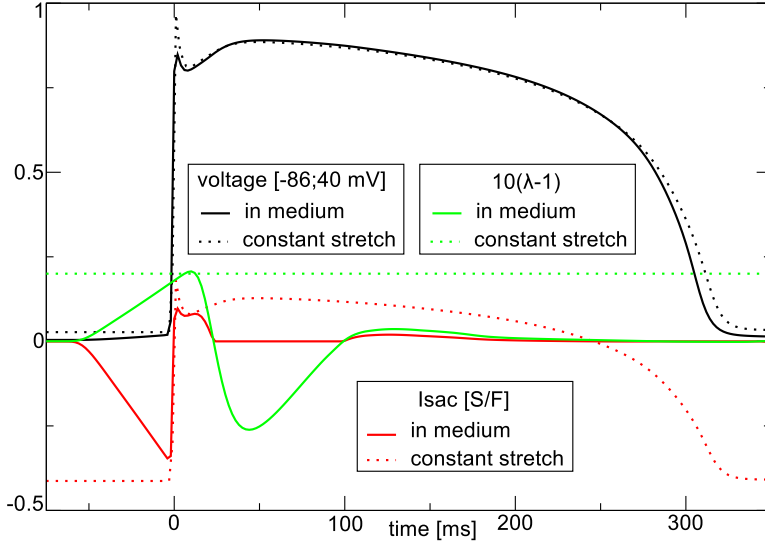


Figure 5.5. Comparison of constantly stretched cell and cell in medium. Continuous lines show variables for cell in the medium, dotted lines show variables for constantly stretched cell. A cell was constantly stretched to 20% of λ_{max} , another cell was in the medium of the restitution experiment illustrated in Figure 5.4. Cells were paced at 1 Hz to steady state dynamics. $G_s = 25 S/F$.

5.3.3 Spiral Wave Dynamics

Here, we study how stretch activated currents effect the dynamics of spiral waves. For this we performed the following simulations. We use a $10\text{ cm} \times 10\text{ cm}$ medium, apply integration steps $\Delta x = \Delta y = 0.025\text{ cm}$ to assure higher spatial resolution, and use $thr = 0.05\text{ mN}$. In this medium we initiate a spiral wave with an S1-S2 protocol, and simulate spiral rotation for 10 s to avoid artifacts from the spiral initiation protocol. During this initial phase $G_s = 0\text{ S/F}$. The values of all variables are then recorded and used as initial conditions for further 2D simulations. We set G_s to various values and study how it affects dynamics of spiral wave. This experiment is performed for conductivities of G_s in a range of $[0; 20]\text{ S/F}$. Figure 5.6 shows an example of spiral rotation in the model for $G_s = 10\text{ S/F}$. Figure 5.7 shows details of tip trajectories of the spirals for different values of G_s . We see that in absence of I_{sac} the spiral rotates around a circular core, however

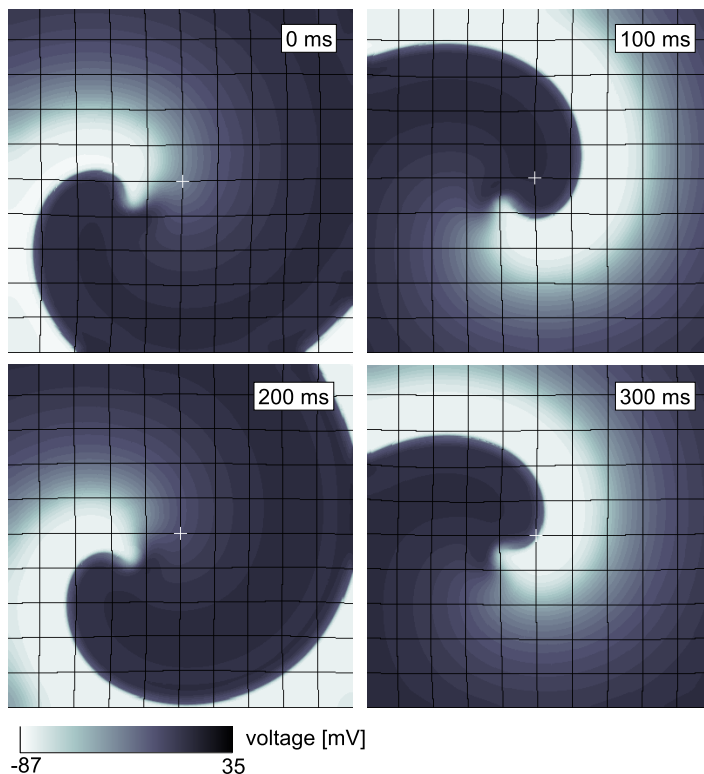


Figure 5.6. Illustration of spiral wave dynamics. Time after stretch activated current I_{sac} was activated is shown in the upper, left of each subfigure. $G_s = 10 S/F$.

with increasing strength of G_s the dynamics of rotation substantially changes. First we see that instead of stationary rotation the spiral starts to drift, and drift velocity increases with an increase of G_s . All simulations in Figure 5.7 were performed for the same time interval, and we see that the distance traveled by the spiral tip increases substantially with an increase of G_s . Figure 5.8A shows the velocity of spiral wave drift as a function of G_s . We see an almost linear increase in drift velocity with increase of G_s .

We have also studied how the period of a spiral wave is affected by stretch-activated currents (see Figure 5.8B). We see that higher G_s increase the spiral wave period. The effects we observe here can again be explained with the accommodation phenomenon. In fact, stretch decreases sodium current which results in some decrease of excitability which is known to increase the period and core of a spiral wave. In Fig.5.8C we show, that indeed larger G_s increases the spiral wave core. Note, that we measured the radius of the spiral core after correcting the spiral tip position data for the drift of the core.

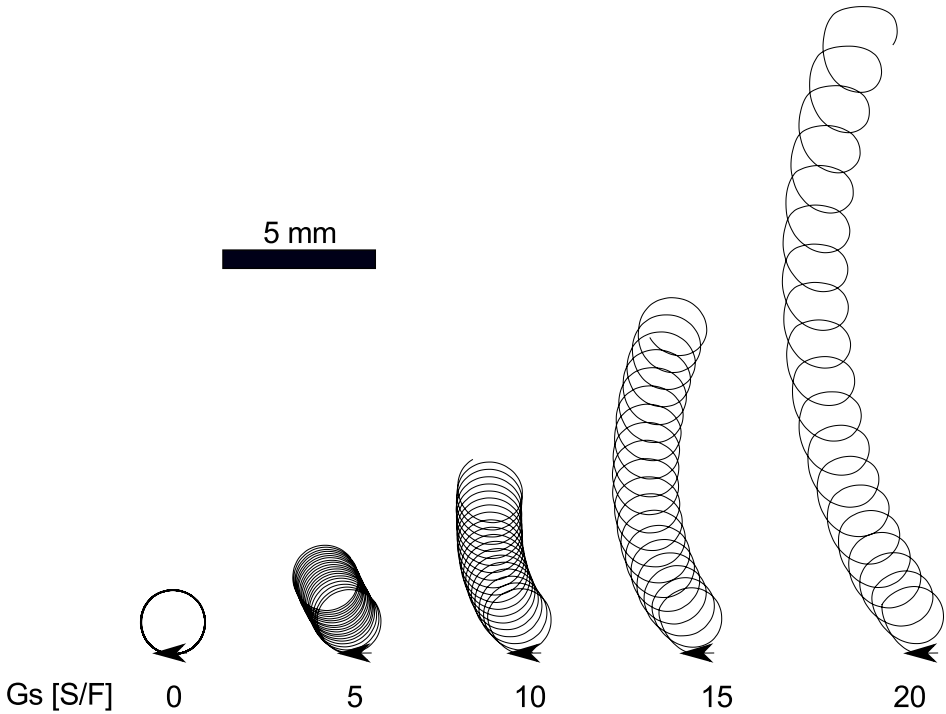


Figure 5.7. Dependence of spiral wave dynamics on stretch-activated currents. Spiral tip trajectories are shown for different values of G_s . Each tip trajectory illustrates drift for 4.434 s. Starting points and drift directions are illustrated with arrows.

5.3.4 Spiral Wave Initiation in a Medium with Complex Geometry

We illustrate our model further by a study of wave deflection at an obstacle in cardiac tissue. This system with a complex geometry was studied before without taking tissue deformation into account [85], and with tissue deformation in [91]. In our study in [91] we found in a low-dimensional electromechanical model, that such a wave deflection can cause abnormal sources of excitation, pacemakers and spiral waves. Here, we choose a very similar setup as in [91], however use a more biophysical description here. We use a medium of size $30\text{ cm} \times 30\text{ cm}$, and the nonconducting obstacle has a stiffness ten times as large as the bulk medium.

Typical results of these simulations are shown in Figure 5.9 and in a movie in the supplemental material.¹ The wave is initiated by a stimulation at the boundary

¹See <http://bioinformatics.bio.uu.nl/danielw/thesis/supplemental/5th-chapter/> for movie on spiral wave initiation in a medium with complex geometry.

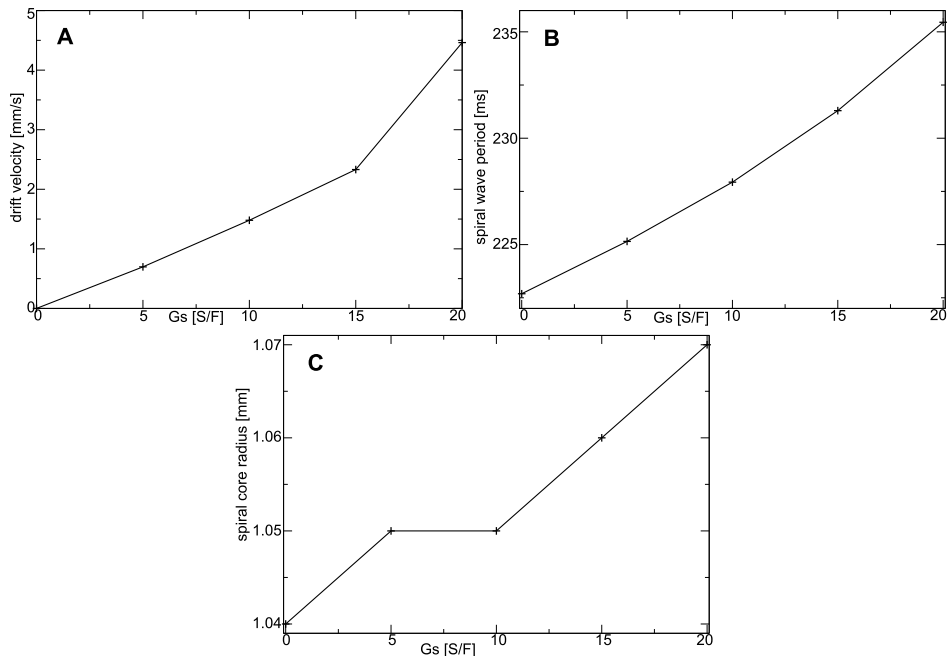


Figure 5.8. Dependence of spiral wave period, drift velocity, and core size on stretch-activated currents. (A) Spiral wave drift velocity as function of G_s . (B) Spiral wave period as function of G_s . (C) Spiral wave core radius as function of G_s .

of the medium above the obstacle. The wave propagates and curls around the obstacle. We see that stretch significantly affects its propagation: we see a preexcitation of the medium before the wave, which increases the local wave velocity [Figure 5.9A] at right boundary, and a similar effect at the bottom boundary. Next, we see the formation of a new wave in a region above the obstacle and the border [Figure 5.9B]. Note, that this phenomenon is similar to the simulations shown in [91], where also a wave is deflected at a non-conducting obstacle, and also stretch-induced wave responses follow a single wave initiation. In the course of time, several wave responses occur by the same mechanism. We also see the formation of a spiral wave in Figure 5.9C due to a local wave break. Note, that this break occurs due to large stretch which causes accommodation of the medium. Figures 5.9D-H show complex dynamics of wave breaks in the medium which is qualitatively similar to the simulations in [91].

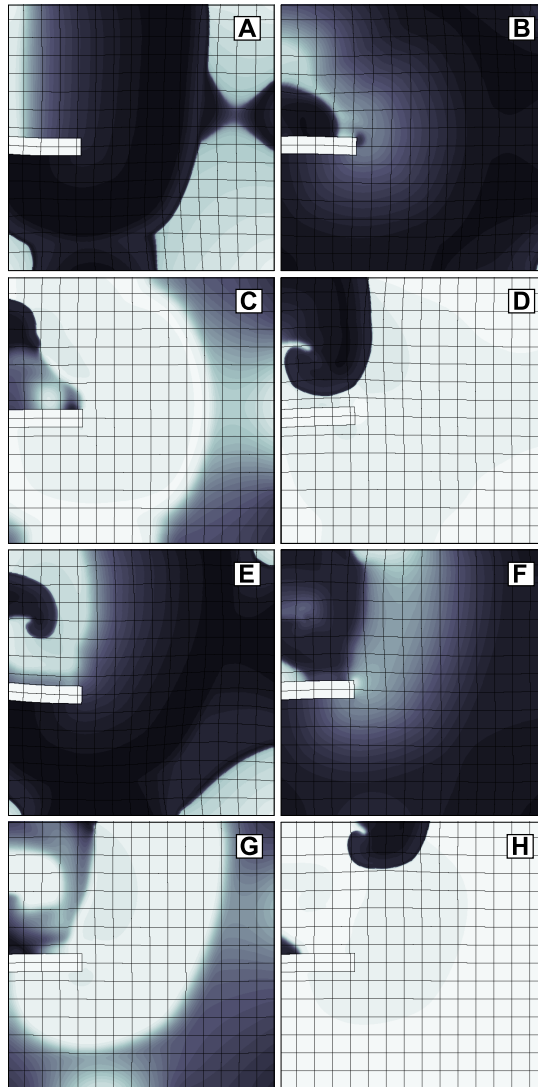


Figure 5.9. Spiral wave activity in a medium with complex geometry (A) Mechanically caused supernormal wave velocity and preexcitation (at time 346 *ms* after external wave initiation). (B) Wave initiation near obstacle and border due to stretch at time 1540 *ms*. (C) Wave break due to accommodation (at time 1894 *ms*). (E) Spiral wave after wave break (at time 2170 *ms*). (F) Spiral wave (at time 2300 *ms*). (G) Spiral breaks (at time 2418 *ms*). (H) Spiral wave after spiral wave break (at time 2550 *ms*). Transmembrane potential is color coded as in Figure 5.6.

5.4 Discussion

In this paper we develop an electromechanical model of the human heart which couples a biophysical model of cardiac excitation [19, 27] and tension development [36, 44] with a discrete elastic mass-lattice model. We illustrate this model in 1D and 2D simulations, and show that it is a valuable tool to study electromechanical effects. The next step is to apply this model to study mechanisms of spiral wave initiation in homogeneous and heterogeneous medium studied in low-dimensional models [91, 106], and find out if they can also be reproduced in the detailed ionic model.

Compared to a finite-element implementation of the Panfilov-Keldermann-Nash (PKN) model used in [43], our mechanical model scales linearly against the number of mechanical nodes, which allows to solve the model with a higher density mechanical nodes and thus high spatial resolution of I_{sac} (see [91]). Furthermore, our model updates the mechanical configuration after each electrical step (0.02 ms); whereas, continuous mechanical studies on cardiac function normally solve mechanics following several electrical steps, for example 100 electrical steps in [65]). Furthermore, our mechanical model is easier to implement than finite element techniques, which makes it an interesting model for many researchers.

However, a drawback of the mass-lattice framework is that it is difficult to reproduce passive mechanical properties of biological tissue with a discrete mechanical model, for example volume conservation or specific passive mechanical properties such as hyperelasticity. In contrast, these properties can be directly described in constitutive relations in continuum mechanics. Note, we aim in this paper not at engineering a realistic model of cardiac tissue, but use a generic material Seth material relation to describe passive mechanical properties, which we however model with state-of-the-art models together with the description of contractile force development. In the area of modeling the passive elasticity of the heart the most established method is to use hyperelastic constitutive relations in finite element formulations of continuum mechanics, for example the Guccione material relation in [65]. Our model can be extended to describe hyperelastic material relations, for example using the approach developed by Fritz et al. in [58], where a mass-spring model is in fact adapted to a hyperelastic material relation to describe cardiac mechanics.

Another important direction would be to extend the model to 3D and the whole heart. Note, that also volume conservation and anisotropy of the heart tissue can be reproduced using engineering techniques [56, 57].

The effect of deformation of the medium on the metric tensor are neglected here, as the main resistivity between cells is constituted by gap junctions. We also

use this assumption in [82] where we studied mechanically caused pacemaking activity in a low-dimensional model where we studied the influence of the change of the metric tensor. We found that the effect of the change in the metric also did not affect the qualitative results of this study on pacemaking activity.

5.5 Acknowledgements

The authors are grateful to Dr. Rikkert H. Keldermann, Dr. Martyn Nash and Dr. Kirsten ten Tusscher for valuable discussions. We thank Jan Kees van Amerongen for excellent technical support.

Chapter 6

Summarizing Discussion

The main aim of this thesis is the development of a new modeling framework: mechanically discrete reaction-diffusion mechanics (dRDM) modeling, and to apply it to study mechanisms of the onset of cardiac arrhythmia. A generic dRDM model is developed in chapter 2 of this thesis, and is applied to study mechanisms of the onset of arrhythmia in chapters 3 and 4. In chapter 5 the mechanically discrete RDM approach is extended to develop a biophysically detailed model for cardiac tissue. Using the discrete mechanical modeling approach we find mechanisms of mechanically caused spiral wave activity in homogeneous and inhomogeneous RDM systems which highlights the importance of mechanical determinants for the onset of cardiac arrhythmia.

The results of the previous chapters will be reviewed in this final chapter; next we will discuss the complexity and limitations of our models; and then a final conclusion will end this thesis.

6.1 A Short Review

In chapter 2 we develop a generic discrete RDM (dRDM) model which couples a low-dimensional model for cardiac excitation and contraction to a discrete mechanical model. We chose a discrete mechanical description, as it might be more appropriate to describe the micro-structure of cardiac tissue, but also because it is computationally efficient and easy to implement. Note, that discrete mechanical models are widely used in various disciplines such as computer graphics [54], medical tissue visualization [55], tribology (the science of friction) [76], and also

in the engineering of elastic models of the heart [57–59]. Our discrete mechanical model directly couples electrical and mechanical processes, and adds a description of stretch-activated currents as the main component of the mechano-electrical feedback phenomenon. In this chapter, we set up the dRDM model with an efficient numerical scheme using Verlet integration for the mechanical equations and an explicit Euler method for RD equations, and we validate its parameter setting. As a demonstration of the high computational performance of the dRDM method we compare it to a continuous mechanical RDM model [43], and we find that the computation time of the dRDM model scales linearly with the number of mechanical nodes, whereas a finite element implementation of [43] scales quadratically. This allows us to use dRDM for large system sizes and high spatial resolution. Furthermore, the numerical scheme allows a frequent update of the mechanical configuration, thus the coupled electrical and mechanical processes can be computed with high temporal resolution. We also show that dRDM reproduces results on pacemaking activity previously found with a RDM model that uses a continuous mechanical description in Ref. [43]. The high numerical resolution allows us to study mechanisms of pacemaker drift, where we find that the curvature of wavefronts cause gradients in the stretch distribution that can cause a drift of a pacemaker.

As a next step, in chapter 3 we apply the dRDM approach to study an important concept in the onset of cardiac arrhythmia, the vulnerability against spiral wave initiation. In a classical protocol to initiate spirals due to vulnerability two consecutive stimuli are applied, and if the time between these stimuli (coupling interval) is in a certain interval called the vulnerable window it can produce spiral wave activity [71]. Spiral wave initiation due to this classical vulnerability is one of the most important concepts in cardiology which explains mechanisms of the onset of various cardiac arrhythmias. The aim of this chapter was to study if and how mechano-electrical feedback may have an influence on vulnerability. We find that deformation not only alters the classical vulnerable zone, but also causes a new mechanism for spiral wave formation at longer coupling intervals. Interestingly, spirals which form via this mechanism have a rotation direction opposite to spirals initiated by the classical vulnerability. We also show that this mechanism naturally occurs in the presence of stretch gradients generated by curved excitation waves.

In chapter 4 we apply the dRDM model to study the effect of mechanical heterogeneity in cardiac tissue for the onset of heart arrhythmias. Heterogeneity is a well known risk factor for the onset of cardiac arrhythmia. Previous modeling studies showed that heterogeneity in electrophysiological properties of cardiac tissue can cause spiral waves [5, 92–94]. However, effects of tissue heterogeneity have mainly been studied without taking deformation into account, even though it is known that cardiac diseases often cause mechanical alterations in cardiac tissue [95, 96]. In addition, abnormal mechanical activity has been observed in chronic cardiac disease [113, 114]. We perform a detailed study of effects of

heterogeneity in passive and active mechanical properties of cardiac tissue, and find that inhomogeneity can cause spiral activity via five possible mechanisms. We classify these mechanisms, and relate them to active and passive mechanical alterations in the inhomogeneity. Interestingly, one of the most abundant mechanisms is abnormal vulnerability which we found earlier in chapter 3. Our results emphasize the relevance of mechanical effects on the onset of cardiac arrhythmia. We use our findings to make predictions on the mechanisms underlying the onset of cardiac arrhythmia during the acute and late stage of myocardial infarction. We make also specific suggestions on experimental setups to test our predictions.

In previous chapters we developed and applied a generic formulation of cardiac tissue which yielded interesting predictions on how mechanical effects may cause cardiac arrhythmia. However, generic models give only a qualitative description of the complex heart function. Therefore, the aim of chapter 5 is to extend our generic description to develop a biophysical model for cardiac tissue to test our predictions and study them further. For this, we use also here the discrete mechanical description, and couple it to state-of-the-art biophysical models of cardiac excitation (Tusscher, Noble, Noble, Panfilov, 2006 model) [19, 27] and contraction (Niederer, Hunter, Smith, 2006 model) [36, 44]. The new electromechanical model for human cardiac tissue combines the advantage of high computational efficiency of the discrete mechanical description and the biophysical complexity of detailed models for excitation and active tension development. We demonstrate the new model approach in an initial set of simulations where we study some effects of deformation on action potential duration and conduction velocity restitution, and the dynamics of spiral waves. Furthermore, we also study wave propagation in a medium with complex geometry which we also used in chapter 3, and find similarities with these results achieved using the generic dRDM model, in particular emergence of spiral waves. The new model proved to be a valuable tool to study cardiac function, and is suitable to test the predictions made in chapter 3 and 4 in more physiologic detail.

6.2 Model Complexity and Limitations

In this thesis, models for cardiac excitability and excitation-contraction coupling of different complexity are used. In chapter 2, a low-dimensional description for cardiac excitability and excitation-contraction coupling is used to develop a generic RDM model (dRDM), and applied in chapters 3 and 4 to study the effect of deformation on mechanisms of spiral wave initiation. The applied modified Aliev-Panfilov-model describes important properties of the cardiac action potential, and the model for development of contractile force captures the most basic property that the active force develops with some delay after the excitation. This generic model does not take individual ionic currents, in particular the complex calcium dynamics into account. However, the advantage of the usage of this generic model

is, that it allows to study basic properties of cardiac excitability with high computational efficiency. Furthermore, the generic dRDM model describes the classical vulnerability phenomenon, and also has a generic description of accommodation. The generic dRDM model was used to identify mechanisms of spiral formation due to deformation in this thesis. This is an adequate choice, as the identification of new mechanisms of spiral wave initiation requires computations over a large parametric space, and it requires high spatiotemporal resolution. Numerical precision is very important in these studies, because some of the phenomena (for example drift in chapter 2) occur in shallow gradients of excitability caused by stretch-activated currents, which needs to be accurately represented in the model. Also, spiral formation due to abnormal vulnerability (studied in chapter 3) occurs only in a small range of stimulation strengths (in the pinwheel experiment) which makes it a challenging problem to find these values.

In chapter 5 the dRDM approach is extended to develop a biophysical, discrete dRDM model for human electromechanical activity. The biophysical model uses the same discrete mechanics formulation and couples it to state-of-the-art models for cardiac excitation and excitation-contraction coupling. We showed that this model can successfully be used to study wave propagation in cardiac tissue, as first initial simulations show interesting results.

The detailed model by itself requires much more differential equations to describe all necessary ionic currents which makes it computationally less efficient than the generic dRDM model. However, here we benefit again from our dRDM approach due to its linear scaling behavior of CPU-time against the number of mechanical nodes. Also with the biophysical model we can make computations within a reasonable time. Moreover, we further improved the computational efficiency by using parallel computations. In case of quadratic scaling, which is normally observed for the FEM models, biophysically accurate modeling becomes a much more challenging problem.

The dRDM models developed in this thesis use a simple two-dimensional geometry of the medium, and do not take fiber anisotropy and electrophysiological inhomogeneity into account. The usage of simple boundary conditions, geometry, and isotropic media are limitations of our studies; however, we wanted to study specific effects without additional complicating factors, and later increase the complexity of our modeling step by step. This allows us to study, and estimate the influence of effects such as geometry and anisotropy on the effects found in our simulations.

The discrete mechanical model used in this thesis is an approximate description of the elastic properties of cardiac tissue, which describes finite deformations in a mass lattice model where springs follow Hooke's deformation law, constituting a so-called Seth material [78]. We, however, do not expect big changes as a result of replacement of this passive mechanical law. Furthermore, in chapter 2, we

show that all effects on pacemaking activity found for more complex non-linear Mooney-Rivlin constitutive relations qualitatively coincide with results achieved with our model. We expect that other constitutive relations may result in some quantitative changes of parameters for the observed effects. This can be studied in more advanced models as a next step.

A practical advantage of the discrete mechanical description applied in this thesis is its computational efficiency. In chapter 2 it is shown that the computation time of the generic dRDM model scales linearly with the number of mechanical nodes of the system. This computational efficiency allows us to compute RDM problems with high numerical resolution. In fact, the dRDM model used in chapter 5 computes the mechanical configuration with the same frequency as the electrophysiological state (every 0.02 *ms*), and computes stretch-activated currents for surface area elements as small as 0.5 *mm* × 0.5 *mm*.

6.3 Future Directions

In this thesis (chapter 3) a new mechanism of spiral wave initiation due to a mechanically caused vulnerable zone is demonstrated. This mechanism is a combination of two processes: first, excitation-contraction coupling causes a supernormal excitability in the back of a wave; second, such a supernormal excitability produces a gradient in excitability which may cause unidirectional wave block which then can lead to the emergence of spiral waves. As next steps it is important to test under which circumstances deformation can lead to supernormal excitability, and to find out conditions when superexcitability can cause spiral waves.

Spiral waves of electrical activity underly arrhythmic malfunctioning of the heart; however, several forms of such tachycardic arrhythmias are a cause of a drift of a spiral wave of electromechanical activity in the heart. It has been shown in a previous study that deformation can induce drift to a spiral wave, however the exact mechanisms behind this phenomenon are not known. Thus, a next important application for our modeling framework is to study the mechanisms of spiral wave drift. A first step was made in this thesis in chapter 5, where the influence of deformation on the spiral wave drift velocity, the shape of the spiral core, and the spiral wave period is studied. Yet, much more work in this direction needs to be done.

The most dangerous cardiac arrhythmia is ventricular fibrillation, a state when many abnormal sources such as spiral waves are present in the heart tissue. The emergence of many spiral sources in the heart can happen when a single spiral wave breaks and thus causes new phase singularities [115, 116]. It has been shown that deformation may cause such a breakup of a spiral wave [60, 65]. However, there is another main effect which so far has mostly been studied as

a pure electrophysiological effect: the mechanism of action-potential restitution instability. In chapter 5 it is shown that deformation affects action potential duration and its restitution via the MEF phenomenon. Therefore, it is important to study the effect of deformation, in particular mechanical heterogeneity on restitution induced breakup of spiral waves with the RDM approach. A first step in this direction was made in chapter 5, where the effect of deformation of the action-potential duration and conduction velocity restitution is studied.

The generic studies of this thesis yielded several mechanisms of spiral initiation in RDM models. The next natural step is to find and test these mechanisms in detailed biophysical models developed in this thesis (chapter 5). Furthermore, these mechanisms should be tested in even more advanced computational models, for example whole heart models, which describe cardiac excitation and deformation with more realistic geometry and boundary conditions, and take the anisotropy and inhomogeneity of cardiac tissue into account.

The most important step to test predictions made in this thesis by performing experiments. For that, experiments on different levels are possible, for example on excised cardiac tissue or cell cultures but also on perfused hearts or even animals. Note that in chapter 4 we proposed possible experimental setups to test our predictions on spiral wave initiation due to mechanical heterogeneity. In particular, we suggested two-dimensional electromechanical experimental systems, such as slices of heart tissue [98] and cell cultures [99] in which ischaemic heterogeneity can for example be mimicked by locally covering the culture with an obstacle [100].

In this thesis, efficient, discrete mechanical modeling is applied to develop RDM models to study the effect of deformation on the onset of heart arrhythmia. However, the modeling formalism may be useful to study other systems in which deformation is coupled to reaction-diffusion processes.

6.4 Conclusion

In this thesis we developed a new modeling framework to study electromechanical systems: mechanically discrete RDM models. These models are numerically efficient, which allows us to solve the coupled electromechanical equations with high spatial and temporal resolution, and they might be extended to describe the underlying cellular structure of cardiac tissue better than continuous mechanical approaches. We first developed and applied a generic discrete RDM model to study mechanisms of spiral wave initiation in homogeneous and heterogeneous cardiac tissue. We found that the important concept of vulnerability is altered by deformation, and even extended by a new mechanically caused vulnerable zone causing a new mechanism of spiral wave generation. Moreover, this mechanically

induced vulnerability is shown to be a main mechanism which produces spiral wave self-generation. We also found that mechanical heterogeneity can cause spiral wave activity via five mechanisms. We related mechanical alterations of an inhomogeneity to emergent regimes of spiral formation and used these results to make predictions on the onset of arrhythmia in acute and chronic infarctious heart conditions, and proposed experiments to test these predictions. As a next step, we developed a biophysical model for human cardiac tissue which couples numerically efficient discrete mechanics modeling with detailed biophysical models of cardiac excitation and contraction. This model updates the electrical and mechanical configuration every 0.02 ms , and the smallest area elements in the mesh that we so far used to calculate stretch-activated currents are $0.5\text{ mm} \times 0.5\text{ mm}$, which makes it to our knowledge the closest coupled biophysical electromechanical model of cardiac tissue. Using this model we found promising results on emerging spiral wave formation in a medium with complex geometry.

Bibliography

- [1] Pool, R. 1990. Heart like a wheel. *Science* 247:1294. (Cited on pages 1, 79, 117, and 119.)
- [2] Winfree, A. T. 1989. Electrical instability in cardiac muscle: Phase singularities and rotors. *J.Theor. Biol.* 138:353. (Cited on pages 1, 52, 71, 79, 117, and 119.)
- [3] Davidenko, J., Pertsov, A., Salomonsz, R., Baxter, W. and Jalife, J. 1992. Stationary and drifting spiral waves of excitation in isolated cardiac muscle. *Nature* 355:349. (Cited on pages 1, 25, 51, 69, 79, 117, and 119.)
- [4] Pertsov, A., Davidenko, J., Salomontsz, R., Baxter, W. and Jalife, J. 1993. Spiral waves of excitation underlie reentrant activity in isolated cardiac muscle. *Circ. Res.* 72:631. (Cited on pages 1, 79, 117, and 119.)
- [5] Krinsky, V. 1966. Spread of excitation in an inhomogeneous medium (state similar to cardiac fibrillation). *Biofizika* 11:776. (Cited on pages 1, 19, 69, 100, 117, and 119.)
- [6] Agladze, K., Keener, J., Müller, S. and Panfilov, A. 1994. Rotating spiral waves created by geometry. *Science* 264:1746. (Cited on pages 1, 117, and 119.)
- [7] Nash, M. and Panfilov, A. 2004. Electromechanical model of excitable tissue to study reentrant cardiac arrhythmias. *Prog. Biophys. Mol. Biol.* 85:501. (Cited on pages 1, 13, 14, 15, 25, 27, 33, 51, 54, 69, 70, 117, and 119.)
- [8] Franz, M. R., Cima, R., Wang, D., Profitt, D. and Kurz, R. 1992. Electrophysiological effects of myocardial stretch and mechanical determinants of stretch-activated arrhythmias 86:968. (Cited on pages 1, 117, and 119.)
- [9] Kohl, P., Hunter, P. and Noble, D. 1999. Stretch-induced changes in heart rate and rhythm: Clinical observations, experiments and mathematical models. *Prog. Biophys. Molec. Biol.* 71:91. (Cited on pages 1, 12, 16, 25, 30, 51, 54, 69, 70, 79, 84, 117, and 119.)

- [10] Wang, Z., Taylor, L. K., Denney, W. D. and Hansen, D. E. 1994. Initiation of ventricular extrasystoles by myocardial stretch in chronically dilated and failing canine left ventricle. *Circulation* 90(4):2022. (Cited on pages 1, 79, 117, and 119.)
- [11] Zipes, D. P. and Wellens, H. J. J. 1998. Sudden cardiac death. *Circulation* 98(21):2334. (Cited on page 3.)
- [12] Zaikin, A. and Zhabotinsky, A. 1970. Concentration wave propagation in two-dimensional liquid-phase self-oscillating system. *Nature* 225:535. (Cited on pages 3, 25, 51, and 69.)
- [13] Imbihl, R. and Ertl, G. 1995. Oscillatory kinetics in heterogeneous catalysis. *Chem. Rev.* 95:697. (Cited on pages 3, 25, and 51.)
- [14] Gorelova, N. and Bures, J. 1983. Spiral waves of spreading depression in the isolated chicken retina. *J. Neurobiol.* 14:353. (Cited on pages 4, 25, and 51.)
- [15] Gerisch, G. 1965. Stadienspezifische aggregationsmuster bei Dictyostelium discoideum. *Wilhelm Roux' Archiv für Entwicklungsmechanik der Organismen* 156(2):127. (Cited on pages 4, 25, and 51.)
- [16] Murray, J. D., Stanley, E. A. and Brown, D. L. 1986. On the spatial spread of rabies among foxes. *Proceedings of the Royal Society of London. Series B. Biological Sciences* 229(1255):111. (Cited on page 4.)
- [17] Bers, D. 2002. Cardiac excitation-contraction coupling. *Nature* 415:198. (Cited on pages 4, 25, and 51.)
- [18] Hodgkin, A. and Huxley, A. 1952. A quantitative description of membrane current and its application to conduction and excitation in nerve. *J. Physiol.* 117:500. (Cited on pages 4, 5, 6, 12, 58, 72, 80, and 89.)
- [19] Ten Tusscher, K. and Panfilov, A. 2006. Alternans and spiral breakup in a human ventricular tissue model. *Am. J. Physiol. Heart Circ. Physiol.* 291:H1088. (Cited on pages 4, 8, 80, 96, and 101.)
- [20] Noble, D. 1962. A modification of the Hodgkin–Huxley equation applicable to Purkinje fiber action and pacemaker potential. *J. Physiol.* 160:317. (Cited on pages 5 and 8.)
- [21] Armstrong, C. M. and Hille, B. 1998. Voltage-gated ion channels and electrical excitability. *Neuron* 20(3):371. (Cited on page 5.)
- [22] Keener, J. and Sneyd, J., *Mathematical physiology*. Springer-Verlag, New York, Heidelberg, Berlin, 1998. (Cited on pages 5, 7, 8, 10, and 26.)
- [23] FitzHugh, R. 1961. Impulses and physiological states in theoretical models of nerve membrane. *Biophys. J.* 1:445. (Cited on page 7.)
- [24] Nagumo, J. S., Arimoto, S. and Yoshizawa, S. 1962. An active pulse transmission line simulating nerve axon. *Proc. IRE.* 50:2061. (Cited on page 7.)

- [25] Yanagihara, K., Noma, A. and Irisawa, H. 1980. Reconstruction of sinoatrial node pacemaker potential based on the voltage clamp experiments. *The Japanese Journal of Physiology* 30(6):841. (Cited on page 8.)
- [26] Beeler, G. W. and Reuter, H. J. 1977. Reconstruction of the action potential of ventricular myocardial fibers. *J. Physiol.* 268:177. (Cited on page 8.)
- [27] Ten Tusscher, K., Noble, D., Noble, P. and Panfilov, A. 2004. A model for human ventricular tissue. *Am. J. Physiol. Heart Circ. Physiol.* 286:H1573. (Cited on pages 8, 80, 81, 96, and 101.)
- [28] Aliev, R. and Panfilov, A. 1996. A simple two-variable model of cardiac excitation. *Chaos, Solitons and Fractals* 7:293. (Cited on pages 8, 9, 10, 26, 51, 52, and 69.)
- [29] Krinsky, V. and Poroticov, V. 1973. Method for analysis of drug action on muscle and nerve membranes from voltage clamp data (nullclines method). *Studia Biophys.* 39(2):69. (Cited on page 9.)
- [30] Labeit, S. and Kolmerer, B. 1995. Titins: Giant proteins in charge of muscle ultrastructure and elasticity. *Science* 270(5234):293. (Cited on page 11.)
- [31] Granzier, H., Kellermayer, M., Helmes, M. and Trombitás, K. 1997. Titin elasticity and mechanism of passive force development in rat cardiac myocytes probed by thin-filament extraction. *Biophysical Journal* 73(4):2043. (Cited on page 11.)
- [32] Huxley, A. F. and Niedergerke, R. 1954. Structural changes in muscle during contraction: Interference microscopy of living muscle fibres. *Nature* 173(4412):971. (Cited on page 11.)
- [33] Huxley, H. and Hanson, J. 1954. Changes in the Cross-Striations of muscle during contraction and stretch and their structural interpretation. *Nature* 173(4412):973. (Cited on page 11.)
- [34] Hanson, J. and Huxley, H. 1957. Quantitative studies on the structure of cross-striated myofibrils: II. investigations by biochemical techniques. *Biochimica et Biophysica Acta* 23(0):250. (Cited on page 11.)
- [35] Bassani, J. W., Bassani, R. A. and Bers, D. M. 1994. Relaxation in rabbit and rat cardiac cells: species-dependent differences in cellular mechanisms. *The Journal of physiology* 476(2):279. (Cited on page 12.)
- [36] Niederer, S., Hunter, P. and Smith, N. 2006. A quantitative analysis of cardiac myocyte relaxation: a simulation study. *Biophys. J.* 90(5):1697. (Cited on pages 12, 14, 80, 81, 82, 96, and 101.)
- [37] Keldermann, R., Nash, M. and A.V., P. 2009. Modeling cardiac mechano-electrical feedback using reaction-diffusion-mechanics systems. *Physica D* 238:1000. (Cited on page 12.)
- [38] Franz, M. R. 1996. Mechano-electrical feedback in ventricular myocar-

- dium. *Cardiovascular Research* 32(1):15 . (Cited on page 12.)
- [39] Hill, A. V. 1936. Excitation and accommodation in nerve. *Proceedings of the Royal Society of London. Series B, Biological Sciences* 119(814):305. (Cited on page 12.)
- [40] Allen, D. and Kentish, J. 1985. The cellular basis of the length-tension relation in cardiac muscle. *Journal of Molecular and Cellular Cardiology* 17(9):821 . (Cited on page 12.)
- [41] Kohl, P. and Sachs, F. 2001. Mechanoelectric feedback in cardiac cells. *Philosophical Transactions of the Royal Society of London. Series A: Mathematical, Physical and Engineering Sciences* 359(1783):1173. (Cited on page 13.)
- [42] Trayanova, N. A., Constantino, J. and Gurev, V. 2011. Electromechanical models of the ventricles. *American journal of physiology. Heart and circulatory physiology* 301(2):H279. (Cited on page 13.)
- [43] Panfilov, A., Keldermann, R. and Nash, M. 2005. Self-organized pacemakers in a coupled reaction-diffusion-mechanics system. *Phys. Rev. Lett.* 95(25)(25):258104. (Cited on pages 14, 15, 16, 17, 21, 25, 26, 27, 31, 32, 33, 36, 37, 38, 39, 40, 41, 46, 48, 51, 52, 54, 55, 60, 69, 70, 71, 73, 79, 81, 84, 85, 96, and 100.)
- [44] Niederer, S. and Smith, N. 2008. An improved numerical method for strong coupling of excitation and contraction models in the heart. *Prog. Biophys. Mol. Biol.* 96(1-3):90. (Cited on pages 14, 80, 81, 82, 83, 84, 96, and 101.)
- [45] LeGrice, I., Hunter, P. and Smail, B. 1995. Laminar structure of the heart. II. Mathematical model. *Am. J. Physiol.* 269:H571. (Cited on pages 14 and 25.)
- [46] Nash, M. and Hunter, P. 2000. Computational mechanics of the heart: from tissue structure to ventricular function. *J. Elasticity* 61:113. (Cited on pages 14 and 25.)
- [47] Nordsletten, D., Niederer, S., Nash, M., Hunter, P. and Smith, N. 2011. Coupling multi-physics models to cardiac mechanics. *Progress in Biophysics and Molecular Biology* 104(13):77. (Cited on page 14.)
- [48] Lautrup, B., *Physics of Continuous Matter: Exotic and Everyday Phenomena in the Macroscopic World*. Taylor & Francis, "Abingdon, Oxford, UK", 2004, 1 edn. (Cited on page 15.)
- [49] Malvern, L., *Introduction to the Mechanics of a Continuous Medium*. Prentice Hall, Englewood Cliffs, 1969. (Cited on page 15.)
- [50] Hunter, P., Nash, M. and Sands, G., *Computational Electromechanics of the Heart*. In A. Panfilov and A. Holden, eds., *Computational Biology of the Heart*, Wiley, Chichester, United Kingdom, 1997, 345–407. (Cited on page 15.)

- [51] Bestehorn, M. and Busse, F., Hydrodynamik und Strukturbildung: Mit einer kurzen Einführung in die Kontinuumsmechanik. Springer-Lehrbuch, Springer, New York, Heidelberg, Berlin, 2006. (Cited on page 15.)
- [52] Popov, V. and S.G., P. 2001. Theoretical principles of modelling elastoplastic media by moveable cellular automata method. i: Homogenous media. *Phys Mesomechanics* 4:15. (Cited on pages 16, 25, and 47.)
- [53] Ostermeyer, G. and Popov, V. 1999. Many-particle non equilibrium interaction potentials in the mesoparticle method. *Phys Mesomechanics* 2(6):31. (Cited on pages 16, 25, and 47.)
- [54] Nealen, A., Müller, M., Keiser, R., Boxermann, E. and M., C. 2006. Physically based deformable models in computer graphics. *Computer Graphics Forum* 25:809. (Cited on pages 16, 25, 47, and 99.)
- [55] Delingette, H. 1998. Towards realistic soft-tissue modelling in medical simulation. *Proceedings of the IEEE* 86(3):512. (Cited on pages 16, 25, and 99.)
- [56] Bourguignon, D. and Cani, M.-P., Controlling anisotropy in mass-spring systems. In Eurographics Workshop on Computer Animation and Simulation (EGCAS), Springer-Verlag, New York, Heidelberg, Berlin, 2000, Springer Computer Science, 113–123, proceedings of the 11th Eurographics Workshop, Interlaken, Switzerland, August 21–22, 2000. (Cited on pages 16, 25, 47, and 96.)
- [57] Mohr, M., Seemann, G., Sachse, F. and Dössel, O. 2003. Modeling of myocardial deformation with an extended spring mass system. *Biomedical Engineering* 48(1):6. (Cited on pages 16, 25, 47, 96, and 100.)
- [58] Fritz, T., Jarrousse, O. and Dössel, O., Adapting a mass-spring system to energy density function describing myocardial mechanics. In J. Vander Sloten, P. Verdonck, M. Nyssen and H. J., eds., 4th European Conference of the International Federation for Medical and Biological Engineering, Springer, Berlin, Heidelberg, 2009, 2003–2006. (Cited on pages 16, 25, 47, 96, and 100.)
- [59] Caillerie, D., Mourad, A. and Raoult, A. 2003. Cell-to-muscle homogenization. application to a constitutive law for the myocardium. *Math. Model. Numer. Anal.* 37:681. (Cited on pages 16, 47, and 100.)
- [60] Panfilov, A., Keldermann, R. and Nash, M. 2007. Drift and breakup of spiral waves in reaction-diffusion-mechanics systems. *Proc. Natl. Acad. Sci. U.S.A.* 104(19):7922. (Cited on pages 16, 17, 25, 31, 32, 51, 54, 55, 58, 69, 70, 71, 73, 79, 84, 85, and 103.)
- [61] Hu, H. and Sachs, F. 1997. Stretch-activated ion channels in the heart. *J Mol Cell Cardiol.* 29:1511. (Cited on pages 17, 30, 54, and 84.)
- [62] Zhang, Y., Youm, J., Sung, H., Lee, S., Ryu, S., Ho, W. and Earm, Y. 2000. Stretch-activated and background non-selective cation channels in rat at-

- rial myocytes. *J. Physiol.* 523:607. (Cited on pages 17, 30, 54, and 84.)
- [63] Vetter, F. and McCulloch, A. 2001. Mechanoelectric feedback in a model of the passively inflated left ventricle. *Ann Biomed Eng.* 29:414. (Cited on pages 17, 31, and 84.)
- [64] Trayanova, N., Li, W., Eason, J. and Kohl, P. 2004. Effect of stretch activated channels on defibrillation efficacy. *Heart Rhythm* 1:67. (Cited on pages 17, 31, and 84.)
- [65] Keldermann, R. H., Nash, M. P., Gelderblom, H., Wang, V. Y. and Panfilov, A. V. 2010. Electromechanical wavebreak in a model of the human left ventricle. *Am J Physiol Heart Circ Physiol* 299(1):H134. (Cited on pages 17, 73, 79, 81, 84, 85, 96, and 103.)
- [66] Jie, X., Gurev, V. and Trayanova, N. 2010. Mechanisms of mechanically induced spontaneous arrhythmias in acute regional ischemia. *Circ Res* 106(1):185. (Cited on pages 17, 73, 75, and 79.)
- [67] Panfilov, A. V., Theory of reentry. In D. P. Zipes and J. Jalife, eds., *Cardiac electrophysiology. From cell to bedside*, 5th edition, Elsevier, New York, 2009, 329–337. (Cited on page 17.)
- [68] Mines, G. R. 1913. On dynamics equilibrium in the heart. *J. Physiol. (London)* 46:349. (Cited on page 17.)
- [69] Wiener, N. and Rosenblueth, A. 1946. The mathematical formulation of the problem of conduction of impulses in a network of connected excitable elements, specifically in cardiac muscle. *Archivos Del Instituto De Cardiología De Mexico* 16(3):205. (Cited on pages 17 and 55.)
- [70] Selfridge, O. 1948. Studies on flutter and fibrillation. Some notes on the theory of flutter. *Arch. Inst. Cardiol. Mex.* 18:177. (Cited on page 18.)
- [71] Starmer, C. F., Biktashev, V. N., Romashko, D. N., Stepanov, M. R., Makarova, O. N. and Krinsky, V. I. 1993. Vulnerability in an excitable medium: Analytical and numerical studies of initiating unidirectional propagation. *Biophys. J.* 65:1775. (Cited on pages 19, 51, 55, and 100.)
- [72] Winfree, A. and Strogatz, S. 1984. Organizing centers for three-dimensional chemical waves. *Nature* 311:611. (Cited on pages 25, 51, and 69.)
- [73] Weijer, C. 2004. Dictyostelium morphogenesis. *Curr Opin Genet Dev.* 14:392. (Cited on pages 25, 51, and 69.)
- [74] Yoshida, R., Takahashi, T., Yamaguchi, T. and Ichijo, H. 1996. Self-oscillating gel. *J. Am. Chem. Soc.* 118:5134. (Cited on pages 25, 51, and 69.)
- [75] Feynman, R., Leighton, R. and Sands, M., Feynman lectures on physics. Addison-Wesley, Massachusetts, New York, 1969. (Cited on page 29.)

- [76] Schargott, M., Popov, V. L. and Heß. 2007. Macroscopic isotropy of two- and three-dimensional elastic lattice models. *Tribology international* 40:937. (Cited on pages 29, 30, 83, and 99.)
- [77] Krivtsov, A. 1999. Constitutive equations of the nonlinear crystal lattice. *Z. angew. Math. Mech.* 79(S2):419. (Cited on pages 30 and 82.)
- [78] Seth, B. 1935. Finite strain in elastic problems. *Phil. Trans. R. Soc. Lond. A* 234:231. (Cited on pages 30, 82, and 102.)
- [79] Verlet, L. 1967. Computer "experiments" on classical fluids. i. thermodynamical properties of lennard-jones molecules. *Phys. Rev.* 159(1):98. (Cited on pages 32, 54, and 84.)
- [80] Panfilov, A. 2002. Spiral breakup in an array of coupled cells: the role of the intercellular conductance. *Phys. Rev. Lett.* 88:118101. (Cited on page 33.)
- [81] Zykov, V. S. 1980. Analytical evaluation of the dependence of the speed of an excitation wave in a two dimensional excitable medium on the curvature of its front. *Biophysics* 25:906. (Cited on page 42.)
- [82] Weise, L. D., Nash, M. P. and Panfilov, A. V. 2011. A discrete model to study reaction-diffusion-mechanics systems. *PLoS ONE* 6(7):e21934. (Cited on pages 51, 52, 53, 54, 55, 60, 61, 64, 69, 70, 71, 81, 82, 83, 85, 86, and 97.)
- [83] Winfree, A., *When time breaks down: The Three-Dimensional Dynamics of Electrochemical Waves and Cardiac Arrhythmias*. Princeton University Press, New York, USA, 1987. (Cited on page 52.)
- [84] Hill, A. 1936. Excitation and accommodation in nerve. *Proc. R. Soc. Lond.* 119:305. (Cited on pages 58 and 72.)
- [85] Panfilov, A. and Pertsov, A. 1982. Mechanism of spiral waves initiation in active media connected with critical curvature phenomenon. *Biofizika* 27:886, in Russian. (Cited on pages 61 and 93.)
- [86] Pertsov, A. M., Panfilov, A. V. and Medvedeva, F. U. 1983. [Instabilities of autowaves in excitable media associated with critical curvature phenomena]. *Biofizika* 28(1):100, PMID: 6830879. (Cited on page 61.)
- [87] Cabo, C., Pertsov, A. M., Baxter, W. T., Davidenko, J. M., Gray, R. A. and Jalife, J. 1994. Wave-front curvature as a cause of slow conduction and block in isolated cardiac muscle. *Circ. Res.* 75:1014. (Cited on page 61.)
- [88] Kamkin, A., Kiseleva, I., Isenberg, G., Wagner, K. D., GÄ $\frac{1}{4}$ nther, J., Theres, H. and Scholz, H. 2003. Cardiac fibroblasts and the mechano-electric feedback mechanism in healthy and diseased hearts. *Progress in biophysics and molecular biology* 82(1-3):111. (Cited on page 64.)
- [89] Hoff, H. and Nahum, L. 1938. The supernormal period in the mammalian ventricle. *Am J Physiol* 124:591. (Cited on page 64.)

- [90] Van Dam, R. T., Durrer, D., Strackee, J. and Vand Der Tweel, L. H. 1956. The excitability cycle of the dog's left ventricle determined by anodal, cathodal, and bipolar stimulation. *Circ Res* 4(2):196. (Cited on page 64.)
- [91] Weise, L. D. and Panfilov, A. V. 2011. New mechanism of spiral wave initiation in a reaction-diffusion-mechanics system. *PLoS ONE* 6(11):e27264. (Cited on pages 69, 70, 71, 73, 79, 81, 83, 85, 93, 94, and 96.)
- [92] Panfilov, A. and Vasiev, B. 1991. Vortex initiation in a heterogeneous excitable medium. *Physica D* 49:107. (Cited on pages 69, 73, and 100.)
- [93] Ten Tusscher, K. and Panfilov, A. 2003. Reentry in heterogeneous cardiac tissue described by the Luo-Rudy ventricular action potential model. *Am. J. Physiol. Heart Circ. Physiol.* 284:H542. (Cited on pages 69 and 100.)
- [94] Moe, G., Rheinbolt, W. and Abildskov, J. 1964. A computer model of atrial fibrillation. *Am. Heart J.* 67:200. (Cited on pages 69 and 100.)
- [95] Tyberg, J., Yeatman, L., Parmley, W., Urschel, C. and Sonnenblick, E. 1970. Effects of hypoxia on mechanics of cardiac contraction. *American Journal of Physiology* 218(6):1780. (Cited on pages 75 and 100.)
- [96] Vogel, W. M., Apstein, C. S., Briggs, L. L., Gaasch, W. H. and Ahn, J. 1982. Acute alterations in left ventricular diastolic chamber stiffness. role of the "erectile" effect of coronary arterial pressure and flow in normal and damaged hearts. *Circulation Research* 51(4):465, PMID: 7127681. (Cited on pages 75 and 100.)
- [97] Alvarez-Lacalle, E. and Echebarria, B. 2009. Global coupling in excitable media provides a simplified description of mechano-electrical feedback in cardiac tissue. *Physical Review E* 79(3):031921. (Cited on page 76.)
- [98] de Boer, T. P., Camelliti, P., Ravens, U. and Kohl, P. 2009. Myocardial tissue slices: organotypic pseudo-2D models for cardiac research & development. *Future Cardiology* 5(5):425. (Cited on pages 76 and 104.)
- [99] Zhang, Y., Sekar, R. B., McCulloch, A. D. and Tung, L. 2008. Cell cultures as models of cardiac mechano-electric feedback. *Progress in Biophysics and Molecular Biology* 97(2&3):367. (Cited on pages 76 and 104.)
- [100] De Diego, C., Pai, R. K., Chen, F., Xie, L., De Leeuw, J., Weiss, J. N. and Valderrábano, M. 2008. Electrophysiological consequences of acute regional Ischemia/Reperfusion in neonatal rat ventricular myocyte monolayers. *Circulation* 118(23):2330. (Cited on pages 76 and 104.)
- [101] Kohl, P., Nesbitt, A., Cooper, P. and Lei, M. 2001. Sudden cardiac death by commotio cordis: role of mechano-electric feedback. *Cardiovasc. Res.* 50:280. (Cited on page 79.)
- [102] Lab, M. 1982. Contraction-excitation feedback in myocardium. Physiological basis and clinical relevance. *Circ. Res.* 50(6):757. (Cited on page 79.)

- [103] Cave, D. M., Gazmuri, R. J., Otto, C. W., Nadkarni, V. M., Cheng, A., Brooks, S. C., Daya, M., Sutton, R. M., Branson, R. and Hazinski, M. F. 2010. Part 7: CPR techniques and devices 2010 american heart association guidelines for cardiopulmonary resuscitation and emergency cardiovascular care. *Circulation* 122(18 suppl 3):S720. (Cited on page 79.)
- [104] Kohl, P. and Ravens, U., eds., Mechano-Electric Feedback and Cardiac Arrhythmias, Prog. Biophys. Molec. Biol., Elsevier Ltd, 2003, vol. 82(1-3). 1–266. (Cited on page 79.)
- [105] Keldermann, R., Nash, M. and Panfilov, A. 2006. Pacemakers in a reaction diffusion mechanics systems. *J. Stat. Phys.* 128:375. (Cited on page 79.)
- [106] Weise, L. D. and Panfilov, A. V. 2012. Emergence of spiral wave activity in a mechanically heterogeneous reaction-diffusion-mechanics system. *Phys. Rev. Lett.* 108:228104. (Cited on pages 79, 81, and 96.)
- [107] de Tombe, P. P. and Stienen, G. J. M. 2007. Impact of temperature on cross-bridge cycling kinetics in rat myocardium. *The Journal of Physiology* 584(2):591. (Cited on page 81.)
- [108] Webb, A. I. and Weaver, B. M. 1979. The density of equine tissue at 37 degrees c. *Research in Veterinary Science* 26(1):71. (Cited on page 83.)
- [109] Kohl, P., Hunter, P. and Noble, D. 1999. Stretch-induced changes in heart rate and rhythm: clinical observations, experiments and mathematical models. *Progress in Biophysics and Molecular Biology* 71(1):91. (Cited on page 84.)
- [110] Skouibine, K., Trayanova, N. and Moore, P. 2000. A numerically efficient model for simulation of defibrillation in an active bidomain sheet of myocardium. *Math. Biosci.* 166(1):85. (Cited on page 84.)
- [111] Kohl, P., Day, K. and Noble, D. 1998. Cellular mechanisms of cardiac mechano-electric feedback in a mathematical model. *Can. J. Cardiol.* 14(1):111. (Cited on page 84.)
- [112] Vahl, C. F., Timek, T., Bonz, A., Fuchs, H., Dillman, R. and Hagl, S. 1998. Length dependence of calcium- and force-transients in normal and failing human myocardium. *Journal of molecular and cellular cardiology* 30(5):957. (Cited on page 86.)
- [113] Califf, R. M., Burks, J. M., Behar, V. S., Margolis, J. R. and Wagner, G. S. 1978. Relationships among ventricular arrhythmias, coronary artery disease, and angiographic and electrocardiographic indicators of myocardial fibrosis. *Circulation* 57(4):725. (Cited on page 100.)
- [114] Siogas, K., Pappas, S., Graekas, G., Goudevenos, J., Liapi, G. and Sideris, D. 1998. Segmental wall motion abnormalities alter vulnerability to ventricular ectopic beats associated with acute increases in aortic pressure in patients with underlying coronary artery disease. *Heart* 79(3):268. (Cited on

page 100.)

- [115] Panfilov, A. 1998. Spiral breakup as a model of ventricular fibrillation. *Chaos* 8:57. (Cited on page 103.)
- [116] Panfilov, A. and Hogeweg, P. 1995. Mechanisms of cardiac fibrillation. *Science* 270:1223. (Cited on page 103.)

Samenvatting

Aritmie van het hart is een belangrijke doodsoorzaak in geïndustrialiseerde landen [1]. Vaak zijn hartritmestoornissen het gevolg van spiraalvormige elektrische excitatie golven in de hartspier [2–4]. Daarom is het belangrijk de mechanismen achter het ontstaan van dergelijke spiraalgolven te begrijpen.

Belangrijke inzichten in de vormingsmechanismen van hartritmestoornissen zijn verkregen door onderzoek aan spiraalgolven in reactie-diffusie modellen van hartweefsel [5, 6]. In de meeste van deze studies was het hart volkomen immobiel [7], hoewel bekend is dat het werkende hart sterk vervormt en dat vervorming van het hart grote invloed heeft op de voortplanting van elektrische golven [8]. Bijvoorbeeld een klap op de borst kan hartritmestoornissen veroorzaken (“commotio cordis”), maar ook beeïndigen (“precordiale stomp”) [9, 10].

De onderzoeksvraag van dit werk is: “wat is de invloed van de vervorming van het hart op het ontstaan van aritmieën in het hart”. Om deze vraag te beantwoorden zijn reactie-diffusie-mechanica modellen ontwikkeld om mechanismen voor de initiatie van spiraalgolven te onderzoeken.

In hoofdstuk 2 van dit boek is een eenvoudig mechanisch discreet reactie-diffusie mechanica model (dRDM) ontwikkeld. In de hoofdstukken 3 en 4, werd het dRDM model toegepast om de mechanismen voor de vorming van aritmieën te onderzoeken. In hoofdstuk 5 werd het dRDM model uitgebreid tot een biofysisch model van menselijk hartweefsel.

Met deze aanpak van discrete reactie-diffusie mechanisme modellen hebben we nieuwe mechanismen voor het ontstaan van spiraalgolven in homogene en inhomogene media gevonden. De resultaten van deze studie laten zien dat mechanische effecten een grote rol spelen bij het ontstaan van hartritmestoornissen.

Zusammenfassung

Rhythmusstörungen des Herzens sind eine der häufigsten Todesursachen in industrialisierten Ländern [1]. Oftmals resultieren Herzrhythmusstörungen von spiralförmigen elektrischen Erregungswellen im Herzmuskel [2–4]. Deshalb ist es wichtig, die Mechanismen der Initiation solcher Spiralwellen zu verstehen.

Wichtige Erkenntnisse zu Entstehungsmechanismen von Herzrhythmusstörungen wurden durch die Erforschung von Spiralwelleninitiation in Reaktions-Diffusions Modellen für Herzgewebe erzielt [5, 6]. Allerdings wurde in den meisten dieser Studien das Herz als unbeweglich angenommen [7], obwohl es bekannt ist, daß sich das arbeitende Herz stark verformt, und dass Deformation des Herzens großen Einfluss auf die Ausbreitung elektrischer Erregungswellen hat [8]. Beispielsweise ist es bekannt, daß ein Schlag auf die Brust Rhythmusstörungen verursachen (“Commotio cordis”), aber auch beenden kann (“Präkordialer Faustschlag”) [9, 10].

Die Forschungsfrage dieser Arbeit ist: “Welchen Einfluss hat die Deformation des Herzens auf Mechanismen der Erzeugung von Herzrhythmusstörungen?”. Um diese Frage zu erforschen, werden Reaktions-Diffusions-Mechanik Modelle entwickelt und angewendet um Mechanismen zur Initiation von Spiralwellen zu untersuchen.

Im Kapitel 2 dieser Arbeit wird ein einfaches mechanisch diskretes Reaktions-Diffusions-Mechanik-Modell (dRDM) entwickelt. In den Kapiteln 3 und 4 wird das dRDM Modell angewendet um Mechanismen zur Entstehung von Herzrhythmusstörungen zu untersuchen. In Kapitel 5 wird der dRDM Ansatz erweitert um ein biophysikalisches Modell für menschliches Herzgewebe zu entwickeln.

Mit den diskreten Reaktions-Diffusions-Mechanik-Modellen werden neue Mechanismen zur Initiation von Spiralwellen in homogenen und inhomogenen Medien gefunden. Die Ergebnisse dieser Arbeit betonen die Wichtigkeit mechanischer Effekte bei der Entstehung von Herzrhythmusstörungen.

Curriculum Vitæ

The author of this thesis, Louis Daniel Weise, was born on the 22nd of July 1979 in Aalen, Germany. He attended the Schenk-von-Limpurg Gymnasium (highschool) in Gaildorf, Germany (1989-1998), where he obtained his “Abitur” (high school diploma). For his “Zivildienst” (civilian national service) he worked as an emergency medical technician at the Red-Cross in Schwäbisch Hall (1999-2000). He studied one year of chemistry at the University of Ulm, Germany (2000-2001), and continued to study biochemistry at the University of Tübingen (2001-2007). As part of his studies he did an internship for one year (2004-2005) at the Max-Planck-Institute for Biochemistry in Martinsried, Germany. He received his diploma in July 2007, after completing an eight month research project in the theoretical chemistry group of Prof. Dr. Christian Ochsenfeld, developing and applying quantum chemical methods to study dispersive molecular interactions. He continued these studies in the group of Prof. Dr. Christian Ochsenfeld until December 2007 as a research assistant. In May 2008 he started his PhD research on reaction-diffusion-mechanics systems in the Theoretical Biology and Bioinformatics group of the Utrecht University, supervised by Prof. Dr. Alexander V. Panfilov. The results of his PhD research are described in this thesis.

List of Publications

Louis D. Weise, Daniel S. Lambrecht, Bernd Doser, Christian Ochsenfeld Simple Parametrization in Double-Hybrid Density-Functional and Scaled Second-Order Møller-Plesset Perturbation Theory. **in preparation**

Louis D. Weise, Alexander V. Panfilov A Discrete Electromechanical Model for Human Cardiac Tissue. **in preparation**

Louis D. Weise, Alexander V. Panfilov Emergence of Spiral Wave Activity in a Mechanically Heterogeneous Reaction-Diffusion-Mechanics System. *Phys. Rev. Lett.* 108, 228104 (2012)

Louis D. Weise, Alexander V. Panfilov New Mechanism of Spiral Wave Initiation in a Reaction-Diffusion-Mechanics System. *PLoS ONE* 6(11):e27264 (2011)

Louis D. Weise, Martyn P. Nash, Alexander V. Panfilov A Discrete Model to Study Reaction-Diffusion-Mechanics Systems. *PLoS ONE* 6(7):e21934 (2011)

Acknowledgements

At the end of this book I want to thank all the persons that helped me to make this thesis possible.

I want to thank my promoter and supervisor, Sasha Panfilov. Dear Sasha, from the first day of working with you, I was impressed by your catching passion for science and your thoughtful and clear way to explain complicated matters. Thanks for giving me the chance to work with you on an exciting research project. You were always there to help and support me on my journey in science. On this road you not only guided me with great care, but also allowed me freedom to develop and follow my own ideas. I enjoyed this time, and I am very proud of what we achieved. Thank you very much for everything!

I am grateful to my promoter, Rob de Boer. Dear Rob, your friendly and calm way to face complicated issues helped me very much. I could always count on your help and support. Thank you very much!

I am grateful to the members of the reading committee for evaluating this thesis: Olaf Doessel, Jan Kucera, Arkady Pertsov, Harold van Rijen and Martyn Nash. I also thank Martyn Nash for valuable discussions and for being a coauthor of my first paper. I thank my friends Daniel Schwerdel and Ivan Kazbanov for being my paranympths.

The Theoretical Biology & Bioinformatics group in Utrecht, is an amazing place to do research. I was impressed from the first moment by this big, multidisciplinary group, where mathematicians, physicists, biologists and computer scientists are working together. It has been a great honour to do my PhD research here. I enjoyed countless scientific views beyond my own nose, excellent courses, and the exciting PhD project I was able to work on. I congratulate and thank Paulien and Ben for building up the group, Rob who is leading the group right now, and all the current and past staff members. I wish you and the whole group all the best for the future! I also want to thank all my dear student colleagues. It has been a pleasure to work with you. I enjoyed the nice discussions in the coffee

room, the lunch breaks and the occasional dinners. I thank Rikkert for many interesting discussions, chess games and sharing an office with me. Dear Rikkert, I thank you also for helping me starting up at the very beginning of my PhD period. I am grateful to Kirsten for many interesting discussions. Dear Kirsten, the discussions on your model for human cardiac cells were very helpful! Thanks Jorg and Folkert for helping me with bureaucratic and latex issues that emerge at the end of a PhD-period! A special thank goes to the system administrator of the group: Dear Jan Kees, thank you very much for a perfect environment to do scientific computations! I want to thank Paulien, Ben and Rob and his family for fantastic group dinners! I enjoyed your cooking skills very much! Thank you for your hospitality! Het was altijd heel gezellig!

I had the chance to visit and follow a course in the group of Sasha at the department for Physics and Astronomy, Gent University. I am very grateful to Sasha and his group in Gent for hospitality and help. Especially I want to thank Ivan: thank you very much that I could be your guest on my trips to Gent! Thanks also for showing me the city and for the interesting discussions, I learned a lot of physics from you!

I am grateful to Chris, Thomas, Anita, Sandro, Christina, Tendai, Daniel, Paul, Sarah, Ivan and Clement for proofreading and linguistic help.

I want to mention here that this PhD research was only possible for me because I could study freely during my undergraduate years in Tübingen and Martinsried; I am grateful to: Wolfgang Neubert, Hans Probst, Ulrich Weser, Hans Bisswanger, Christian Ochsenfeld, Peter Bohley and Wolfram Sarrazin. I want to especially thank Daniel Lambrecht who was my supervisor in my diploma project and taught me very much. I am grateful to Till Brettschneider who showed me the field of Theoretical Biology.

When I arrived in Utrecht I felt a bit alone; however, soon I met nice people that became my friends. Thank you Leslie, Mick, Andreas, Roxana, Djamel, Mitko, Hristina, Yihuan, Mate, Clement, Paul and Ivan! I thank you all very much for a wonderful time! It is great to know you!

Liebe Freunde, Thimo, Ingrid, Anja, Kai, Meike, Daniel, Dany, Basti and Stefan. Es ist immer eine besondere Freude für mich nachhause zu kommen und Euch zu treffen! Vielen Dank!

Liebe Familie, vielen Dank für alles! Euch widme ich dieses Buch!